

# SIMULATING THE PHOTODYNAMICS OF AZOBENZENE DERIVATIVES

USING SURFACE-HOPPING DYNAMICS

DOCTORAL THESIS



SUBMITTED IN FULFILLMENT  
OF THE REQUIREMENTS FOR THE DOCTORAL DEGREE

*Dr. rer. nat.*

TO THE FACULTY OF MATHEMATICS AND NATURAL SCIENCES  
OF THE CHRISTIAN-ALBRECHTS-UNIVERSITY OF KIEL

SUBMITTED BY  
NISS OLE CARSTENSEN

KIEL 2014



Erster Gutachter	Prof. Dr. Bernd Hartke
Zweiter Gutachter	Prof. Dr. Friedrich Temps
Tag der mündlichen Prüfung	03.06.2014
Zum Druck genehmigt	03.06.2014

gez. Prof. Dr. Wolfgang J. Duschl, Dekan





## Kurzzusammenfassung

Die vorliegende Arbeit behandelt die Simulation der Photodynamik unterschiedlicher Azobenzolderivate. Hierzu wurde eine spezifisch für Azobenzol reparametrisierte semiempirische Methode verwendet, in Verbindung mit fewest-switching surface-hopping.

Mit Hilfe der durchgeführten Simulationen konnte ein Reaktionsmechanismus für ein verbrücktes Azobenzolderivat aufgestellt werden. Der Mechanismus ist geprägt von einer ultraschnellen Rotation um den CNNC-Diederwinkel. Während das **1Z**-Isomer einem barrierefreien Reaktionspfad folgt, beinhaltet der Reaktionsmechanismus ausgehend von **1E** eine unvorteilhaft langsame Reorientierung des Molekülgerüsts auf der Grundzustandsfläche. Der vorgeschlagene Reaktionsmechanismus erweist sich als konsistent mit experimentellen Daten der Arbeitsgruppe Temps, die mit Femtosekundenauflösung gewonnen wurden, und wurde in späteren theoretischen Arbeiten in seinen Kernpunkten bestätigt.

Solvenseffekte und verbliebene Diskrepanzen zwischen experimentellen und simulierten Quantenausbeuten konnten erstmals in einer aufwendigen QM/MM-Simulation der Photodynamik mit explizitem *n*-Hexan-Solvens schlüssig erklärt und nahezu vollständig ausgeräumt werden.

In einem themenübergreifenden Projekt wurden mit Hilfe globaler Optimierungsmethoden Substitutionsmuster vorgeschlagen, die die Absorptionswellenlängen eines molekularen Schalters in den Bereich kommerziell erhältlicher Laserpointer verschieben können.

Die dem SFB 677 "Funktion durch Schalten" entstammende Idee, ein künstliches Flimmerhärchen zu entwickeln, das in Verbindung mit einem Plattformkonzept auf Oberflächen fixiert werden kann, wurde simuliert und als vielversprechend eingestuft.

Zusätzlich wurden erste Simulationen zu Azobenzolderivaten in Polymermatrizen, sowie zum Schaltverhalten gegen eine äussere Kraft und dem Design neuer Schalter im Rahmen von fünf Bachelorarbeiten vom Autor betreut.



## Short summary

This work deals with the simulation of the photodynamics of various azobenzene (AB) derivatives. The dynamics were simulated using an azobenzene-specific reparameterized semiempirical ansatz and the fewest-switches surfacing-hopping approach.

A photoisomerization reaction mechanism was proposed for an ethylene-bridged AB derivative. The essential features of the mechanism include: Ultrafast rotation around the N=N bond, a barrierless reaction path starting from the **1Z** isomer and a non-beneficial reorientation of the molecular framework on the ground state surface following excitation of the **1E** isomer. The results were found to be consistent with both preceding experimental time-resolved data of the Temps group and follow-up theoretical publications of various groups.

Both solvent effects and differences between experimental and simulated quantum yields could be explained for the first time by running large-scale QM/MM simulations including explicit *n*-hexane solvent.

By combining global optimization techniques with the semiempirical ansatz, substitution patterns of the bridged AB derivative were optimized, with the aim to shift the absorption wavelengths of the bridged AB derivative. The proposed substitution pattern was intended to shift the wavelengths towards those available in cheap commercial laser pointers.

A complete AB-driven artificial cilium with a molecular platform for surface-mounting as proposed in the SFB 677 "Function by Switching" was simulated and found to be a promising concept.

In addition, first works towards the simulation of azobenzene derivatives embedded in polymer matrices, AB-switching against external forces and molecular design approaches were supervised in five bachelor theses by the author.



# CONTENTS

<b>Contents</b>	<b>I</b>
<b>1 Introduction</b>	<b>1</b>
1.1 Introductory words . . . . .	1
1.2 Azobenzene photochemistry . . . . .	2
<b>2 Methods and techniques</b>	<b>7</b>
2.1 Time-independent methods . . . . .	7
2.2 Dynamics . . . . .	25
2.3 Trajectory analysis . . . . .	34
2.4 Trajectory setup . . . . .	39
<b>3 Bachelor projects</b>	<b>41</b>
3.1 Introduction . . . . .	41
3.2 J. Müller, B.Sc.Thesis . . . . .	43
3.3 R. Scholz, B.Sc.Thesis . . . . .	45
3.4 J. Steffen, B.Sc.Thesis . . . . .	47
3.5 A. Kostevic, B.Sc.Thesis . . . . .	50
3.6 R. Höppner, B.Sc.Thesis . . . . .	54
<b>4 Gas phase photodynamics of a bridged azobenzene derivative</b>	<b>59</b>
4.1 Scope of the project . . . . .	59
4.2 Own Contribution . . . . .	61
4.3 Publication . . . . .	61
4.4 Additional Information . . . . .	62
<b>5 Design of optimally switchable molecules by genetic algorithms</b>	<b>69</b>
5.1 Scope of the project . . . . .	69
5.2 Own Contribution . . . . .	71
5.3 Publication . . . . .	71

5.4	Additional information . . . . .	72
<b>6</b>	<b>Simulating a complete molecular machine in action</b>	<b>79</b>
6.1	Scope of the project . . . . .	79
6.2	Own Contribution . . . . .	80
6.3	Publication . . . . .	80
6.4	Additional information . . . . .	81
<b>7</b>	<b>QM/MM photodynamics of a bridged azobenzene derivative</b>	<b>87</b>
7.1	Scope of the project . . . . .	87
7.2	Own Contribution . . . . .	89
7.3	Publication . . . . .	89
7.4	Additional Information . . . . .	90
<b>8</b>	<b>Summary</b>	<b>97</b>
	<b>Acknowledgements</b>	<b>101</b>
	<b>Bibliography</b>	<b>103</b>
	<b>Declaration</b>	<b>109</b>
	<b>Curriculum Vitae</b>	<b>111</b>







# INTRODUCTION

## 1.1 Introductory words

Azobenzene (AB) is without doubt one of the most intensely studied photochromic compounds. It was first described by the German chemist Eilhard Mitscherlich in 1834.<sup>1</sup> Surprisingly, it took more than another century until the photochromic property, i.e. the *cis*-isomer, of AB was discovered by Hartley.<sup>2</sup> Since then, AB has been the subject of ongoing controversy. While the historical discussion of whether the azo moiety is configured *cis* or *trans* can safely be considered settled, the opposite holds for the mechanism of the photoisomerization. Today, 180 years after the discovery of AB, the photoisomerization mechanism of AB is still discussed, although a consensus on essential features of the reaction mechanism finally begins to emerge.

At Kiel University, AB and its derivatives are studied in the course of the Collaborative Research Center (SFB) 677 "Function by Switching". Due to its ability of reversible photoisomerization, AB was used successfully as a nano-motor in diverse molecular machinery setups, one of which will be discussed in one chapter of this thesis, together with first works on AB (derivatives) subject to inter- or intramolecular stress. However, the central part of the thesis deals with an enhanced AB derivative termed brAB and its photoisomerization mechanism.

This first section is intended to summarize the essential works on the AB photo-switching mechanism. First, the famous interpretation put forward by Rau and

coworkers is reviewed, although this particular mechanism should be considered outdated. The review is given for two reasons: The initial reasoning of Rau and coworkers was based on sterically hindered AB derivatives and is therefore directly connected to the works presented in this thesis. The second reason arises from the fact that this reaction mechanism is still found today in literature on azobenzene and it is the authors personal concern to clearly distinguish between the modern and the deprecated reaction mechanism. The section concludes with a summary of the revised reaction mechanism and of the reaction mechanisms found in sterically hindered AB derivatives.

## 1.2 Azobenzene photochemistry

AB photoisomerization can be induced by irradiating either isomer with visible light using wavelengths of either 380-500 or 280-380 nm. The first interval corresponds to an  $n \rightarrow \pi^*$  ( $S_0 \rightarrow S_1$ ) excitation, while the latter is a  $\pi \rightarrow \pi^*$  ( $S_0 \rightarrow S_{2,3}$ ) transition.<sup>3</sup> The efficiency of the isomerization is commonly given in terms of quantum yields,  $\Phi = (\text{number of isomerized molecules}) / (\text{number of absorbed photons})$ . These quantum yields are usually expected to be independent of the excitation wavelength, based on an empirical principle formulated in 1950 by M. Kasha.<sup>4</sup> However, in the case of AB, the quantum yields resulting from a  $\pi \rightarrow \pi^*$ -excitation are significantly lowered for both isomers.

The mechanism of the AB photoisomerization could in principle proceed via two reaction pathways: Inversion or rotation as depicted in Fig. 1.1. Not surprisingly, the question of the two possible reaction mechanisms and the violation of Kasha's rule following a photoexcitation ( $n \rightarrow \pi^*$  or  $\pi \rightarrow \pi^*$ ) of naked AB has been addressed in large amount of both theoretical and experimental studies.

### The (historical) inversion mechanism

The first notable theoretical work on AB dates back into the beginning of the 1980s and was published by Monti and coworkers.<sup>5</sup> The calculation employed the first three singlet states at a CI-level of theory using a minimal STO-3G basis set. With this setup a scan along the reaction coordinates CNNC and NNC was calculated, while the remaining internal coordinates were held fixed. According to Monti an  $n \rightarrow \pi^*$  excitation of AB results in an inversion, while a  $\pi \rightarrow \pi^*$  excitation leads to a rotational mechanism. The theoretical findings clearly supported experimental results published

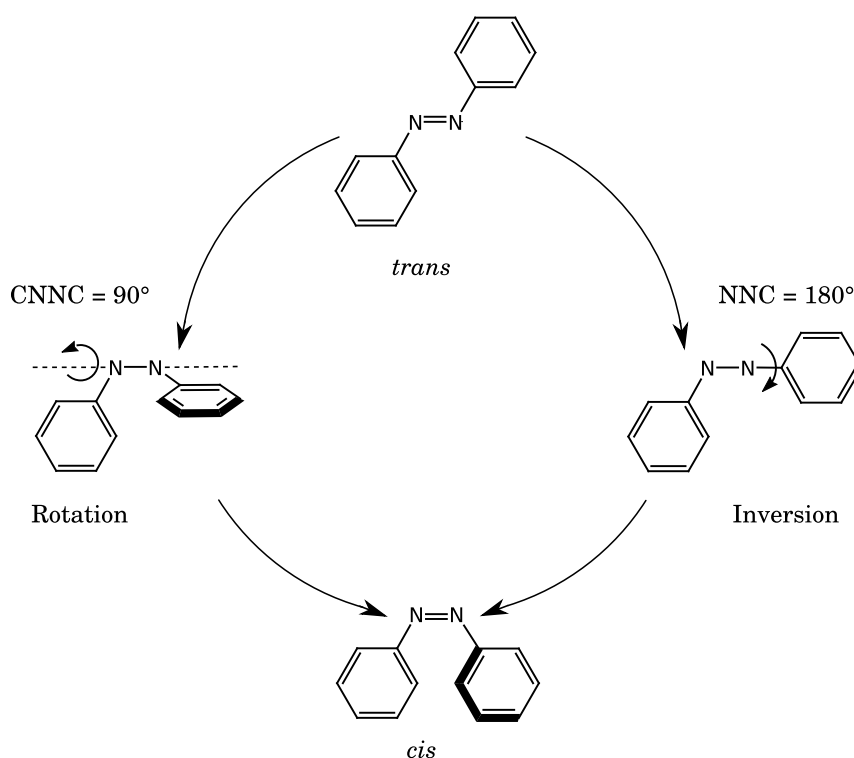


Figure 1.1: Depiction of the inversional (*right*) and rotational (*left*) pathway in AB photodynamics.

shortly before in 1982 by Rau and coworkers.<sup>6</sup>

Due to the computational limits of those days, the energetics from the calculations alone could not be trusted, but the agreement with the experimental findings seemed to have put an end to the discussion about the reaction mechanism. In the experiment Rau and coworkers measured the kinetics of the sterically hindered azobenzophanes depicted in Fig. 1.2. Since the hula-twist mechanism observed in some stilbenes

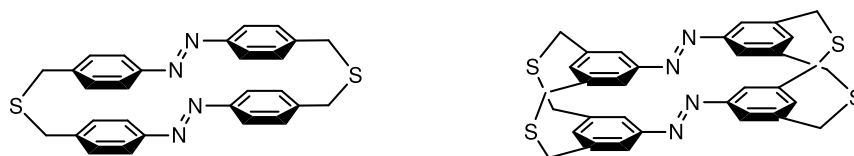


Figure 1.2: Azobenzophanes studied by Rau and coworkers.<sup>6</sup>

and sterically hindered ABs was not yet discovered<sup>(1)</sup>, Rau and coworkers expected the rotational pathway to be completely blocked. Both azobenzophanes in Fig. 1.2 were found to exhibit a reversible photoisomerization leading to the conclusion: "The reversible photoisomerization of 1 and 2 finally provides unequivocal proof

<sup>(1)</sup>The hula-twist mechanism was proposed about three years later by Liu and Asato (see below).

that trans-cis isomerization of azo compounds can proceed via inversion."<sup>6</sup> The fact that the quantum yields of both azobenzophanes were equal for  $n \rightarrow \pi^*$  and  $\pi \rightarrow \pi^*$  excitations, in contrast to naked AB, was finally interpreted as proof for a rotational mechanism upon  $\pi \rightarrow \pi^*$  excitation.

It is worth noticing that despite the new insights into AB photochemistry put forward by theoreticians and experimentalists alike in the mid 1990s(see below), this (historical) interpretation is still found in today's literature. For example a recently published review(!) article by Pathem, Claridge, Zheng and Weiss<sup>7</sup> states that "Two possible switching mechanisms exist. One is an inversion mechanism: a forbidden  $n \rightarrow \pi^*$  excitation ( $S_0$  to  $S_1$ ), with in-plane bending of N=N-C angle from  $\sim 120^\circ$  to  $\sim 240^\circ$ . The other is a rotation mechanism: an allowed  $\pi \rightarrow \pi^*$  excitation ( $S_0$  to  $S_2$ ), resulting in out-of-plane rotation of the N=N bond."<sup>7</sup> Given the fact that the rotational reaction mechanism (see below) is supported not only by several ultrafast time-resolved experimental results, but also by high-level multireference calculations, the inversion based reaction mechanism for naked AB should be considered outdated.<sup>(2)</sup> This is especially important because, in the laboratory, direct practical relevance for the designer of AB based molecular machinery arises from extended spatial requirements resulting from a rotational based mechanism (see also Chap. 6).

### The (modern) rotation mechanism

The new reaction mechanism was facilitated by Persico<sup>8</sup> and Shoda,<sup>9</sup> who ran more sophisticated CASSCF and multireference calculations (CIPSI) and found drastic differences in the shape of the potential energy surfaces compared to the early studies of Monti *et al.*. The central difference is that the inversion pathway exhibits a barrier, while the rotational pathway is essentially barrierless for  $n \rightarrow \pi^*$  and  $\pi \rightarrow \pi^*$  excitations alike. This finding immediately lead to the question how Kasha's rule can be violated if both reaction mechanisms follow the rotational pathway? The surprising answer was given in 2004-2005 in a series of independent publications by Persico, Orlandi and Diau.<sup>3,10,11</sup>

In order to explain the lowered quantum yields following  $\pi \rightarrow \pi^*$  excitation, the CNN-angles have to be taken into account. During the excited-states dynamics the CNN angles open up symmetrically<sup>(3)</sup> from  $\approx 120^\circ$  to  $\approx 140^\circ$  and oscillate. In the

<sup>(2)</sup>At least if it is based on the early work by Monti and Rau as in the case of Weiss and coworkers.

<sup>(3)</sup>The symmetric opening contrasts with the unsymmetric opening required for an inversion mechanism.

studies of Persico, Orlandi and Diau it could be shown that the  $S_2$ -surface and the  $S_1$ -surface are connected by a conical intersection seam that becomes accessible by the CNN-opening. In fact the  $S_2$  surface is left almost immediately after the start of the dynamics via this de-excitation channel to proceed on the  $S_1$  surface. In the words of Diau, an excitation to the  $S_2$  state leads to a rapid formation of "a vibrationally hot  $S_1$  species"<sup>11</sup> that enters the  $S_0/S_1$  seam before reaching the midpoint along the rotational pathway (CNNC=90°) thus lowering the quantum yield. The schematic of the reaction mechanism is shown in Fig. 1.3.

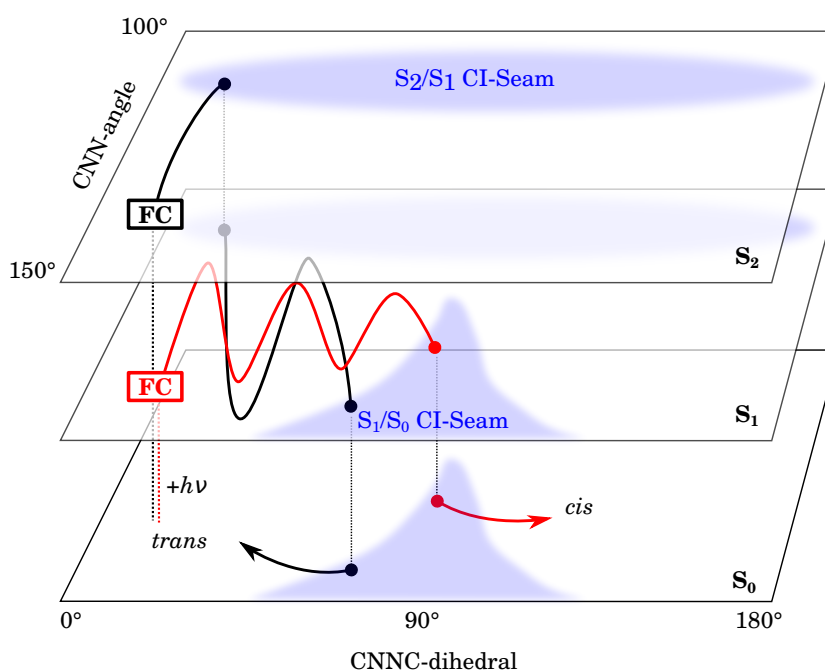


Figure 1.3: Cartoonlike picture of the AB photoisomerization mechanism following  $S_0 \rightarrow S_1$  ( $n \rightarrow \pi^*$ , red trajectory) and  $S_0 \rightarrow S_2$  ( $\pi \rightarrow \pi^*$ , black trajectory) excitations explaining the lowered quantum yields following  $\pi \rightarrow \pi^*$  excitation. The trajectories start at the according Franck-Condon points (FC). Surface-hops are indicated by solid circles connected with dotted lines (see text for details).

Obviously, the essential statements of the new reaction mechanism are: The rotational pathway is feasible in both cases and lowered quantum yields following  $\pi \rightarrow \pi^*$  excitation do not result from a significant different reaction pathways. Instead, the lowered quantum yields result from an ultrafast and efficient internal conversion from the  $S_2$  to the  $S_1$ -state that in turn causes an untimely internal conversion to the ground state on the educt side of the ground-state reaction barrier.

At first sight, the above reaction mechanism is contradicting the experimental re-

sults on sterically hindered AB derivatives, in particular the early experimental results reported on azobenzophanes by Rau. The question was again addressed by Persico and coworkers in 2005, who presented a surface-hopping dynamics study on the photoisomerization mechanism of azobenzophanes.<sup>12</sup> Surprisingly, their analysis of the trajectories revealed that the rotational pathway was not blocked at all. Instead, the azo-moiety could rotate rather freely without forcing large scale displacements to the phenyl rings. This reaction mechanism is commonly termed the "hula-twist" movement. It was originally proposed by Liu and Asato<sup>(4)</sup> in order to explain the *cis*→*trans*-isomerization of the retinal chromophore in its restricting opsin matrix.<sup>13</sup> Since then, the hula-twist mechanism was discussed for stilbene<sup>14</sup> and photoswitchable organic glasses.<sup>15-17</sup> Note that the bridged AB derivative simulated in this work also exhibits a hula-twist based mechanism (see Chap. 4, p. 59).

The quantum yields in the azobenzophanes shown above in Fig. 1.2 can now be explained by the sterical constraints upon the CNN-angles. In simple words: The restriction of the CNN-angles prevents the azobenzophanes from experiencing the untimely return to the ground-state surface explained above and the quantum yields of  $n \rightarrow \pi^*$  and  $\pi \rightarrow \pi^*$  were found equal as in the experiment of Rau and coworkers.

---

<sup>(4)</sup>Both from the University of Hawaii, Honolulu, hence the nomenclature.

## METHODS AND TECHNIQUES

This section is intended to illustrate the methods and techniques used to simulate AB photodynamics throughout this thesis. It is split in two parts: One dealing with techniques used for time-independent calculations, i.e. classical molecular mechanics (MM), quantum chemical methods (QM) and the combination of both in quantum mechanics/molecular mechanics (QM/MM) approaches. The other part deals with methods used to simulate the (photo)dynamics of a system, which are classical molecular dynamics (MD) and semiclassical surface-hopping dynamics. In order to keep this section focused, a simplified description was chosen. As a consequence, the reader will encounter gaps wherever a detailed discussion would exceed the scope of this section. In this case, a more detailed depiction is found in the quoted literature.

### 2.1 Time-independent methods

#### Molecular mechanics

Molecular mechanics are based on the idea that atoms in a molecule can be treated as (charged) mass particles that obey the classical equations of motion. The commonly used standard force fields for molecular mechanics, including the one used in this thesis, employ simple parametrized analytical expressions, for all interatomic interactions. These can be grouped into bonded and non-bonded interactions.<sup>(1)</sup>

---

<sup>(1)</sup>Often, the interactions are divided into intramolecular and intermolecular interactions,<sup>18</sup> which might be misleading, since Coulomb and van der Waals terms are usually also calculated for intramolecular interactions.

The bonded interactions consist of bond-stretching ( $E_{\text{str.}}$ ), angle-bending ( $E_{\text{bend}}$ ) and torsional ( $E_{\text{tors.}}$ ) terms, while the non-bonded interactions include Coulomb ( $E_{\text{el.}}$ ) and van-der-Waals ( $E_{\text{vdW}}$ ) interactions. Some force fields additionally include coupling terms between the bonded interactions.

As an example, the bonded interactions ( $E_{\text{b.}}$ ) of the all-atom optimized potentials for liquid simulations force field (OPLSAA)<sup>19</sup> are given by

$$\begin{aligned}
 E_{\text{b.}} = & \sum_{\text{bonds}} K_r (r - r_e)^2 \\
 & + \sum_{\text{angles}} K_\theta (\theta - \theta_e)^2 \\
 & + \sum_{\text{dihedrals}} \left[ \frac{V_1}{2} [1 + \cos(\phi + f_1)] \right. \\
 & \quad + \frac{V_2}{2} [1 - \cos(2\phi + f_2)] \\
 & \quad \left. + \frac{V_3}{2} [1 + \cos(3\phi + f_3)] \right]
 \end{aligned} \tag{2.1}$$

where  $r$ ,  $\theta$  and  $\phi$  denote a bond length, an angle and a dihedral angle respectively. Within Eq. 2.1, the bond-stretching and angle-bending terms are simple harmonic potentials, parametrized with force constants ( $K_r$ ,  $K_\theta$ ) and equilibrium values ( $r_e$ ,  $\theta_e$ ). The functional form of the torsional energy is constructed by a Fourier series and depends on the parameters  $V_1$ ,  $V_2$  and  $V_3$  (the coefficients of the series) and  $f_1$ ,  $f_2$  and  $f_3$  (the according phase angles). Non-bonded Coulomb and van-der-Waals terms ( $E_{\text{n.b.}}$ ) for two fragments  $a$  and  $b$  are given by

$$E_{\text{n.b.}} = \sum_{i \text{ on } a} \sum_{j \text{ on } b} \left[ \frac{q_i q_j e^2}{r_{ij}} + 4\epsilon_{ij} \left( \left( \frac{\sigma_{ij}}{r_{ij}} \right)^{12} - \left( \frac{\sigma_{ij}}{r_{ij}} \right)^6 \right) \right] f_{ij} \tag{2.2}$$

with the distance ( $r_{ij}$ ), the partial charges of the atoms ( $q_i$ ,  $q_j$ ), and the Lennard-Jones parameters ( $\epsilon_{ij}$ ,  $\sigma_{ij}$ ). As already mentioned, the intramolecular non-bonded-interactions are also calculated but only for atom-pairs spaced at least 3 bonds apart. The scaling parameter  $f_{ij}$  is set to be 1.0 in all cases except for intramolecular 1,4-interactions and results from applying the same atom parameters to inter- and intramolecular interactions. The total energy given by the OPLSAA force field is then given by the sum of Eq. 2.1 and Eq. 2.2.

In the context of this work an improved version of the force field termed OPLSAA-L<sup>20</sup>



was used for the MM part in the QM/MM calculations and the molecular dynamics of the solvent boxes. It does not differ in its functional form from the above OPLSAA force field published in 1996. Instead, the torsional parameters of the force field were reparametrized in 2001 employing pseudospectral local MP2<sup>21</sup> (LMP2/cc-pVTZ(-f)//HF/6-31G\*) *ab-initio* calculations<sup>(2)</sup> and an improved fitting strategy. As a result the root mean square (RMS) deviation between force field and *ab-initio* calculations was reduced by 40%.

## Quantum Mechanics

This section introduces the time-independent quantum mechanical methods used in this thesis. First, the Hartree-Fock method is reviewed briefly, followed by an introduction to the theoretical background of the quantum chemical methods used in this thesis, namely FOCI-AM1, (RI-)MP2 and DFT-D.

### Hartree-Fock

The time-independent Schrödinger equation in atomic units for a system containing  $N$  electrons and  $M$  nuclei is given by

$$\begin{aligned} \hat{H}\psi &= E\psi \\ \text{with} \\ \hat{H} &= - \sum_{A=1}^M \frac{1}{2M_A} \nabla_A^2 \\ &\quad - \sum_{i=1}^N \frac{1}{2} \nabla_i^2 \\ &\quad + \sum_{i=1}^N \sum_{j \neq i}^N \frac{1}{r_{ij}} \\ &\quad - \sum_{i=1}^N \sum_{A=1}^M \frac{Z_A}{r_{iA}} \\ &\quad + \sum_{A=1}^M \sum_{B>A}^M \frac{Z_A Z_B}{R_{AB}} \end{aligned} \tag{2.3}$$

where  $\psi$  marks the wavefunction,  $\hat{H}$  the molecular Hamilton operator,  $r/R$  the distance between two particles,  $Z$  the nuclear charge and  $M_A$  the mass of nucleus  $A$ . The Schrödinger equation cannot be solved analytically, except for very simple model systems. However, it is nowadays routinely solved numerically. A vast variety of methods, differing in computational cost and accuracy exist and can be used, but

<sup>(2)</sup>According to the authors OPLSAA-L stands for OPLSAA-LMP2.

most of them share a common ancestor called the Hartree-Fock method.

The Hartree-Fock method originated shortly after discovery of the Schrödinger equation (first published 1926<sup>22</sup>) itself as D.R. Hartree introduced the first self-consistent field method in 1928.<sup>23</sup> It was reformulated shortly after by J.C. Slater<sup>24</sup> and V.A. Fock independently who both pointed out that the principle of antisymmetry was violated in the original formulation. In 1935 Hartree published a reformulation of his self-consistent field method with his father, taking into account the results from Slater and Fock, resulting in the formulation of the Hartree-Fock equations essentially as known today.<sup>25</sup>

In order to derive the Hartree-Fock method, the ansatz for the unknown wavefunction  $\psi$  is taken to be a Slater determinant

$$\psi_{SD} = \frac{1}{\sqrt{N!}} \begin{vmatrix} \chi_i(x_1) & \chi_j(x_1) & \dots & \chi_k(x_1) \\ \chi_i(x_2) & \chi_j(x_2) & \dots & \chi_k(x_2) \\ \vdots & \vdots & \ddots & \vdots \\ \chi_i(x_N) & \chi_j(x_N) & \dots & \chi_k(x_N) \end{vmatrix} \quad (2.4)$$

where  $N$  denotes the number of electrons,  $\chi$  single-electron wavefunctions (orbitals) and  $x_i$  the coordinate of electron  $i$ . The orbitals are the wavefunctions obtained from a Schrödinger equation describing a single electron in the potential of all nuclei. The Hamiltonian for this single electron Schrödinger equation is given by

$$\hat{h}(i) = -\frac{1}{2}\nabla_i^2 - \sum_{A=1}^M \frac{Z_A}{r_{iA}} \quad (2.5)$$

By using  $\psi_{SD}$  the antisymmetry principle is satisfied: The arrangement of every electron in every orbital within a determinant not only considers all permutations needed but the exchange of an odd number of electrons also results in the required sign change of the wavefunction.

Since the electrons are described completely uncorrelated if the orbitals are calculated independent via Eq. 2.5, a physically sensible result is only obtained by optimizing all orbitals at the same time. The simultaneous optimization of all orbitals is achieved by minimizing the energy  $E$  obtained from

$$E = \langle \psi_{SD} | \hat{H} | \psi_{SD} \rangle \quad (2.6)$$

where  $\hat{H}$  denotes the molecular Hamiltonian shown in Eq. 2.3. Commonly the minimization is carried out using Lagrange multipliers.<sup>(3)</sup> Within the molecular Hamiltonian, the electrons interact via a Coulomb term  $\frac{1}{r_{ij}}$ . As a consequence one electron experiences the potential generated by the other electrons as a mean field. The result of the variational calculus is then given by

$$\begin{aligned}\hat{f}|\chi_m\rangle &= \epsilon_m |\chi_m\rangle \\ \hat{f}(1) &= \hat{h}(1) + \sum_n [2\hat{j}_n(1) - \hat{k}_n(1)] \\ \hat{j}_n(1)|\chi_m(1)\rangle &= \langle\chi_n(r_2)|\frac{1}{r_{12}}|\chi_n(r_2)\rangle|\chi_m(r_1)\rangle \\ \hat{k}_n(1)|\chi_m(1)\rangle &= \langle\chi_n(r_2)|\frac{1}{r_{12}}|\chi_m(r_2)\rangle|\chi_n(r_1)\rangle\end{aligned}\tag{2.7}$$

where  $\hat{f}$  denotes the Fock operator,  $\hat{j}$  the Coulomb operator and  $\hat{k}$  the exchange operator. In contrast to orbitals obtained from the single-particle Hamiltonian shown in Eq. 2.5, a HF-orbital depends on all other HF-orbitals via the Coulomb and exchange terms in the Fock operator.

In practice, each of the unknown orbitals is presented as a linear combination of  $M$  (known) atomic orbitals  $\phi$  (linear combination of atomic orbitals, LCAO)

$$\chi_m = \sum_i^M c_{im}\phi_i\tag{2.8}$$

by inserting the above into the Hartree-Fock equations (Eq. 2.7), the Roothaan-Hall equations are obtained

$$\begin{aligned}FC &= SC\epsilon \\ F_{\alpha\beta} &= \langle\phi_\alpha|\hat{f}|\phi_\beta\rangle \\ S_{\alpha\beta} &= \langle\phi_\alpha|\phi_\beta\rangle\end{aligned}\tag{2.9}$$

where  $F$  denotes the Fock-Matrix,  $S$  the overlap matrix,  $C$  the matrix containing the MO expansion coefficients and  $\epsilon$  the diagonal matrix of the MO energies. Starting from an initial guess the coefficients are iteratively optimized until a suitable convergence criterion is fulfilled. The optimized set of orbitals finally determines the so called self-consistent field (SCF) solution.

### FOCI-AM1

The floating-occupation-configuration-interaction Austin-Model 1<sup>27,28</sup> method (FOCI-AM1) was used for all surface-hopping calculations, except for the dynamics results

<sup>(3)</sup>The optimization is constrained, because the molecular orbitals should remain orthogonal and normalized upon variation of the orbitals.<sup>26</sup>

presented in Chap. 5, where a different semiempirical method termed Parametric Model 3 (PM3)<sup>26</sup> was used. Apart from employing a PM3 wavefunction the setup was the same as the one used with AM1.

In order to reduce the computational cost of the Hartree-Fock method<sup>(4)</sup>, the so called semiempirical methods were developed. The following approximations are made within (most) semiempirical models:

1. Only valence electrons are considered. Core electrons are accounted for by reducing the charge of the nuclei accordingly and/or via parametrized analytic expressions.
2. Only a minimum basis set is used for the valence electrons. Usually, only s- and p-orbitals are used, and they are taken to be Slater-type functions (STO's).
3. Products of basis functions located on different atoms are neglected if they depend on the same electron coordinates (Zero Differential Overlap, ZDO, see below).

Among the approximations listed above the ZDO-approximation is the central one. By introducing the ZDO-approximation all three and four center two-electron orbitals of the Fock-Matrix become zero, as well as all one-electron integrals involving three centers. Finally, the overlap matrix turns into a unity matrix. Denoting atomic orbitals as  $\mu$  and  $\nu$ <sup>(5)</sup> and indexing the center, e.g.  $\mu_A$  for atomic orbital  $\mu$  centered on core  $A$ , the approximations write out as

$$\begin{aligned} S_{\mu\nu} &= \langle \mu | \nu \rangle = \delta_{\mu\nu} \delta_{AB} \\ \langle \mu_A \nu_B | \lambda_C \sigma_D \rangle &= \delta_{AC} \delta_{BD} \langle \mu_A \nu_B | \lambda_C \sigma_D \rangle \end{aligned} \quad (2.10)$$

Taken together with the approximations listed above these are referred to as the neglect of diatomic differential overlap approximations (NDDO).

The methods Austin Model 1 (AM1) and Parametric Model 3 (PM3) are modified parametrizations of the NDDO model. The label 'modified' refers to the explicit calculation of the overlap matrix  $S$ , as opposed to the initial ZDO-approximations. Within AM1 parametrizations are carried out for the one-center one-electron integrals as follows

$$h_{\mu\nu} = \langle \mu_A | \hat{h} | \nu_A \rangle = \delta_{\mu\nu} U_\mu - \sum_{a \neq A}^{N_{\text{nuclei}}} Z'_a \langle \mu_A \mu_A | \nu_A \nu_A \rangle \quad (2.11)$$

<sup>(4)</sup>Hartree-Fock scales formally as  $N^4$ , with  $N$  being the number of basis functions.<sup>26</sup>

<sup>(5)</sup>Due to historical reasons, semiempirical atomic orbitals are commonly labeled  $\mu, \nu, \lambda$  and  $\sigma$ .

where the matrix element  $h_{\mu\nu}$  is represented by the parameter  $U_\mu$  corresponding to the energy of a single electron in the field of the nucleus. Corrections from the reduced charges of all other nuclei are added via the parameters  $Z'_a$  and parametrized one-center two-electron integrals. The integrals are parametrized according to

$$\langle \mu_A | \hat{h} | \nu_B \rangle = \frac{1}{2} S_{\mu\nu} (\beta_\mu + \beta_\nu) \quad (2.12)$$

where  $\beta_\mu$  and  $\beta_\nu$  are the so called resonance parameters. Since only s- and p-type basis functions are used, there are only five types of two-electron one-center integrals that need to be known. All of these are not calculated explicitly, but turned into the following set of parameters

$$\begin{aligned} \langle ss | ss \rangle &= G_{ss} \\ \langle sp | sp \rangle &= G_{sp} \\ \langle ss | pp \rangle &= H_{sp} \\ \langle pp | pp \rangle &= G_{pp} \\ \langle pp' | pp' \rangle &= G_{p2} \end{aligned} \quad (2.13)$$

By a comparison with Eq. 2.7 the  $G$  parameters can be identified as Coulomb terms, while the  $H$  parameters result from the exchange integral. The last parameter in Eq. 2.13 involves two different p-type orbitals, e.g.  $p_x$  and  $p_y$ . The final parameters result from the core-core interactions

$$\begin{aligned} V_{mn}(A, B) &= Z'_A Z'_B \langle s_A s_A | s_B s_B \rangle (1 + \exp(-\alpha_A R_{AB}) + \exp(-\alpha_B R_{AB})) \\ &+ \frac{Z'_A Z'_B}{R_{AB}} \sum_k (a_{kA} \exp(-b_{kA} (R_{AB} - c_{kA})^2) a_{kB} \exp(-b_{kB} (R_{AB} - c_{kB})^2)) \end{aligned} \quad (2.14)$$

where  $R_{AB}$  denotes the distance of the nuclei and  $\alpha, a, b, c$  are fitting parameters. Depending on the atom the sum index  $k$  takes on values between 2 and 4.<sup>(6)</sup> The parametrization of the AM1 method was carried out against both atomic spectra (Coulomb and exchange parameters) and molecular data (core-core parameters).

The floating-occupation approach (FLOCC)<sup>29</sup> used with the AM1 semiempirics is based on the idea that orbitals used in the SCF-procedure are allowed to possess fractional occupations which may differ from 0, 1 or 2. The fractional occupation is introduced with the help of the density matrix  $D^{(7)}$  containing the coefficients used in

<sup>(6)</sup>In fact the functional form of the core-core repulsion is in part alike to the model used in an ancestor of AM1 called modified neglect of differential overlap (MNDO). The second term involving the sum of Gaussian functions can be considered a patch of the MNDO-term, explaining the varying amount of added Gaussian functions.

<sup>(7)</sup>Not to be confused with the density matrix  $\rho$  introduced in the dynamics chapter below.

the LCAO representation of the molecular orbitals

$$\begin{aligned} D_{ij} &= \sum_k C_{ik} C_{jk} \\ D_{ij}^{\text{FLOCC}} &= \sum_k N_k C_{ik} C_{jk} \end{aligned} \quad (2.15)$$

here  $C_{ik}$  marks the  $k$ th molecular orbital coefficient of the  $i$ th basis function and  $N_k$  are the fractional occupation numbers introduced by the FLOCC approach. Since the total number of electrons has to stay constant the occupation numbers are self-consistently determined from the orbital energies  $\epsilon$

$$N_k = \frac{\sqrt{2}}{\sqrt{\pi}w} \int_{-\infty}^{\epsilon_F} \exp\left[-\frac{(\epsilon - \epsilon_k)^2}{2w^2}\right] d\epsilon \quad (2.16)$$

where  $\epsilon_F$  is the Fermi level and  $w$  is an arbitrary parameter defining the spread of electron populations. The Fermi level  $\epsilon_F$  is determined from the requirement that the total sum of occupation numbers must result in the total number of electrons  $N$

$$N = \sum_k N_k \quad (2.17)$$

With the usage of the modified density matrix  $D^{\text{FLOCC}}$  in the SCF cycle the flexibility of the wavefunction is significantly improved and problems like homolytic bond breaking and orbital degeneracy are treated correctly.<sup>30</sup> According to Persico and coworkers,<sup>31</sup> FLOCC also facilitates the description of excited states. The reason for this lies in the partial filling of orbitals above the Fermi level. As a consequence these orbitals take part in the optimization cycle to some extent. Finally, the floating occupation numbers are determined self-consistently and can therefore adjust to changing molecular geometries.

In the FOCI-AM1 approach, FLOCC is combined with a configuration interaction (CI) approach and only a subset of selected orbitals are allowed to possess a floating occupation. The CI-approach employs a linear combination of Slater determinants in contrast to the Hartree-Fock method, where a single Slater determinant is used. Additional determinants are constructed from a Hartree-Fock Slater determinant by exchanging occupied with non-occupied (virtual) orbitals. The molecular orbitals are held fixed during the complete calculation. If  $\Phi_{\text{HF}}$  denotes the Hartree-Fock Slater determinant and excited determinants are labeled by indices (single excitation (S), double excitation (D),...) the CI-ansatz is given by

$$\Psi_{CI} = a_0 \Phi_{\text{HF}} + \sum_S a_S \Phi_S + \sum_D a_D \Phi_D + \sum_T a_T \Phi_T + \dots = \sum_{i=0} a_i \Phi_i \quad (2.18)$$

The linear combination of all possible determinants that can be constructed from a single Slater determinant is known as Full-CI (FCI). If the atomic basis is complete an infinite number of excited Slater determinants can be formed and FCI is in principle the exact solution to the Schrödinger equation. In practical applications the basis is finite and FCI is only exact within the subspace spanned by this basis. Apart from very small systems FCI is computationally not feasible. Therefore, the series is usually truncated at some point. The truncation can be done following various strategies: A FCI within a subset of selected active orbitals with an additional optimization of MO coefficients leads to the complete active space-SCF procedure (CASSCF). A further distinction of the active space into complete active spaces (all possible excitations) and restricted active spaces (e.g. only single or double excitations) leads to the restricted active space-SCF (RASSCF) method.

The FOCI-AM1 ansatz can be considered RASSCF-like. The excited determinants are formed from the Slater determinant obtained from a (reparametrized!) AM1 calculation as follows:

- The active space consists of 7 occupied and 6 virtual orbitals summing up to 14 electrons in 13 orbitals.
- For three occupied and one virtual orbital (two lone pairs, a  $\pi$  and a  $\pi^*$  orbital) the active space included all determinants that can be formed if they result in 0 total spin.
- All single excitations for the 7 occupied and 6 virtual orbitals are included.

This azobenzene specific selection results in a total of 94 determinants and was used 'as is' throughout the thesis, because it corresponds to the setup used in the reparametrization of the method.

## RI-MP2

The resolution of the identity - Møller-Plesset perturbation theory (second order approximation) method (RI-MP2) was used for benchmarking the ground-state brAB-*n*-hexane interactions. The two elements of the method, RI and MP2 will be briefly explained in the following.

Following general perturbation theory,<sup>26,32</sup> the molecular Hamiltonian  $\hat{H}$  is replaced by the sum of an unperturbed Hamiltonian yielding the 'exact' solution to the

unperturbed system  $\hat{H}^{(0)}$  and a perturbation operator  $\hat{H}^{(1)}$

$$\begin{aligned}\hat{H} &= \hat{H}^{(0)} - \lambda \hat{H}^{(1)} \\ \hat{H}^{(0)} &= \sum_i \hat{f}(i) = \sum_i \left( \hat{h}(i) + \sum_j (\hat{j}_j - \hat{k}_j) \right) \\ &= \sum_i \hat{h}(i) + \sum_i \sum_j (\hat{g}_{ij}) \\ \hat{H}^{(1)} &= \hat{H} - \hat{H}^{(0)} = \frac{1}{2} \sum_{i \neq j} \frac{1}{r_{ij}} - \sum_i \hat{g}(i)\end{aligned}\tag{2.19}$$

where  $\hat{f}$  denotes the Fock operator (see Eq. 2.7),  $\hat{h}$  the single-particle Hamiltonian and  $\hat{j}$  and  $\hat{k}$  the Coulomb and Exchange operators. The perturbation is given by the difference of the exact molecular Hamiltonian and the approximate Hamiltonian formed by a sum of Fock operators, or in other words: The perturbation is given by the difference between the exact electron correlation given by the  $1/r_{ij}$  term and the approximate mean field - electron interaction provided by the Fock operator.<sup>(8)</sup>

Following the formalism of general many-body perturbation theory the still unknown wavefunction and energy can be expanded in a Taylor series

$$\begin{aligned}\Psi &= \Psi^{(0)} + \lambda^{(0)} \Psi^{(0)} + \lambda^{(1)} \Psi^{(1)} + \lambda^{(3)} \Psi^{(3)} + \dots \\ E &= E^{(0)} + \lambda^{(0)} E^{(0)} + \lambda^{(1)} E^{(1)} + \lambda^{(3)} E^{(3)} + \dots\end{aligned}\tag{2.20}$$

Inserting Eq. 2.20 and 2.19 into the Schrödinger equation and collecting terms with the same power of  $\lambda$  results in a set of perturbation equations

$$\begin{aligned}\lambda^{(0)} : \hat{H}^{(0)} \Psi^{(0)} &= E^{(0)} \Psi^{(0)} \\ \lambda^{(1)} : \hat{H}^{(0)} \Psi^{(1)} + \hat{H}^{(1)} \Psi^{(0)} &= E^{(0)} \Psi^{(1)} + E^{(1)} \Psi^{(0)} \\ \lambda^{(2)} : \hat{H}^{(0)} \Psi^{(2)} + \hat{H}^{(1)} \Psi^{(1)} &= E^{(0)} \Psi^{(2)} + E^{(1)} \Psi^{(1)} + E^{(2)} \Psi^{(0)} \\ &\vdots \\ \lambda^{(n)} : \hat{H}^{(0)} \Psi^{(n)} + \hat{H}^{(1)} \Psi^{(n-1)} &= \sum_{i=0}^n E^{(i)} \Psi^{(n-i)}\end{aligned}\tag{2.21}$$

after a multiplication from the left with  $\langle \Psi^{(0)} |$  the energy corrections are given by

$$\begin{aligned}E^{(0)} &= \langle \Psi^{(0)} | \hat{H}^{(0)} | \Psi^{(0)} \rangle \\ E^{(1)} &= \langle \Psi^{(0)} | \hat{H}^{(1)} | \Psi^{(0)} \rangle \\ E^{(2)} &= \langle \Psi^{(0)} | \hat{H}^{(1)} | \Psi^{(1)} \rangle \\ &\vdots \\ E^{(n)} &= \langle \Psi^{(0)} | \hat{H}^{(1)} | \Psi^{(n-1)} \rangle\end{aligned}\tag{2.22}$$

<sup>(8)</sup>The factor 1/2 results from the double sum before Coulomb and Exchange operators, caused by the summing of Fock operators.



the  $n$ th energy correction therefore depends only on the  $n-1$ th correction of the wavefunction. Eq. 2.22 can be reformulated to obtain an even better description for the  $2n+1$ th energy correction

$$E^{(2n+1)} = \langle \Psi^{(n)} | \hat{H}^{(1)} | \Psi^{(n)} \rangle - \sum_{k,l=1}^n E^{(2n+1-k-l)} \langle \Psi^{(k)} | \Psi^{(l)} \rangle \quad (2.23)$$

where the  $E^{(2n+1)}$  is only depending on the the  $n$ th order correction for the wavefunction. Given the choice of the ansatz presented in Eq. 2.20, the unperturbed wavefunctions are known exactly and given by the Hartree-Fock determinant and all excited determinants (labeled  $\Phi_I$ ). Since the Hamilton operator is hermitian, the solution forms a complete basis and the perturbed wavefunction can in theory be exactly represented in the infinite basis of determinants. Nonetheless, in real life applications, the basis remains finite and incomplete, therefore this expansion will introduce an error.

The first- and second-order corrected wavefunctions are given by

$$\begin{aligned} \Psi^{(1)} &= \sum_I c_I^{(1)} \Phi_I \\ \Psi^{(2)} &= \sum_I c_I^{(2)} \Phi_I \end{aligned} \quad (2.24)$$

the expansion coefficient  $c_I^{(1)}$  can now be obtained from the first order term in Eq. 2.22 by multiplication from the left with  $\langle \Phi_I |$

$$c_I^{(1)} = - \frac{\langle \Phi_I | \hat{H} | \Phi_0 \rangle}{\langle \Phi_I | \hat{H}^{(0)} - E^{(0)} | \Phi_I \rangle} \quad (2.25)$$

where  $\Phi_0$  denotes the Hartree-Fock determinant. The coefficients are finally obtained recognizing that only doubly excited determinants give non-vanishing matrix elements with  $\Phi_0$ . Eq. 2.25 then becomes

$$c_{ab}^{ij(1)} = - \frac{\langle \Phi_{ij}^{ab} | \hat{H} | \Phi_0 \rangle}{\epsilon_a + \epsilon_b - \epsilon_i - \epsilon_j} \quad (2.26)$$

where  $\Phi_{ij}^{ab}$  denotes the doubly excited determinants and  $\epsilon$  the Hartree-Fock eigenvalues, corresponding to Koopmans' theorem. The final second order energy correction in an MP2 calculation can thus be written out as

$$E^{(2)} = \sum_{i>j}^{occ} \sum_{a>b}^{vir} \frac{\langle \Phi_0 | \hat{H}^{(0)} | \Phi_{ij}^{ab} \rangle \langle \Phi_{ij}^{ab} | \hat{H}^{(0)} | \Phi_0 \rangle}{\epsilon_i + \epsilon_j - \epsilon_a - \epsilon_b} \quad (2.27)$$

Formally MP2 calculations scale as the fifth power of the number of basis functions ( $N^5$ ). The reason for this is found in the need of transforming from the atomic orbital

into the (orthonormal) molecular orbital basis.

In order to reduce the scaling different techniques can be used. One popular technique is the combination with the resolution of the identity (RI) approach. As already mentioned in the chapter dealing with the FOCI-AM1 approach (Sec. 2.1, p. 11), the evaluation of two-electron multi-center integrals introduced by the Fock operator is computationally expensive during the SCF-cycle. Introducing what is called the Mulliken notation these integrals take on the following form

$$(ij|kl) = \int \chi_i(r_1)\chi_j(r_1)\frac{1}{|r_1-r_2|}\chi_k(r_2)\chi_l(r_2)d^3r_1d^3r_2 \quad (2.28)$$

The ansatz for simplifying starts by introducing an additional auxiliary orthonormal basis, labeled  $|m\rangle$  via the resolution of the identity

$$I = \sum_m |m\rangle\langle m| \quad (2.29)$$

Inserting  $I$  into Eq. 2.28 right before the  $1/r_{12}$  operator yields

$$\begin{aligned} (ijI|kl) &= \sum_m (ijm)(m|kl) \\ (ijm) &= \int \chi_i(r_1)\chi_j(r_1)\chi_m(r_1)d^3r_1 \\ (m|kl) &= \int \chi_m(r_1)\frac{1}{|r_1-r_2|}\chi_k(r_2)\chi_l(r_2)d^3r_1d^3r_2 \end{aligned} \quad (2.30)$$

turning the four-index two-electron integral  $(ij|kl)$  into a sum of three-index one-electron overlap  $(ijm)$  and three-index two-electron repulsion  $(m|kl)$  integrals. Although the modification seems to be a minor one, the consequences are drastic: Not only the evaluation of the integrals is speeded up significantly but also the required storage is decreased. The three index overlap integrals  $(ijm)$  are extremely inexpensive to compute. While the three-center repulsion integrals are more expensive, they still are significantly less expensive than the original four-index integrals.<sup>33</sup> In addition the total number of three-center integrals is far less than the total number of four-center integrals.

In summary the scaling of Hartree-Fock is reduced from  $N^4$  to  $N^2m$  with  $m$  being the number of auxiliary basis functions. From this scaling it becomes obvious that a speedup can only be achieved if the auxiliary basis is small compared to the squared

number of conventional basis functions, which is easily achieved using modern auxiliary basis sets.<sup>34</sup> If combined with MP2, the RI-approximation results in another benefit, since the transformation into the orthonormal molecular orbital basis only scales as  $N^4$  in contrast to the initial scaling of  $N^5$ .

RI-MP2 is reported to perform best with large-scale calculations. An outstanding example was reported by Bernholdt and Harrison with an astonishing reduction of 94% in CPU time relative to conventional MP2 for the binding energy of  $K^+$  to a 12-crown-4 ether. In this calculation no loss of accuracy(!) in the resulting binding energy was found.<sup>35</sup> A more comprehensive overview of typical errors introduced by the RI-approximation was given by Ahlrichs and coworkers<sup>36</sup> who tested their auxiliary basis sets with a benchmark set of 368 small molecules. The common oxidation states of all elements were taken into account by at least one compound. A comparison against standard MP2/(SVP, TZVP, TZVPP) calculations yielded errors not larger than  $60 \mu E_h$  (0.16 kJ/mol) per atom for 90% of the structures.<sup>(9)</sup> As for the resulting geometries the errors were less than 0.2 pm in any case, leading to the authors conclusion that the loss of accuracy introduced by the RI-ansatz is insignificant.

For the purpose of illustrating dimensions: The RI-MP2 calculations employed in this thesis featured an augmented triple zeta basis for 48 atoms. The dimension of the orbital basis was 738 with a total of 2562 auxiliary basis functions. The typical time for computation was as small as  $\sim 20h$ .

## DFT-D

This section deals with a quantum-mechanical method termed long-range dispersion-corrected density functional theory (DFT-D). In the following, a short overview of density functional theory is given, before the B97 functional and the dispersion correction are discussed.

Density functional theory is based on the famous theorem by Hohenberg and Kohn,<sup>26,32</sup> showing that a one-to-one correspondence between the electron density  $\rho(x, y, z)$  and the total energy of a system exists. The most obvious advantage of this ansatz is the reduction of complexity achieved by replacing the inherently multi-dimensional wavefunction with the electron density that depends only on three spatial coordinates.

---

<sup>(9)</sup>No error was found bigger than  $120 \mu E_h$  (0.32 kJ/mol) per atom

In fact the general form of the - still unknown - exact energy functional  $E[\rho]$  is given as

$$\begin{aligned} E[\rho(r)] &= E_{ne}[\rho] + T[\rho] + E_{ee}[\rho] \\ &= E_{ne}[\rho] + T[\rho] + J[\rho] + X[\rho] \end{aligned} \quad (2.31)$$

where  $E_{ne}[\rho]$  denotes the Coulomb interaction between electrons and nuclei,  $T[\rho]$  the kinetic energy of the electrons and  $E_{ee}[\rho]$  the electron-electron interaction energy. Linking to Hartree-Fock,  $E_{ee}[\rho]$  can be decomposed into a Coulomb term,  $J[\rho]$  and a term corresponding to the (non-classical) exchange term,  $X[\rho]$ . While the nuclei-electrons coulomb interaction and the coulomb interaction between electrons can be expressed by the classical expressions

$$\begin{aligned} E_{ne}[\rho(r)] &= - \sum_a^{N_{nuclei}} \int \frac{Z_a(R_a)\rho(r)}{|R_a - r|} dr \\ J[\rho(r)] &= \frac{1}{2} \int \int \frac{\rho(r)\rho(r')}{|r - r'|} dr dr' \end{aligned} \quad (2.32)$$

the expressions for the kinetic energy,  $T[\rho]$ , and the exchange functional  $X_\rho$  are not known. Numerous attempts were made to develop a formalism that is based exclusively on the electron density, all of which failed to date. The lack of accuracy rendered these models not usable for the purpose of solving chemical problems. Especially the kinetic energy of the electrons proved to be a critical point in the models.

It was not until W. Kohn and L. J. Sham re-introduced the wavefunction that DFT could gain the popularity it exhibits today. In order to re-introduce a wavefunction, a reference system without electron-electron repulsion is constructed and described with the following Hamiltonian

$$\hat{H}_s = \sum_i \left( -\frac{1}{2} \nabla_i^2 \right) + E_{ne} \quad (2.33)$$

where the first term in the sum gives the kinetic energy of the electrons and  $E_{ne}$  the potential energy of the electrons in the field of all nuclei. The solution of the reference system is exactly a Slater determinant, since the electrons are non-interacting. If  $\Psi_{SD}$  denotes the Slater determinant and  $\psi_i$  the molecular orbitals, the kinetic energy is exactly given by

$$\begin{aligned} T_s[\rho] &= \langle \Psi_{SD} | \sum_i \left( -\frac{1}{2} \nabla_i^2 \right) | \Psi_{SD} \rangle \\ &= \sum_i \langle \psi_i | -\frac{1}{2} \nabla_i^2 | \psi_i \rangle \end{aligned} \quad (2.34)$$

with the help of the above equation, the expression for the total energy becomes

$$E[\rho(r)] = E_{ne}[\rho] + T_s[\rho] + J[\rho] + E_{xc}[\rho] \quad (2.35)$$

where  $E_{xc}[\rho]$  is the so called exchange-correlation functional. The new functional,  $E_{xc}[\rho]$ , not only accounts for the exchange functional, labeled  $X[\rho]$  above, but also for the error introduced by the non-interacting electrons assumption. Although the dimensionality is raised again by re-introducing a wavefunction, the Kohn-Sham approach is extremely successful. The main reasons are that the search is reduced to only one functional and already rough approximations for  $E_{xc}$  result in significantly more accurate results compared to wavefunction-free DFT models. Finally, the rather simple wavefunction<sup>(10)</sup> does increase the complexity of the ansatz, but cannot be compared to the extremely complex wavefunctions used in modern wavefunction-based correlation methods.

The B97-D functional used in this thesis consists of a generalized gradient approximation functional presented by Becke in 1997 (B97)<sup>37</sup> and an additional (semi)empirical correction term for the dispersion correction introduced by Grimme.<sup>38</sup> The general gradient approximation refers to exchange-correlation functionals that include not only the local electron density but also the gradient of the electron density. In short, the functional is given by

$$E_{xc} = E_x + E_{C\alpha\beta} + \sum_{\sigma} E_{C\sigma\sigma} \quad (2.36)$$

where the labels  $x$  and  $c$  mark the exchange and correlation contributions and  $\sigma$  a spin variable denoting  $\alpha$  or  $\beta$  spin. The single terms depend on the gradient of the electron density  $\rho_{\sigma}$  via the reduced gradient variable  $s_{\sigma}$

$$\begin{aligned} s_{\sigma} &= \frac{\nabla \rho_{\sigma}}{\rho_{\sigma}^{4/3}} \\ E_x &= \sum_{\sigma} \int e(\rho_{\sigma}) g_{X\sigma}(s_{\sigma}^2) dr \\ E_{C\alpha\beta} &= \int e(\rho_{\alpha}\rho_{\beta}) g_{C\alpha\beta} \left( \frac{1}{2}(s_{\alpha}^2 + s_{\beta}^2) \right) dr \\ E_{C\sigma\sigma} &= \int e(\rho_{\sigma}) g_{C\sigma\sigma}(s_{\sigma}^2) dr \end{aligned} \quad (2.37)$$

the  $e(\rho)$  terms are the (analytically known) local energy densities of a uniform electron gas, while  $g$  denotes the gradient correction factors. The prominent feature of Beckes ansatz manifests in the gradient correction factors that are expanded in a power series

<sup>(10)</sup>The complexity of the Kohn-Sham wavefunctions is comparable to the Hartree-Fock wavefunction.

containing essentially the reduced electron density  $s^2$ . As an example,  $g_{x\sigma}(s^2)$  is given by

$$\begin{aligned} g_{x\sigma}(s^2) &= \sum_{j=0}^2 c_j u_{x\sigma}^j(s^2) \\ u_{x\sigma}^j(s^2) &= \frac{\gamma_{x\sigma} s_\sigma^2}{1 + \gamma_{x\sigma} s_\sigma^2} \end{aligned} \quad (2.38)$$

where  $c_j$  and  $\gamma_{x\sigma}$  are empirical fit parameters. The functional form of the remaining two  $u(s^2)$  terms in Eq. 2.37 take on the same functional form. However, their individual  $c$  and  $\gamma$  parameters have to be fitted as well. While the parameters  $\gamma$  remain Beckes original set of parameters the  $c$  parameters were re-fitted by Grimme upon the addition of the dispersion correction.

The dispersion correction introduced by Grimme modifies the total energy by adding a dispersion term  $E_{\text{disp}}$ .

$$E_{\text{B97-D}} = E_{\text{B97}} + E_{\text{disp}} \quad (2.39)$$

Although the above is written for the case of the B97 functional, the correction can be added to any Kohn-Sham DFT energy. The empirical dispersion correction is given by

$$E_{\text{disp}} = -s_6 \sum_{i=1}^{N_{at}-1} \sum_{j=i+1}^{N_{at}} \frac{C_6^{ij}}{R_{ij}^6} f_{\text{damp}}(R_{ij}) \quad (2.40)$$

here  $N_{at}$  is the total number of atoms in the system,  $R_{ij}$  the interatomic distance,  $C_6^{ij}$  the dispersion coefficient between two atoms  $i$  and  $j$  and  $s_6$  a global scaling factor. In order to avoid singularities caused by small interatomic distances a damping function  $f_{\text{damp}}^{(11)}$  is used

$$f_{\text{damp}}(R_{ij}) = \frac{1}{1 + e^{-20(R_{ij}/R_r - 1)}} \quad (2.41)$$

the damping function depends on the sum of atomic van der Waals radii obtained from electron densities computed with restricted-open shell Hartree-Fock (ROHF)/TZV calculations. The dispersion coefficients,  $C_6^{ij}$  are decomposed into the geometric mean of atomic parameters

$$C_6^{ij} = \sqrt{C_6^i C_6^j} \quad (2.42)$$

---

<sup>(11)</sup>In addition the dispersion correction should only contribute to the long-range asymptotic regions since DFT is already capable of describing the short-range interactions.

The atomic parameters are in turn parametrized using atomic ionization potentials  $I_p$  and static dipole polarizabilities  $\alpha$  taken from PBE0/QZVP calculations

$$C_6^a = 0.05NI_p^a\alpha^a \quad (2.43)$$

with  $N$  taking values of 2,10,18,36 and 54 for atoms from rows 1-5 of the periodic table. The parameters were fitted using a least-squares optimization approach and a training set containing 30 atomization energies of selected molecules, 8 atomic ionization potentials, 3 proton affinities, 15 selected chemical reactions and 21 noncovalently bound complexes.<sup>38</sup>

According to Grimme the quality of the B97-D functional is remarkably high: It clearly outperforms the well known functionals BP86, BLYP, PBE, TPSS and B3LYP and "seems to yield structures and interaction energies for v.d.Waals complexes that deviate insignificantly from, e.g., those of CCSD(T) quality".<sup>38</sup> Finally, B97-D was found to accurately describe noncovalent complexes consisting of aromatic vs. saturated complexes, which corresponds to the *n*-hexane-brAB dimers studied in Chap. 7, p. 87.

## Quantum Mechanics/Molecular Mechanics

By combining quantum mechanical methods with classical molecular mechanics in what is called the Quantum Mechanics/Molecular Mechanics (QM/MM) approach, the study of large systems becomes possible. The initial idea can be traced back to Warshel and Levitt<sup>39</sup> and was recently awarded with the Nobel prize in chemistry. In most QM/MM approaches a part of the system that shall be studied in detail is described with a quantum mechanical method, while the rest - commonly referred to as the environment - is treated with molecular mechanics. However, since the initial formulation by Warshel and Levitt in 1976, the QM/MM ansatz has steadily been refined and extended. For example, a prominent successor of the initial QM/MM approach is found in the multilayer models (ONIOM)<sup>40</sup> routinely used today. Within the ONIOM model a QM<sub>1</sub>:QM<sub>2</sub>:MM ansatz is realized. The two quantum mechanical methods differ in computational cost and accuracy, offering a rather smooth transition in accuracy within one system.

The QM/MM method used throughout this thesis consists of a FOCI-AM1 QM-part and an OPLSAA-L MM-part. It is not limited to the case presented in Chap. 7, p. 87, where the surrounding solvent was chosen to be the environment, instead, the environment can also be a part of the same molecule as in the publication presented in Chap.6, p. 79, by using a modified connection atom approach put forward by Thiel

and coworkers.<sup>41,42</sup>

The electronic Hamiltonian used in the QM/MM ansatz is decomposed into three terms

$$\hat{H}_{el} = \hat{H}_{QM} + \hat{H}_{QM/MM} + E_{MM} \quad (2.44)$$

where  $\hat{H}_{QM}$  marks the Hamiltonian used for quantum subsystem,  $\hat{E}_{MM}$  the force field for the environment and  $\hat{H}_{QM/MM}$  the interaction between both. Following the same approach for the total energy of the systems one can also write

$$\begin{aligned} \hat{E}_{tot} &= E_{QM} + E_{MM} + E_{QM/MM} \\ &= \langle \Psi | \hat{H}_{QM} + \hat{H}_{QM/MM} | \Psi \rangle + E_{MM} \end{aligned} \quad (2.45)$$

Within the FOCI-AM1/OPLSAA-L method,  $\hat{H}_{QM}$  marks the FOCI-AM1 approach (see Sec. 2.1, p.11) and  $\Psi$  the FOCI-AM1 wavefunction.  $E_{MM}$  is taken to be the OPLSAA-L force field (see Sec. 2.1, p.7). The essential component of the QM/MM approach is given by the interaction between QM and MM subsystems described by  $\hat{H}_{QM/MM}$ . In the case of the FOCI-AM1/OPLSAA-L approach, the interaction for  $m$  MM-atoms with  $\alpha$  QM-atoms and  $i$  electrons is given in terms of electrostatic interactions as follows

$$\hat{H}_{QM/MM} = - \sum_{i,m} \frac{q_m}{R_{im}} + \sum_{\alpha,m} \frac{Z_\alpha q_m}{R_{\alpha m}} + \sum_{\alpha,m} \epsilon_{\alpha m} \left[ \left( \frac{\sigma_{\alpha m}}{R_{\alpha m}} \right)^{12} - \left( \frac{\sigma_{\alpha m}}{R_{\alpha m}} \right)^6 \right] \quad (2.46)$$

with  $q_m$  being the charge of an MM-atom,  $R_{im}$  or  $R_{\alpha m}$  distances between electrons or QM atoms and MM-atoms,  $Z_\alpha$  the nuclear charge of a QM-atom and  $\epsilon_{\alpha m}, \sigma_{\alpha m}$  the Lennard-Jones parameters for electrostatic interaction between a QM- and an MM-atom.

For the case of a chemically bound environment, the connection atom (CA) is used. The CA is included both in the force field and in the QM-Hamiltonian. For example MM-like terms (angle bending, torsion, bond stretch) are included if they involve the CA, at least one MM-atom and possibly one or two QM-atoms.<sup>42</sup> On the other hand, the CA is included into the QM-Hamiltonian by assigning one 2s-orbital<sup>(12)</sup> and a fractional core charge to it. The fractional core charge ( $q_{CA}$ ) is given by

$$q_{CA} = Q + 1 - \sum_m q_m \quad (2.47)$$

and depends on the charges of all MM-atoms ( $q_m$ ), the total charge of the molecule ( $Q$ ) and the fact that one electron of the CA is treated quantum mechanically. With

<sup>(12)</sup>Since a carbon atom is replaced, the basis function is of 2s form.



the above ansatz, even a polarization of the quantum mechanical bond is possible by assigning a core charge  $> 1$ . Finally the MM-part is influenced by electrostatic embedding of the connection atom using  $q_{CA}$  and the electronic densities already shown in Eq. 2.46.

While the last two terms in Eq. 2.46 are simply added to the final energy, the first term containing electrostatic interactions between MM-atoms and QM-electrons is added to the QM-Hamiltonian. By including the first term into  $\hat{H}_{QM}$ , i.e. adding the term before diagonalizing the Hamilton matrix, environmental spectral shifts become possible as well as displacements of conical intersections and avoided crossings along energy and coordinate axes, since the electronic wavefunction is directly affected by the electrostatics of the environment.

## 2.2 Dynamics

Before presenting the techniques and methods used for the simulation of molecular (photo)dynamics, two important concepts, the concept of the classical phase space and the density matrix, should be introduced. Consider a molecule consisting of  $N$  atoms. In order to precisely define the current state of the system, the three coordinates and the three components of momentum for every atom have to be known. Since the system contains  $N$  atoms, the total number of values needed is  $6N$ . Every possible combination of these  $6N$  coordinates spans a space known as the phase space. A point in phase space refers to one precisely defined state of the molecule<sup>(13)</sup> while its dynamics, i.e. the change of states with time, occur as a line or path.

While the concept of the phase-space originated in classical mechanics, the density matrix is a quantum-mechanical concept, very popular in semiclassical dynamics. Consider a two-state quantum system, if the system is found in precisely one state  $|1\rangle$  or  $|2\rangle$ , this is called a pure state. Due to the nature of quantum mechanics, the system could also be in a mixture of states, characterized by probabilities for the single states. For example, the system could be found in  $|1\rangle$  with a probability of 60% or in  $|2\rangle$  with a probability of 40%. The density matrix can nicely be used for the description of such mixed states. If  $|u_m\rangle$  form a set of basis functions, the density matrix for a quantum system with  $i$  states  $|\psi_i\rangle$  is given by

$$\rho_{mn} = \sum_i p_i \langle u_m | \psi_i \rangle \langle \psi_i | u_n \rangle \quad (2.48)$$

<sup>(13)</sup>In the language of statistical mechanics, a point in phase space is termed a microstate.

where  $p_i$  would correspond to the probabilities 60:40 mentioned in the two-state example above. The expectation value of any operator  $\hat{A}$  can be calculated by the trace of the product of density matrix and operator:  $tr(\rho\hat{A})$ . The latter operation can nicely be illustrated by noticing that the classical analogue of the density matrix is found in the probability distribution of positions and momenta ( $\rho(p, q)$ ) in phase space. From this probability distribution the average of an observable  $A(p, q)$  is calculated as

$$\langle A \rangle = \int_{-\infty}^{\infty} \int_{-\infty}^{\infty} A(p, q) \cdot \rho(p, q) dq dp \quad (2.49)$$

which corresponds to summing up the (probability weighted) observable for every point in phase-space.

## Molecular Dynamics

Molecular dynamics is a popular and widely used simulation technique that is treating the movement of the atoms like the movement of classical particles. In principle molecular dynamics can be run on any kind of potential energy surfaces, analytic (force fields) or *ab-initio* surfaces (AIMD),<sup>26,32,43</sup> although the term molecular dynamics (MD) often implies that a force field is used.

The dynamics of the internal degrees of freedom ( $Q$ ) for any molecule, obtained by solving Newton's equation of motion, are called a classical trajectory ( $Q(t)$ ). In contrast to the dynamics of quantum particles that obey the quantum mechanical equations of motion, trajectories of classical particles are localized in phase space at any given time  $t$ . The latter point is of great importance for the semiclassical dynamics presented below.

The most common technique for integration of classical trajectories is called the Verlet algorithm. Since the dynamics presented in this work were calculated with a slightly modified Verlet algorithm,<sup>44</sup> a short derivation of the applied algorithm is presented in the following.<sup>(14)</sup> In order to obtain the nuclear trajectory at one time step later ( $t + \Delta t$ ), we start by constructing a Taylor expansion around  $Q(t)$

$$\begin{aligned} Q(t + \Delta t) &= Q(t) + \dot{Q}(t)\Delta t + \frac{\Delta t^2}{2}\ddot{Q}(t) + \frac{\Delta t^3}{6}\dddot{Q}(t) + \mathcal{O}(\Delta t^4) \\ &= Q(t) + v(t)\Delta t + \frac{\Delta t^2}{2}a(t) + \frac{\Delta t^3}{6}\dot{a}(t) + \mathcal{O}(\Delta t^4) \end{aligned} \quad (2.50)$$

<sup>(14)</sup>The main difference between the standard simple Verlet algorithm and the current one is simply a truncation of the Taylor series after the cubic term, instead of a truncation after the quadratic term.

where the time derivatives  $\dot{Q}(t)$  and  $\ddot{Q}(t)$  mark the velocity ( $v$ ) and the acceleration ( $a$ ). Next, a corresponding Taylor expansion around the future trajectory point  $Q(t + \Delta t)$  for the current point  $Q(t)$  is constructed

$$\begin{aligned} Q(t) &= Q(t + \Delta t) - \dot{Q}(t + \Delta t)\Delta t + \frac{\Delta t^2}{2}\ddot{Q}(t + \Delta t) - \frac{\Delta t^3}{6}\dddot{Q}(t + \Delta t) + \mathcal{O}(\Delta t^4) \\ &= Q(t + \Delta t) - v(t + \Delta t)\Delta t + \frac{\Delta t^2}{2}a(t + \Delta t) - \frac{\Delta t^3}{6}\dot{a}(t + \Delta t) + \mathcal{O}(\Delta t^4) \end{aligned} \quad (2.51)$$

Summing of both equations yields an expression for the velocity at the next trajectory point

$$\begin{aligned} \dot{Q}(t + \Delta t) &= v(t + \Delta t) \\ &= \dot{Q}(t) + \frac{\Delta t}{2} [\ddot{Q}(t) + \ddot{Q}(t + \Delta t)] + \frac{\Delta t^2}{6} [\dddot{Q}(t) - \dddot{Q}(t + \Delta t)] + \mathcal{O}(\Delta t^3) \\ &= v(t) + \frac{\Delta t}{2} [a(t) + a(t + \Delta t)] + \frac{\Delta t^2}{6} [\dot{a}(t) - \dot{a}(t + \Delta t)] + \mathcal{O}(\Delta t^3) \end{aligned} \quad (2.52)$$

The acceleration within Eq. 2.50 and Eq. 2.51 is obtained as the negative gradient of the potential  $V(Q)$

$$\begin{aligned} F &= ma \\ a &= \frac{F}{m} = -\frac{1}{m} \frac{\partial V(Q)}{\partial Q} \end{aligned} \quad (2.53)$$

while the first derivatives of the acceleration  $\dot{a}(t)$  and  $\dot{a}(t + \Delta t)$  are calculated by first order approximations

$$\dot{a}(t) = \frac{a(t) - a(t - \Delta t)}{\Delta t} + \mathcal{O}(\Delta t^2) \quad (2.54)$$

With this final approximation Eq. 2.50 and Eq. 2.52 can be rewritten as

$$\begin{aligned} Q(t + \Delta t) &= Q(t) + v(t)\Delta t + \Delta t^2 \left[ \frac{2}{3}a(t) - \frac{1}{6}a(t - \Delta t) \right] + \mathcal{O}(\Delta t^4) \\ v(t + \Delta t) &= v(t) + \Delta t \left[ \frac{5}{6}a(t) + \frac{1}{3}a(t + \Delta t) - \frac{1}{6}a(t - \Delta t) \right] + \mathcal{O}(\Delta t^3) \end{aligned} \quad (2.55)$$

Since the initial equations of motion are second-order differential equations in  $Q(t)$ , the calculation of a trajectory requires two initial values, i.e. the positions and initial velocities. The trajectory is finally obtained by repeated application of Eq. 2.55. The

resulting order of accuracy for a given time interval is  $\mathcal{O}(\Delta t^3)$  for the positions  $Q(t)$  and  $\mathcal{O}(\Delta t^2)$  for the velocities  $v(t)$ .

While the above version of the Verlet algorithm was used in the actual surface-hopping dynamics, the ground-state Brownian dynamics followed a different approach. In order to simulate the ground-state Brownian dynamics an integration of the Langevin equation was applied

$$\dot{P}_\alpha = -\gamma_\alpha P_\alpha - \frac{\partial E_K(\vec{R})}{\partial R_\alpha} + X_\alpha(t) \quad (2.56)$$

where the conjugate momentum of the  $R_\alpha$  nuclear coordinate is given by  $P_\alpha = m_\alpha \dot{R}_\alpha$ . The friction coefficient,  $\gamma_\alpha$  determines the associated viscosity of the solvent (see below) and  $X_\alpha(t)$  a Gaussian random white noise. The friction coefficient is linked to the Gaussian white noise via its autocorrelation function

$$\langle X_\alpha(0) X_\beta(t) \rangle = 2m_\alpha \gamma_\alpha kT \delta_{\alpha\beta} \delta(t) \quad (2.57)$$

The equations of motion implemented into the MOPAC2002<sup>45</sup> development version by Persico and coworkers<sup>46</sup> follow the approach of van Gunsteren and Berendsen.<sup>47</sup>

## Semiclassical surface-hopping dynamics

Semiclassical theory is a concept used for obtaining approximate solutions for quantum mechanical problems. In principle, the central assumption used in semiclassical theory is based on the correspondence principle, first formulated by Nils Bohr in 1920.<sup>48</sup> The correspondence principle states that the quantum theory must reproduce the classical results in the limit of large quantum numbers, i.e. high energies. From the view of dynamics this establishes a correspondence between the dynamics of a wave packet, obtained from an exact solution of the time-dependent Schrödinger equation, and an ensemble of classical particles.

Since the formulation of the correspondence principle, numerous studies on this quantum classical boundary have been presented. Among them are famous examples like the propagation of frozen Gaussian wave packets along classical paths as presented by Heller,<sup>49</sup> as well as the Ehrenfest method that propagates a "classical" trajectory on an effective potential given by the energy expectation value of a quantum system.<sup>50</sup> The semiclassical ansatz used throughout this thesis was introduced by John C. Tully in 1990<sup>(15)</sup> and is termed fewest-switching surface-hopping dynamics.<sup>50,51</sup> Its

<sup>(15)</sup>Historical note: Fewest-switches surface-hopping was developed during Tully's stay at the famous AT&T Bell laboratories.

derivation and essential features are outlined below. However, the original publication "Molecular dynamics with electronic transitions" by Tully<sup>51</sup> is strongly advised to the interested reader.

The basic objective of surface-hopping dynamics is combining fast and efficient classical molecular dynamics with electronic transitions. Since the solutions of the classical equations of motion correspond to localized lines/points in phase space, an ensemble of trajectories is propagated, such that the ensemble average adapts to the quantum mechanical solution.

Let  $R$  be the atomic coordinates and  $r$  the electronic coordinates, then the total Hamiltonian can be written as

$$H = T_R + H_0(r, R) \quad (2.58)$$

where  $T_R$  is the kinetic energy operator of atomic motion and  $H_0(r, R)$  the electronic Hamiltonian. By assuming that the atoms move on a trajectory  $R(t)$ , the electronic Hamiltonian becomes a time-dependent operator through its dependence on  $R$ . In order to construct a time-dependent wavefunction, a linear combination of arbitrary, but orthonormal, electronic basis functions is made

$$\begin{aligned} \psi(r, R, t) &= \sum_j c_j(t) \phi_j(r; R) \\ c_j &\in \mathbb{C} \quad \text{and} \quad \langle \phi_i | \phi_j \rangle = \delta_{ij} \end{aligned} \quad (2.59)$$

Inserting Eq. 2.59 into the time-dependent Schrödinger equation, multiplying from the left by  $\phi_k(r; R)$  followed by an integration over the electronic coordinates  $r$  yields the change of the expansion coefficients with time

$$\begin{aligned} i\hbar \dot{c}_k &= \sum_j c_j \left( \langle \phi_k(r; R) | H_0(r, R) | \phi_j(r; R) \rangle - i\hbar \dot{R} \cdot \langle \phi_k(r; R) | \nabla_R | \phi_j(r; R) \rangle \right) \\ &= \sum_j c_j \left( V_{kj}(R) - i\hbar \dot{R} d_{kj} \right) \end{aligned} \quad (2.60)$$

with the non-adiabatic coupling vector  $d_{kj}$  and the matrix elements of the electronic Hamiltonian  $V_{kj}$ . Eq. 2.60 is known as the standard classical path method result. The coupled set of differential equations can be integrated along a trajectory  $R(t)$  to yield the expansion coefficients  $c_j$  for each electronic state. Within Eq. 2.60 both the off-diagonal matrix elements of the electronic Hamiltonian and the non-adiabatic coupling vector can cause transitions between electronic states.

Given that we are interested in the probability of a state being populated or not, a reformulation in terms of the density matrix is sensible. The density matrix is defined by

$$\rho_{kj} = c_k c_j^* \quad (2.61)$$

Substitution of the expansion coefficients with the density matrix in Eq. 2.60 yields an equation for the time evolution of the density matrix elements.

$$i\hbar\dot{\rho}_{kj} = \sum_i (\rho_{ij} [V_{kl} - i\hbar\dot{R} \cdot d_{kl}] - \rho_{kl} [V_{lj} - i\hbar\dot{R} \cdot d_{lj}]) \quad (2.62)$$

In order to derive the above equation, the following properties of a set of orthonormal basis functions was used

$$\begin{aligned} d_{ij}^* &= -d_{ji} \\ d_{jj} &= 0 \end{aligned} \quad (2.63)$$

From Eq. 2.62, the diagonal elements of the density matrix  $\rho_{kk}$ , i.e. the probability to find the system in state  $k$ , depend on the off-diagonal elements  $\rho_{kl}$ , the coherences, via the following equations

$$\begin{aligned} \dot{\rho}_{kk} &= \sum_{l \neq k} b_{kl} \\ b_{kl} &= \frac{2}{\hbar} \Im(\rho_{kl}^* V_{kl}) - 2\Re(\rho_{kl}^* R \cdot d_{kl}) \end{aligned} \quad (2.64)$$

In order to obtain a procedure for self-consistent selection of the real-valued trajectory  $R(t)$ , Tully argued that a trajectory must only evolve on a single potential energy surface at any time. If the latter does not hold and the trajectory is propagated on an average surface, like for example in the Ehrenfest approach, situations where two surfaces represent drastically different states of the system are not treated correctly. The most prominent example is that of a dissociative state versus a bound state, where an average state between bound and dissociated is obviously physically senseless. State switches are then treated by changing the potential energy surface used in the propagation. These sudden switches, or surface-hops, are accompanied by a rescaling of the momenta to enforce energy conservation during the dynamics.

Having formulated the general idea of integrating Eq. 2.64 alongside a classical trajectory and accounting for electronic state switches by surface hops, the central question remains how to determine when an electronic state switch should occur. The first thing to notice is that surface-hops should occur as seldom as possible in order to prevent the ensemble average from proceeding on average potentials (see Fig. 2.1).

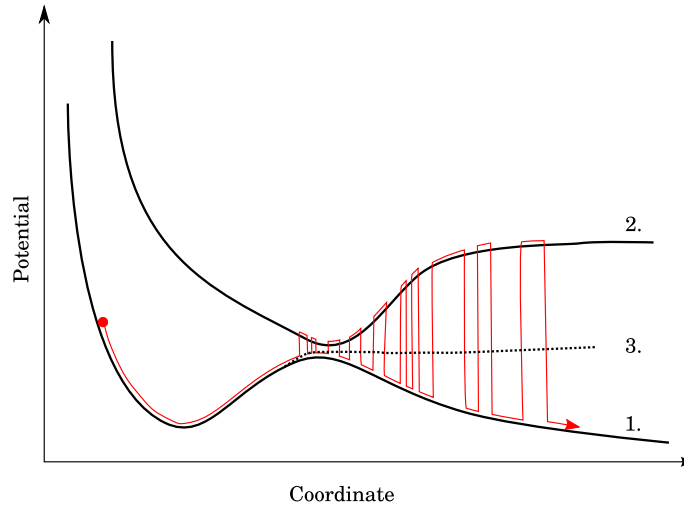


Figure 2.1: Scheme of a surface-hopping trajectory exhibiting too much switching.

Consider a simple two-state system and  $N$  independent nuclear trajectories at some time  $t$ . The trajectories correctly reflect the state populations  $N_{1,2}$  of the two states taken from the diagonal of the density matrix, i.e.  $N_1$  trajectories are found in state 1 and  $N_2$  trajectories are found in state 2.

$$\begin{aligned} N_1(t) &= \rho_{11}(t)N \\ N_2(t) &= \rho_{22}(t)N \end{aligned} \quad (2.65)$$

one (finite) time step  $\Delta t$  later the probabilities have changed slightly to  $\rho_{11}(t + \Delta t)$  and  $\rho_{22}(t + \Delta t)$

$$\begin{aligned} \rho_{11}(t + \Delta t) &< \rho_{11}(t) \\ \rho_{22}(t + \Delta t) &> \rho_{22}(t) \end{aligned} \quad (2.66)$$

indicating a population transfer from state 1 to state 2. In order to maintain the correct state distribution, some of the trajectories need to perform a surface hop. The fewest amount of switches, regardless of the amount of change in the diagonal of the density matrix, is achieved when all trajectories that currently evolve on state 2 stay in state 2 and the amount of trajectories required to reflect the new populations perform a surface hop from state 1 to state 2. The number of trajectories needed for compensation is given by the change of the density matrix diagonal element

$$(\rho_{11}(t + \Delta t) - \rho_{11}(t))N \quad (2.67)$$

The probability for one trajectory to perform a surface hop is obtained by dividing with the amount of trajectories that are currently found in state 1

$$\frac{(\rho_{11}(t) - \rho_{11}(t + \Delta t))N}{\rho_{11}(t)N} = \frac{(\rho_{11}(t) - \rho_{11}(t + \Delta t))}{\rho_{11}(t)} \quad (2.68)$$

For sufficiently small time steps,  $\Delta t \rightarrow dt$ , Eq. 2.68 can be rewritten in terms of the probability increase for state 2 to be populated ( $\dot{\rho}_{22}$ )

$$\frac{(\rho_{11}(t) - \rho_{11}(t + \Delta t))}{\rho_{11}(t)} \approx \frac{\dot{\rho}_{22}(t + \Delta t) \cdot \Delta t}{\rho_{11}(t + \Delta t)} \quad (2.69)$$

The probability for surface-hops now depends on the coherence via Eq.2.64 and the fewest switches criterion is fulfilled.

In order to start the propagation, initial positions and momenta have to be assigned. Note that due to the density matrix formulation, the initial state can also be a mixed state, though this is uncommon in surface-hopping dynamics. Once this is done the algorithm proceeds as follows:

1. The classical equations of motion for the nuclei are integrated for a small time step  $\Delta t$  on the according potential energy surface  $V_{kk}$ . The density matrix elements are integrated alongside via Eq. 2.62
2. The switching probabilities for all states are calculated from Eq. 2.69 and compared against a random number between one and zero.
  - If the random number is bigger than the probability a surface-hop to the according state occurs. The velocities are scaled to conserve the total energy and the trajectory is propagated on the new potential from new on. Continue with step 1.
  - If no switch occurs continue with step 1.
3. Terminate if trajectory is declared finished or some other suitable criteria is fulfilled.

The fewest switching surface hopping approach presented above is nowadays the most famous semiclassical dynamics ansatz. Despite its popularity, it still has some known drawbacks that will be discussed in the following. A minor drawback are the so called "frustrated surface-hops" that occur when the probabilities for a surface-hop are large and the trajectory should hop to another surface but cannot do so, because the energy difference between the surfaces is too large to be compensated by a scaling of the kinetic energy. Since total energy conservation is a strict criterion, these surface-hops are skipped. When estimating the quality of a surface-hopping trajectory the amount of frustrated surface-hops serves as a simple criterion: The less frustrated surface hops, the better the description of the photodynamics.



The most important drawback of surface-hopping dynamics is the inability to correctly describe quantum-decoherence. In other words, fewest-switching surface-hopping overestimates the quantum effect of interference. The reason for this surprising tendency can best be understood by comparing an ensemble of surface-hopping trajectories against the movement of wave packets as obtained from the 'exact' solution of the time-dependent Schrödinger equation, as sketched in Fig. 2.2.

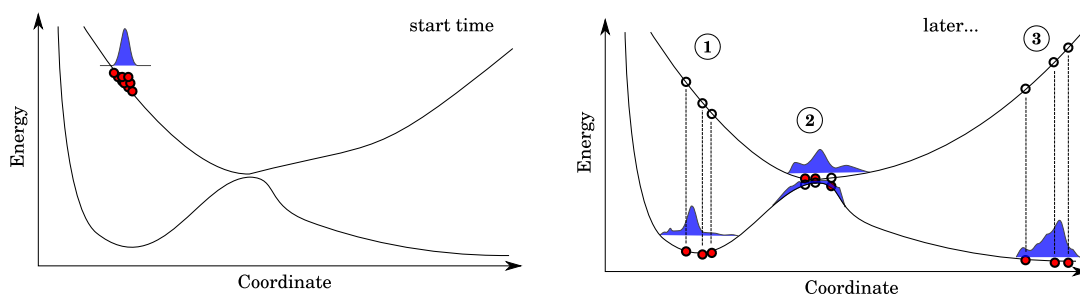


Figure 2.2: Simplified cartoon of the quantum-decoherence problem in surface-hopping dynamics. The red dots mark trajectories that reside on the current surface. The white dots connected with dotted lines mark possible points of interference, i.e. points where vertical surface-hops could occur, while the exact wavepacket solution is indicated in blue (see text for details).

In Fig. 2.2, a wave packet and an ensemble of trajectories, mimicking the initial wave packet, are depicted in the left panel. After the dynamics started, the wave packet starts to spread over the complete surface as do the trajectories. The central difference is that the wave packet typically interferes with itself, when a nonadiabatic event has transferred part of the population to another state (e.g. case 2, in Fig. 2.2). This quantum interference (usually) takes place on a rather short timescale, because all portions of the wave packet move individually on the surfaces and drift apart soon (case 2 vs. case 3 in the Figure), especially in higher dimensional cases. In contrast, the trajectories are always interfering for the whole simulation period, if the couplings do not vanish (as shown in cases 1 and 3 in the Figure), because the solid and blank circles cannot move individually. In a sense, the trajectories are exactly localized wave packets (points in phase space) that differ only by their amplitudes and can therefore constantly interfere.

The lack of quantum decoherence in surface-hopping dynamics is most fatal in regions where the energy difference between the surfaces is big.<sup>(16)</sup> In order to account for the decoherence effects Persico and coworkers implemented a correction term, initially proposed by Truhlar.<sup>52,53</sup> In this correction the surface-hopping probabilities are scaled as function of the energy difference between the surfaces. As a consequence

<sup>(16)</sup>This is why frustrated surface-hops are linked to missing quantum decoherence.

the probability for a surface hop decreases as the energy difference increases. Let  $k$  be the current state and  $P_l$  the probability for a surface hop to a state  $l$ , then the corrected probabilities can be computed from

$$\begin{aligned}
 P'_k &= P_k \left[ \frac{1 - \sum_{l \neq k} |P'_l|^2}{|P'_k|^2} \right]^{1/2} \\
 P'_l &= P_l e^{-\frac{\Delta t}{\tau_{kl}}}, \quad k \neq l \\
 \tau_{kl} &= \frac{\hbar}{|E_k - E_l|} \left( 1 + \frac{C}{E_{kin}} \right)
 \end{aligned} \tag{2.70}$$

where  $\Delta t$  is the time step,  $E_{kin}$  the nuclear kinetic energy and  $C$  an empirical constant. The correction term vanishes if the potential energy surfaces come close. If the surfaces are far apart, the probabilities for surface hops to other states are lowered, while the probability to stay in the current state is raised.

## 2.3 Trajectory analysis

### Electronic spectra

The calculation of static and time-resolved spectra from a set of surface-hopping trajectories was applied in every project presented in this work, simply because femtosecond time-resolved spectra offer the most direct experimental information on the photodynamics of a chromophore. The actual calculation of all spectra was carried out using a variety of PERL scripts written by the author and is based on the well-known Einstein coefficients. In order to keep this section focused, the reader is referred to the quoted literature or textbooks for a complete derivation of the Einstein coefficients. A very good azobenzene case study published by Granucci and coworkers<sup>54</sup> deals (in part) with the topic of calculating and interpreting electronic spectra from surface-hopping dynamics and is strongly recommended.

The calculation of spectra is best illustrated by discussing the simplest case, i.e. the calculation of time-resolved fluorescence spectra. In the case of fluorescence spectra, the Einstein coefficient for spontaneous emission,  $A_{21}$ , is the key quantity.

$$A_{L \rightarrow K} = \frac{4(E_L - E_K)^3 \mu_{LK}^2}{3\hbar^4 c^3} \tag{2.71}$$

$A_{L \rightarrow K}$  gives the probability for a system to spontaneously change from state L to a lower state K by emitting a photon with energy  $E_L - E_K$ . Apart from the reduced Planck constant,  $\hbar$ , and the speed of light,  $c$ , the value of  $A_{L \rightarrow K}$  exclusively depends on the cube

of the energy difference between the two states and the corresponding squared transition dipole moment,  $\mu_{LK}$ , which both are time-dependent quantities readily obtained from the surface-hopping trajectories. With the use of  $A_{L \rightarrow K}$ , the time dependent total emission rate,  $F(t)$  can be calculated from a set of  $N_T$  trajectories as follows:<sup>54</sup>

$$F(t) = \frac{1}{N_T} \sum_{i=1}^{N_T} \sum_{K=1}^{L_i-1} A_{L_i \rightarrow K} \quad (2.72)$$

where  $i$  numbers a single trajectory and  $L_i$  is the current electronic state at time  $t$  for the  $i$ th trajectory. In practice, a one-dimensional histogram, with time being the continuous variable, is set up and filled with the Einstein coefficients for every possible transition to a state lower than the current state, for all trajectories. After normalization with the total number of trajectories the total emission spectrum is obtained.

Total fluorescence quantum yields are easily obtained from the total emission rate by simply calculating the integral of  $F(t)$ :

$$\Phi_f = \int_0^{\infty} F(t) dt \quad (2.73)$$

Since the fluorescence quantum yields presented in this thesis are computed with the above procedure, a short information on units shall be given. From Eq. 2.71 the Einstein coefficient in SI units is given as

$$A_{L \rightarrow K} = \frac{J^3 \cdot C^2 \cdot m^2}{J^4 \cdot s^4 \cdot m^3 \cdot s^{-3}} = \frac{A^2 \cdot s^3}{kg \cdot m^3} \quad (2.74)$$

Due to a better comparison with spectroscopic experiments the more convenient wavenumbers were chosen for the Einstein coefficients and the computed fluorescence quantum yields:

$$A_{L \rightarrow K} = \frac{A^2 \cdot s^3}{kg \cdot m^3} \cdot \frac{(1m)^3}{(100cm)^3} = \frac{A^2 \cdot s^3}{kg \cdot 1 \cdot 10^6 cm^3} \quad (2.75)$$

Time-resolved spectra were calculated using an approach very similar to the above, with the only difference being that the continuous variable in the histogram is not the time but the energy gap between the current state and all states lower than the current state. The procedure can best be illustrated by a piece of pseudo code:

```

!Assemble the histogram
for each trajectory and every time step do
  for lower_state = current_state-1 until lower_state = ground_state do
    ΔE=current_state - lower_state;
    μ2 = μ2current_state→lower_state;
    compute Acurrent_state→lower_state(ΔE, μ2);
    F(ΔE) += Acurrent_state→lower_state(ΔE, μ2);
  end
end
!Normalize
for each entry in F(ΔE) do
  | entry = entry / (number_of_trajectories);
end

```

**Algorithm 1:** Pseudo code for the calculation of time-resolved fluorescence spectra from a set of surface-hopping trajectories.

In contrast to the emission spectra, absorption spectra, including static UV/Vis absorption spectra, presented in this work were calculated employing the Einstein coefficient for absorption of a photon

$$B_{K \rightarrow L} = \frac{2\pi^2}{3\epsilon_0 h^2} \cdot \mu_{K \rightarrow L}^2 \propto \mu_{K \rightarrow L}^2 \quad (2.76)$$

with the electric constant  $\epsilon_0$  and Planck's constant  $h$ . When combined with the spectral radiation density for isotropic radiation with frequency  $\nu$  at temperature  $T$  from Planck's law

$$\rho_\nu(\nu) = \frac{8\pi\nu^2}{c^3} \frac{h\nu}{e^{\frac{h\nu}{k_B T}} - 1} \quad (2.77)$$

the transition probability  $P_K$  from state K to a higher state L can be written as the product of the Einstein coefficient and the spectral radiation density.

$$\frac{dP_K}{dt} = B_{K \rightarrow L} \cdot \rho_\nu(\nu) \quad (2.78)$$

The actual calculation of spectra followed the binning techniques outlined above, apart from Eq. 2.78 being the quantity added to the bins of histograms.

## Pair radial distribution functions

The pair radial distribution functions are a concept widely used in the field of classical molecular dynamics (MD). It can best be understood when interpreted as the probability of finding a particle at a distance  $r$  from another particle. Since the probability is given relative to the ideal gas distribution,  $g(r)$  is a dimensionless quantity.<sup>32</sup>

Fig. 2.3 shows a typical radial distribution and the corresponding molecular setup in a cartoon-like manner. The sketch shown on the left of Fig. 2.3 represents a solvent

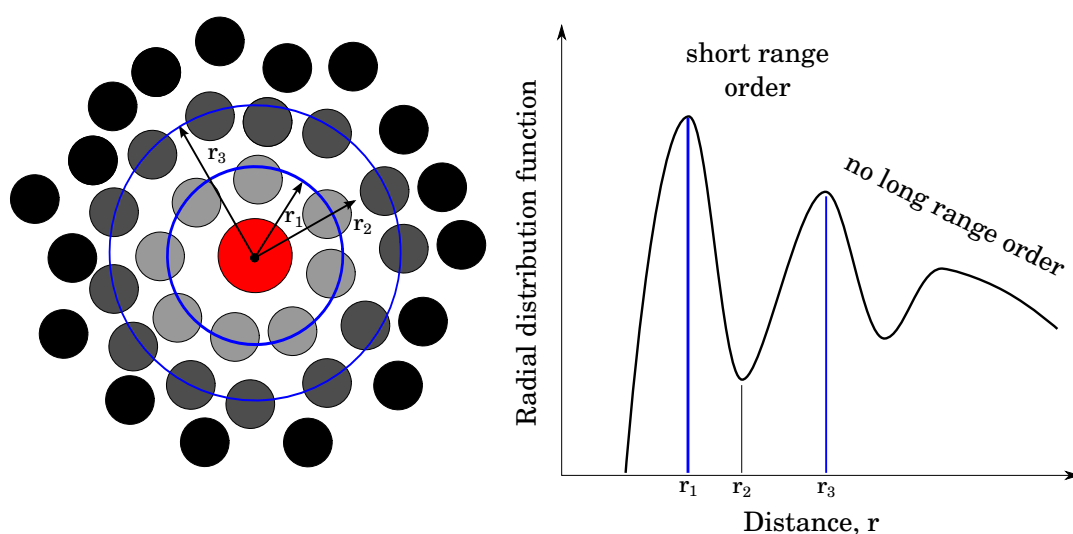


Figure 2.3: Cartoon of the pair radial distribution function as used in this thesis. The red circle marks the center of mass of the chromophore located at the center of the solvent sphere. The *n*-hexane solvent molecules are represented by their centers of mass and color coded: the darker the color the lower the solvent chromophore interaction.

sphere. The function shown on the right describes whether or not a particle is found at a distance  $r+dr$  relative to the red-marked reference particle at the center of the sphere. During a trajectory all particles are moving and the function is continuously updated for every new frame. The result is a probability distribution of finding a particle at distance  $r+dr$ , which is exactly the pair radial distribution function. If the reference particle and the solvent particles interact via for example van-der-Waals interactions a flexible but rather permanent solvent shell is formed that manifests itself in the first peak of the distribution function shown in Fig. 2.3. The peak stands for a short-range order caused by the attractive interaction between the reference particle and its first solvent shell.

The pair radial distribution function was used in this thesis in Chap. 7 on p. 87

for a description of brAB solvated in *n*-hexane. In order to be able to use the pair radial distribution function all molecules inside a trajectory movie were represented by their center of mass. The pair radial distribution function was then calculated using a VMD plugin.<sup>55</sup>

## Quantum yields

The calculation of quantum yields from an ensemble of surface-hopping trajectories is given by the fraction of trajectories reaching the product structure. Despite the simple nature of the simulated quantum yields, difficulties arise in practice because the product structures are usually vibrationally hot and exhibit strong oscillations that sometimes enable an escape from the product potential well. Commonly, this is accounted for in the dynamics by just stopping the dynamics once the product structure is reached. In the simulations presented in this thesis a different approach was chosen<sup>(17)</sup>: All trajectories were propagated for the same total time. The quantum yields were then computed using a PERL script.

The approach was chosen, because some gas phase trajectories of brAB were found to leave the product structure almost immediately, i.e. within some tens of femtoseconds. In addition, the *cis*-brAB structure cannot be identified using only the CNNC-dihedral due to the intermediate ground-state structure that also shows a dihedral angle of  $\approx 0^\circ$  (see Chap. 4 p. 59 for details). Instead, both the CNNC- and the CCCC-dihedral of the ethylenic bridge have to be taken into account in order to identify a vibrationally hot product structure. The oscillations were handled by assigning thresholds to the degrees of freedom.

The settings used for the calculation of the quantum yields were carefully chosen by checking against the trajectory movies, if the proposed classification into "reactive" and "unreactive" was correct. A typical setting as used in the QM/MM dynamics of brAB (see Chap. 7 p. 87 for details) for identifying the *trans*-isomer is:

- CNNC-dihedral  $> 113^\circ$  and  $< 163^\circ$  ( $138^\circ \pm 25\%$ )
- CCCC-dihedral (of the ethylenic bridge)  $> 61^\circ$  and  $< 141^\circ$  ( $101^\circ \pm 40\%$ )

The trajectory is considered reactive only if the product structure is reached and held for 50 frames (= 50fs). Note that due to the solvent cooling, escapes from the prod-

---

<sup>(17)</sup>Which is also a somewhat arbitrary stopping criterion.

uct potential well were not observed. The amount of required frames was therefore reduced to speed up the calculation.

## 2.4 Trajectory setup

### Gas phase dynamics

Starting from the optimized ground state structures of the azobenzene derivatives a ground state Brownian trajectory was calculated following the approach outlined in Sec. 2.2, p. 26. The temperature was set to 298.15 K and friction coefficients of  $\gamma = 1.35 \cdot 10^{13}$  were used. Snapshots of the dynamics were saved every 10 time steps, i.e. every femtosecond. In the FOCI-AM1 calculations the SCF convergence criterion was set to  $1 \cdot 10^{-11}$  a.u. with a floating-occupation number of 0.1 a.u. The chosen time step was 0.1 fs throughout all calculations.

The sampling of initial conditions for the surface-hopping dynamics was realized by randomly selecting structures from the movie file of the Brownian dynamics. In order to account for an equilibration period the first 10% of all structures were always discarded. Every frame preceding the first 10% was then selected with an equal probability of 0.05%. The probability was set empirically with the aim that the complete trajectory is read over about three times until the desired amount of starting structures is collected. This procedure was chosen because it prevents systematical sampling of certain intervals of the trajectory. The complete process was automatized with a PERL script and was used in every bachelor thesis apart from that of J. Müller.

Once the starting structures were assembled the surface hopping dynamics were started on the desired excited state, mostly  $S_1$ , without any initial momentum. During the surface-hopping dynamics the first four singlet states were included.

### QM/MM dynamics

The setup of the QM/MM dynamics presented in Chap. 7, p. 87 can be divided into two parts: The equilibration of the solvent box with molecular dynamics and the OPLSAA-L force field using TINKER<sup>56</sup> and the equilibration of the complete QM/MM setup, chromophore and solvent shell, with subsequent surface-hopping dynamics using MOPAC2002.<sup>45</sup>

The preparation of the solvent box followed the strategy outlined by Persico and

coworkers, who provided the *n*-hexane solvent box presented in Chap. 7, p.87. In order to visualize the procedure, the preparation of an own cyclohexane solvent box is described in the following. The starting structure of the box was constructed by aligning 1000 cyclohexane molecules in a 10x10x10 rectangle box. The OPLSAA-L force field was used for the simulation of one nanosecond of the ground-state dynamics in an NPT ensemble with the settings

- Time step: 1 fs
- Temperature: 298 K
- Pressure: 1 Atm.

An assessment of the force field and the setup was carried out via a comparison of experimental and simulated densities. Since the OPLSAA-L force field is optimized for the description of liquids, the simulated density of 0.7690 g/mL agrees with the experimental density of 0.7781 g/mL. Fig. 2.4 shows snapshots taken from the trajectory. Since the total of 1000 cyclohexane molecules is still too large for the QM/MM surface-

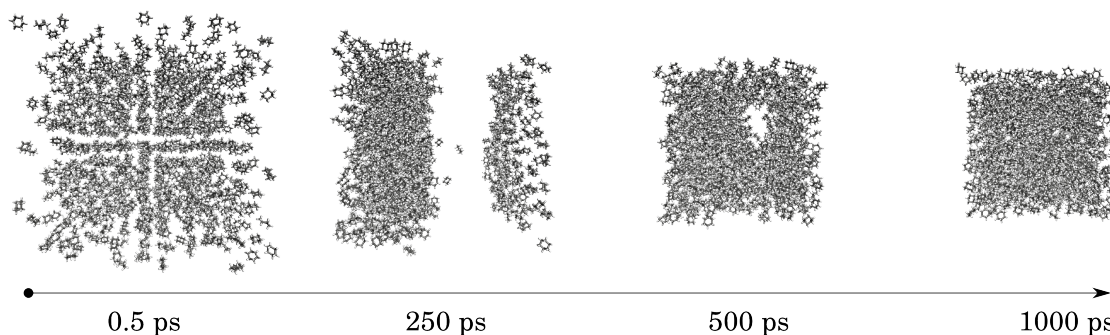


Figure 2.4: Snapshots from the OPLSAA-L/NPT molecular dynamics of the cyclohexane box.

hopping dynamics<sup>(18)</sup>, a sphere was cut around the center of the complete solvent box. The chromophore was finally inserted into the sphere, removing all solvent molecules that collided with the chromophore. As discussed in Chap. 7, p. 87 a collision can best be estimated by taking into account the van der Waals spheres of chromophores and solvent molecules. In total the final setup consisted of 182 cyclohexane molecules and brAB, i.e. 3304 atoms. Once the starting structure was constructed from the equilibrated solvent box the dynamics were calculated following the exact same strategy as with the gas phase dynamics discussed above.

<sup>(18)</sup>The setup was tested in ground state Brownian dynamics by the author.



## BACHELOR PROJECTS

As an introduction the basic problems and ideas leading to the bachelor theses presented within this chapter are outlined in the following section. The order of appearance in the following is not strictly chronological but grouped into topics starting off with force-related bachelor theses, that targeted existing or planned experiments. The Chapter concludes with two more stand-alone works. All setups and essential results of the bachelor projects are then summarized in the according sections.

All theses were supervised by the author in that the author introduced the students to all programs, supplied analysis tools, helped tackle technical problems and guided the interpretation of the results.

### 3.1 Introduction and overview

Whether or not molecular switches, like brAB, can in principle be used in molecular machines depends on a variety of properties. One of them was addressed in J. Müllers bachelor thesis,<sup>57</sup> namely the question if brAB is capable of performing a photoisomerization against an external force. Of course this is the analogue of asking what amount of work can be delivered by brAB. From the experimental side this question has been addressed in the Collaborative Research Center (SFB) 677 of the University of Kiel (SFB 677).<sup>58</sup> Most directly this is the case within the project A05 where a molecular switch is to be covalently linked between a surface and an atomic force microscope (AFM) cantilever at constant force, thus offering the perspective of quantitative

experimental data for the mechanical properties upon photoisomerization of a single molecular switch.

Besides the investigations on brAB carried out by J. Müller, the bachelor thesis of R. Scholz<sup>59</sup> aimed directly at the experimental setup of project A05. There AB was exposed to a constant external force and UV/Vis spectra were simulated targeting the question if and how these spectra change due to the external force, which is vital information for the experimental excitation. Besides the connection to project A05, the ansatz can also be used for predicting whether certain molecules act as mechanophores, i.e. if they change color upon mechanical stress. In the SFB 677, mechanophores are subject to future studies of the Staubitz and Adelung groups. It should be noted that both J. Müller's and R. Scholz's thesis are based on the pioneering work of S. Frick originating from an advanced practical course in the Hartke group.<sup>60</sup> During this practical course our development version of MOPAC was extended by the additional force terms needed in the above theses.

The thesis of T. Raeker,<sup>61</sup> that led to the publication discussed in Chap. 6, p. 79, also directly links to the SFB 677 as it dealt with the platform approach for surface mounted photoswitches proposed by Herges and coworkers.<sup>62–64</sup>

Another, also force-related, approach is the inclusion of AB into a polymer matrix, where the molecule is subject to intramolecular sterical stress<sup>(1)</sup> and presumably experiences notable restrictions on freedom of movement. From the experimental side this setup is addressed in sub-project A01 of the SFB 677 by the Temps group. Due to this project experimental data about the excited-states dynamics of an azobenzene derivative in a restrictive environment become available via time-resolved fluorescence experiments. This topic was addressed in the latest bachelor thesis by J. Steffen.<sup>65</sup>

The thesis of A. Kostevic dealt with brAB excitations into higher states. Within this work reaction pathways that result from excitations into the bright  $S_0 \rightarrow S_2$  band of the spectrum were analyzed. One motivation for this topic is of course the prominent role of higher excitations in AB photodynamics (see Chap. 1.2, p. Chap:Theory:AB). Results from this work were unfortunately affected by simultaneous results from multireference calculations of J. B. Schönborn that indicated significant differences in the electronic characters of the  $S_2$  and  $S_3$  states in AB and brAB.<sup>66</sup>

---

<sup>(1)</sup>As opposed to the solvent effect on brAB photoisomerization discussed in Chap. 7, p. 87

Whilst the above works were directly coupled to planned or existing experiments, the thesis written by R. Höppner<sup>67</sup> was dedicated to designing an improved photo-switch on the basis of brAB. Motivation for an attempt to improve brAB emerged from the reaction mechanism presented in Chap. 4 where gas-phase dynamics of brAB are discussed. There the ethylenic bridge was established as a mixed blessing, because it hinders the *trans*→*cis* isomerization and lowers the quantum yield of this reaction. In order to overcome this drawbacks while keeping the benefits, several different bridging patterns were simulated and a promising new molecule was proposed.

### 3.2 J. Müller: BrAB under the influence of an external force

The bachelor thesis of J. Müller entitled "Simulationen ultraschneller photochemischer Reaktionen eines verbrückten Azobenzols unter Einfluss externer Kräfte"<sup>57</sup> dealt with the question what amount of work can be delivered by the brAB photoisomerization following  $S_0 \rightarrow S_1$  excitation. In order to determine the work, two constant external forces were applied to the outer atoms of each phenyl ring pointing in opposite directions mimicking a clamped molecule. The quantum yields were determined by running a swarm of 90 surface-hopping trajectories for several different force values each, all of which were propagated for 3 ps. The maximum force against which brAB could isomerize was then estimated via a linear fit of quantum yield vs. force as depicted in Fig. 3.1, yielding a maximum force of  $368 \pm 44$  pN. The work can now be calculated according to the following equation (keeping in mind that forces and path are colinear by construction)

$$W_{\max} = |\vec{F}_{\max}| \cdot |\vec{s}| = 48.7 \pm 6.0 \text{ kJ/mol} \quad (3.1)$$

where  $\vec{F}_{\max}$  denotes the maximum force mentioned above and  $\vec{s}$  the difference in distance between the outer C-atoms of the phenyl rings of *cis*- and *trans*-isomer ( $=2.197\text{\AA}$ ). An analogous calculation on bare AB by S. Frick<sup>60</sup> resulted in  $W_{\max}=91.82$  kJ/mol which is roughly twice as much as in the case of brAB. This indicates that brAB, despite being a very efficient molecular switch, can be expected to be less powerful in terms of a molecular machine performing mechanical work. Very likely this is due to the ethylenic bridge. Support for this assumption can be found in Müller's thesis. There the dihedral angle of the ethylenic bridge acts particularly sensitive to the applied forces, while the CNNC dihedral is hardly effected. Obviously, with increasing force, the isomerization takes longer and longer, not because of the CNNC

dihedral angle but because of the rigid molecular framework. The movement of the CNNC-moiety caused by the photo-excitation has to be transferred to the ethylenic bridge via the phenyl rings. Due to a significant loss of vibrational energy in a realistic environment (see Chap. 7, p. 87) the struggle of overcoming the ground state barrier is more and more doomed to fail. Note that this relationships also show themselves in the *hula-twist* or *pedal movement* presented earlier, as the molecular framework can remain in its overall structure for a surprisingly long time, while the azo moiety performs the pedal movement. Another finding was made when Müller compared the average

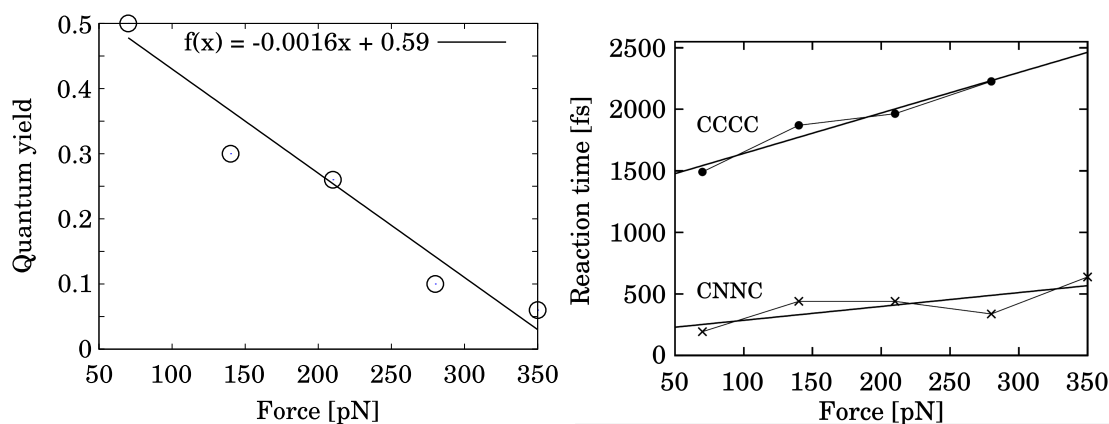


Figure 3.1: The left panel shows the plot of quantum yield against the external force applied and the linear fit used to estimate the maximum force, whilst the right panel shows the dependence of the isomerization time of CNNC and CCCC<sub>Br</sub> dihedrals on the external force (see text for details).

Data and right picture taken from.<sup>57</sup>

times needed for a successful isomerization that increased as the external force grew larger. The CNNC dihedral angle in the right panel of Fig. 3.1 visualizes these findings. Although not as clearly influenced by the force as the dihedral angle of the ethylenic bridge, the CNNC dihedral angle is influenced as well, despite exhibiting great flexibility due to its *hula-twist* option. These findings could give clues on the question of the very long reaction time of the cilium (as reported in Chap. 6, p. 79) and the prolonged fluorescence lifetimes of AB polymers (subject of Sec. 3.4). Unfortunately the effect of the force upon the excited-state lifetimes could not be addressed in the thesis due to lack of time.

### 3.3 R. Scholz: Effect of an external force upon the UV/Vis spectra of azobenzene

The bachelor thesis of R. Scholz entitled "Auswirkungen einer simulierten mechanischen Kraft auf ein schaltbares Molekül und dessen UV-Spektrum"<sup>59</sup> addresses the question of peak shifts in the UV/Vis spectra of a clamped AB molecule. The selected procedure combined a constant force ranging between zero and 5000 pN and a 20 ps long ground state trajectory for each isomer at room temperature, from which the UV/Vis spectra were calculated following the procedure lined out in Chap. 2.3, p. 34. Additionally a smaller set of trajectories was calculated employing the exact same approach except that the temperature was set to 70 K, simulating an experimental setup cooled with liquid nitrogen.

In order to estimate the force needed to dissociate AB, i.e. the upper force limit, the two isomers were treated with a force that was raised in a stepwise manner during the dynamics on the ground state surface. Not surprisingly it was found that the exact force amount depends on the rate of force increase. For example a rate of +30 pN every 150 fs resulted in a rupture of the bonds at 11010 pN for the *cis*- and 11610 pN for the *trans*-isomer, whilst a rate of +50 pN every 50 fs resulted in 12150 pN and 12200 pN accordingly. As this marks only a rough estimate, strictly limited by the simulation time scales and rates chosen, this should at maximum be interpreted as that the force needed for rupture of bonds within the AB molecule is presumably larger than 10000 pN. Note that all results refer to a force that was applied directly to the two outer C-atoms of the phenyl rings. Of course this cannot be achieved in a realistic experiment. There the AB is bonded to linker molecules on both sides. In such a setup the breaking points are very likely located within the linking molecules.

Regarding the UV/Vis spectra a general trend was found as the peaks experienced a red shift in direct comparison to the the spectra calculated without force. An example is shown in Fig. 3.2 that visualizes this red shift, showing clearly red-shifted and broadened peaks at a force of 1600 pN applied to the *cis*-isomer. Table 3.1 lists the results from the trajectories showing the maximal shifts for the first three peaks in the AB UV/Vis spectrum. Scholz also discusses a loss in intensity especially for the  $n \rightarrow \pi^*$  band. Although this might be an "observable" effect<sup>(2)</sup> it appears to the author that this is at least in parts caused by less sampling points per energy bin, due to the broadened

---

<sup>(2)</sup>Please note that, in the context of a single-molecule experiment as outlined in the introductory section 3.1, the term observable should not be taken literally.

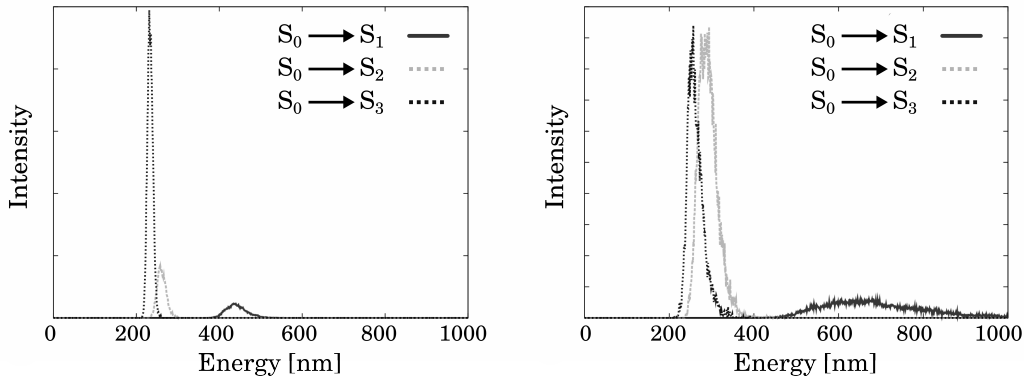


Figure 3.2: Simulated UV/Vis spectra according to Scholz. Left panel: Spectrum of the *cis*-isomer without any external force applied. Right panel: Spectrum of the *cis*-isomer at a constant force of 1600 pN.

Taken from.<sup>59</sup>

peaks, when calculating the distribution of vertical excitation energies from a long ground state trajectory. In general the intensities of the peaks should be examined critically, as they depend mainly on the unparametrized transition dipole moments (see Chap. 2.3, p. 34).

Table 3.1: Force dependence of the absorption maxima in the AB UV/Vis spectrum, according to Scholz. The labeling  $F_{\max}$  refers to the maximum force applied that did not result in bond rupture or isomerization, while the values given in parentheses mark the shift of the peak maximum.

<i>cis</i>	$S_0 \rightarrow S_1$	$S_0 \rightarrow S_2$	$S_0 \rightarrow S_3$
no force	435 nm	258 nm	231 nm
$F_{\max} = 1600$ pN	645 nm (+ 210 nm)	294 nm (+36 nm)	257 nm (+26 nm)
<i>trans</i>	$S_0 \rightarrow S_1$	$S_0 \rightarrow S_2$	$S_0 \rightarrow S_3$
no force	456 nm	285 nm	265 nm
$F_{\max} = 5000$ pN	499 nm (+ 43 nm)	284 nm (+1 nm)	265 nm (+0 nm)

Based on the above results Scholz fitted the peak positions employing a linear fit. The resulting formula allows for a rough estimate of the peak position of the *cis*-isomer as a function of the external force applied. For the  $S_0 \rightarrow S_1$  excitation the shifted peak position  $\lambda_{\max}(F)$  can thus be estimated by the following expression

$$\lambda_{\max}(F) = \lambda_{\text{no force}} + 1.289 \cdot 10^{-1} \frac{s^2}{g} \cdot F \quad (3.2)$$

where  $\lambda_{\text{no force}}$  is the peak position without any force and  $F$  the applied external force. As pointed out by Scholz this simple expression can be used for optimal  $S_0 \rightarrow S_1$

excitation. Apart from that, it could in principle be used for a rough estimate for the force an AB is subjected to. In fact this was the reason the author encouraged Scholz to check for the above analytical expression. Even when applying a rule of thumb like the more force the chromophore experiences the more red-shifted appears the  $n \rightarrow \pi^*$  peak, one could estimate simple relations (both experimentally and in simulations) for example between ABs embedded in polymer matrices with different branching ratios.

Yet another interesting question was addressed, when the trajectories of the *cis*-isomer that experienced a force-induced isomerization at forces greater than 2900 pN during the ground state dynamics and corresponding trajectories of the *trans*-isomers were compared. At such high forces the two isomers become unstable. Instead, only one *trans*-like distorted structure is found. Although this might seem intuitive this does not need to be the case, because due to different reaction paths on the ground state surface the isomers might as well have ended up in two different high-energy conformations or one of the isomers could have experienced a bond break, when approaching this structure. Based on the assumption that the FOCI-AM1 semiempirics are capable of capturing qualitative features of the AB ground state surface in such high-energy regimes, this would mean that all photoisomerization attempts were doomed to failure, as there exists only one distorted *trans*-like structure.

### **3.4 J. Steffen: QM/MM-simulation of the photodynamics of chromophores in polymers.**

The thesis by J. Steffen entitled "QM/MM - Simulation der Photodynamik von Chromophoren in Polymeren"<sup>65</sup> deals with the incorporation of the AB derivative 4,4'-Bis(acetamido)-azobenzene (BAAAB) into a poly(butyl methacrylate) (PBMA) polymer matrix. The whole project was initiated within sub-project A1 of the SFB 677 by the Temps group, and links to the area of sterical and mechanical interactions between a chromophore and its environment, which is obviously of utmost importance for any practical applications of molecular switches. The unpublished experimental data revealed a clear trend: When compared with the plain BAAAB chromophore, the pBAAAB showed a significantly increased fluorescence lifetime. The unknown mechanistic details behind this experimental observation mark the key question addressed in Steffens thesis.

The model system used in the simulations is depicted in Fig. 3.3. It consists of one BAAAB chromophore treated on the FOCI-AM1 level of theory and a saturated

surrounding PBMA polymer treated by the OPLSAA-L force field. The polymer was setup with a branching ratio of 1:10, i.e., one butanol bridging unit per ten monomers. As expected, the structures of *cis*- and *trans*-BAAAB are distorted upon incorporation

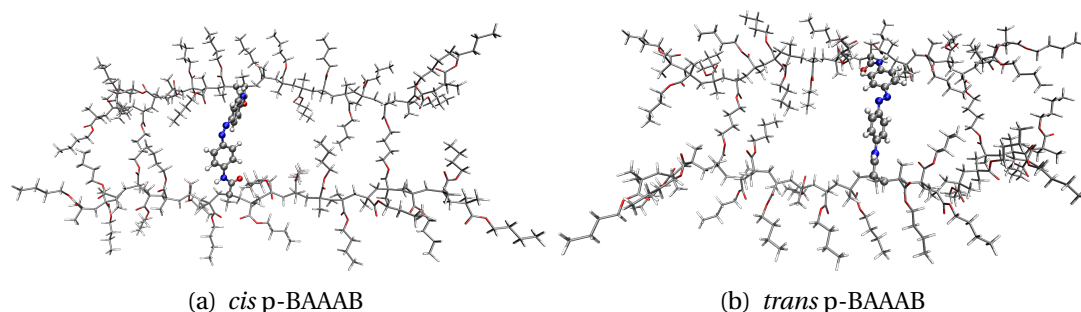


Figure 3.3: QM/MM model system (pBAAAB) used in the thesis of J. Steffen. The QM-part treated at FOCI-AM1 level of theory is shown as ball and stick, while the MM-part treated with the OPLSAA-L force field is depicted as wireframe.

Taken from.<sup>65</sup>

into the polymer. The *cis*-isomer was found to be clearly stretched with a total length difference of  $\approx 6\text{\AA}$  and adjusts to this external stress primarily by an opening of CNN angles. While the structure of the *cis*-isomer is stretched significantly, the structure of the *trans*-isomer is slightly compressed by  $\approx 2\text{\AA}$ . Interestingly, the *trans*-isomer reacts more sensitive to this compression by loosing its planarity: A phenyl ring is forced to rotate out of the molecular plane and the CNNC-dihedral angle is forced to close from  $180^\circ$  down to  $168^\circ$ . The effects on the equilibrium geometries are visualized in Fig. 3.4 below.

An analysis of the photoisomerization mechanisms for both isomers revealed that the photoisomerization starting from the *cis*-pBAAAB-isomer is not notably affected in terms of fluorescence lifetimes, but showed an increased quantum yield, compared to *cis*-BAAAB. The key steps in the isomerization mechanism of *cis*-pBAAAB involve an unchanged rotational movement of the CNNC-dihedral angle and an opening of the CNN-angles. Since the starting structure featured a slightly more opened CNNC-dihedral and significantly more opened CNN-angles, an effect of suitable pre-orientation is the likely cause for the increased quantum yields. The assumption also holds for the orientation of the phenyl rings, which is represented by the CCNN-dihedral angles, as the difference in the orientation of the phenyl rings between the two BAAAB isomers is smaller once they are embedded into the polymer. Clearly, the *cis* $\rightarrow$ *trans*-isomerization is promoted by the surrounding polymer.

The *trans* $\rightarrow$ *cis*-isomerization on the other hand is significantly hindered by the



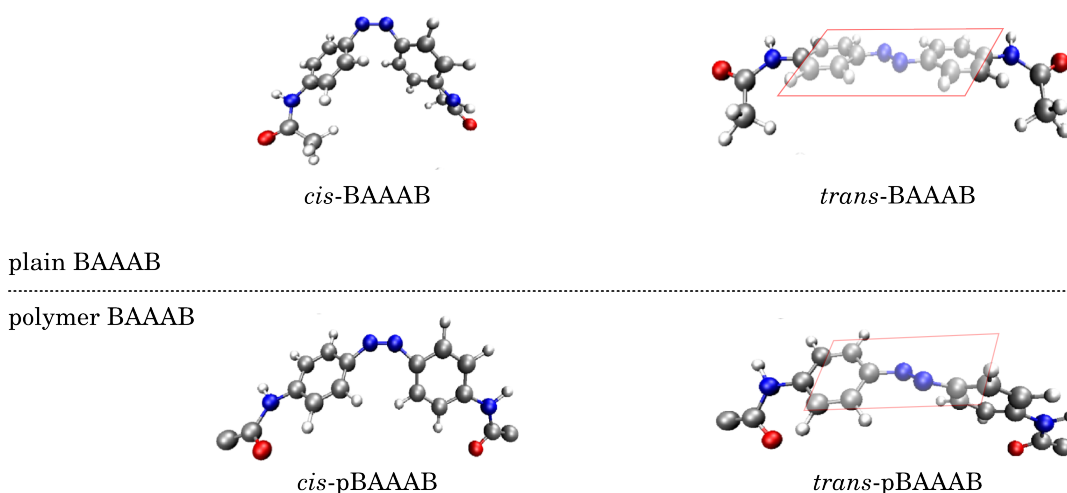


Figure 3.4: FOCI-AM1 and FOCI-AM1/OPLSAA-L optimized ground-state structures of BAAAB and pBAAAB. The molecular plane of the *trans*-isomers is indicated by a red-framed rectangle (see text for details).

With modifications taken from.<sup>65</sup>

polymer. As already mentioned above, the *trans*-BAAAB is slightly contracted inside the polymer. Therefore, one might expect a similar supporting pre-orientational effect as in the case of the *cis*-isomer. In addition, the overall length difference between the isomers inside the polymer is less than 1Å, compared to 4.9Å in gas-phase structures. The reason for the hindering of the isomerization reaction can be found when looking at the overall length changes during the dynamics, as depicted in Fig. 3.5. Obviously, the *trans*→*cis* isomerization reaction features more drastic contractions

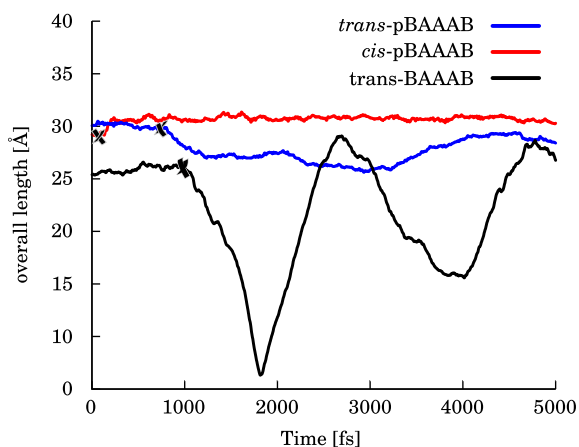


Figure 3.5: Overall length changes of the chromophores BAAAB and pBAAAB during the simulated photodynamics.

With modifications taken from.<sup>65</sup>

during the isomerization dynamics. Please note that these findings link directly to

the considerations presented in Chap. 6, p. 79, where the low quantum yields of AB *trans*→*cis*-isomerization are discussed from the perspective of total displacements during the isomerization dynamics. As a consequence, the surrounding polymer needs to adapt to the contractions of the chromophore, which is a very slow and unfavorable process. It is not surprising that the simulated quantum yield is very low with  $\Phi_{\text{trans-pBAAAB}} = 0.04 (\pm 0.02)$  and the fluorescence quantum yields are high. This can be explained by the trapping of many trajectories at an early stage of the photoisomerization, somewhere on the first excited state, until they finally return to the ground-state surface via radiative decay.

The simulated fluorescence spectra are shown in Fig. 3.6 and qualitatively reflect the experimental findings. The fluorescence spectra of the plain BAAAB chromophores nicely reflect the experimentally observed trends: The spectra of the *cis*-isomer remain almost unchanged, while the spectra of *trans*-BAAAB show a significantly prolonged fluorescence decay. A direct comparison with the experimental data in the lower panel of Fig. 3.6 fits nicely for the plain BAAAB, but shows an overestimated fluorescence lifetime for the chromophore embedded in the polymer. A tempting explanation for the discrepancies observed in the latter case would be that the experimental setup naturally contains a mixture of both isomers. J. Steffen tried to account for this mixing of isomers by summing the spectra of the two isomers with weightings determined by the quantum yields: An equal mixture for the plain BAAAB and almost exclusively *trans*-pBAAAB for the pBAAAB. Unfortunately, the discrepancies between theory and experiment cannot be solely explained by this approach. In the opinion of the author, likely reasons for the observed deviations are found either in the simplified pBAAAB model system or in missing fluorobenzene solvent molecules or in missing quantum decoherence (see also Chap. 2.2, p. 28). The latter one can easily be checked, by simply rerunning<sup>(3)</sup> the trajectories with a very recently obtained MOPAC development version including a new and promising overlap decoherence correction (ODC).<sup>68</sup>

### 3.5 A. Kostevic: BrAB Dynamics following

#### $S_0 \rightarrow S_2$ excitation.

The bachelor thesis of Angelika Kostevic entitled "Dynamik eines Azobenzolderivates auf dem zweiten elektronisch angeregten Zustand"<sup>69</sup> extends the calculations presented in Chap. 4 by simulating a photo-excitation into the  $S_2$  state of brAB.

<sup>(3)</sup>Since the general structure of the input files remains unchanged, this is easily achieved by simply adding three keywords.

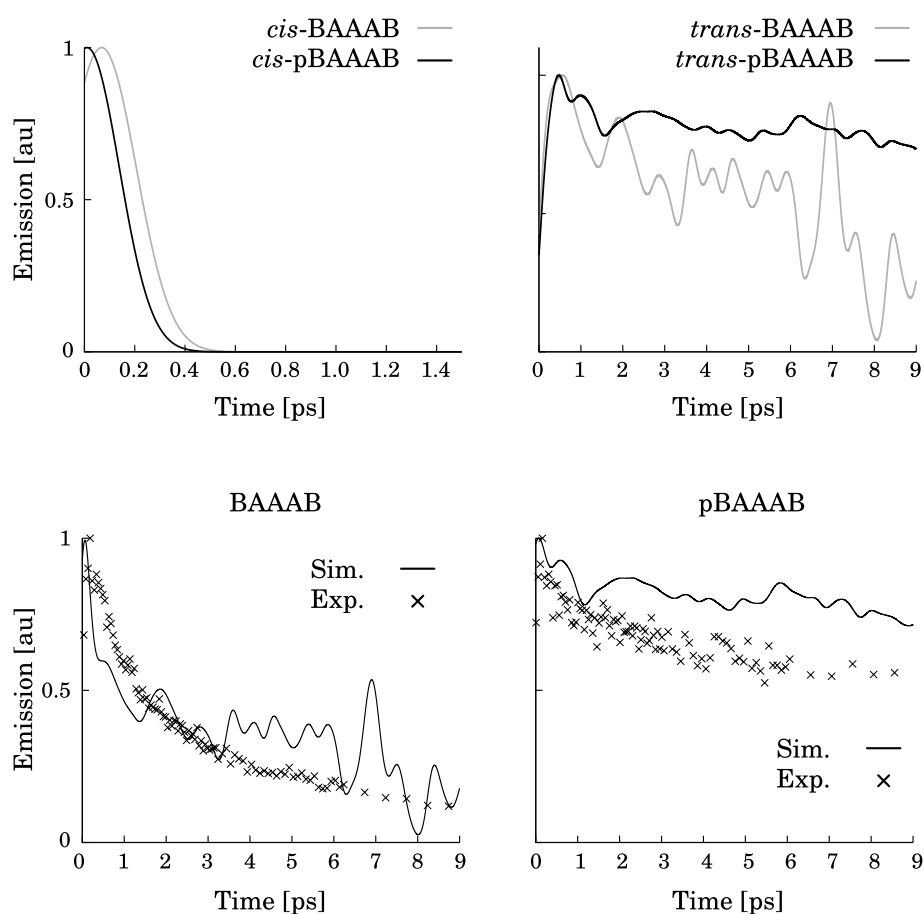


Figure 3.6: Experimental and simulated fluorescence decay of *trans* BAAAB and *trans* pBAAAB (see text for details).

With modifications taken from.<sup>65</sup>

The photodynamics were simulated by running 100, 2.5 ps long, surface-hopping trajectories for both isomers. Starting conditions were sampled from 2.5 ps Brownian ground-state trajectory. As with all surface-hopping calculations presented in this work only the first four singlet states were included in the dynamics.

It was found that the dynamics resulted in significantly increased quantum yields for both isomers with up to 73 % for the dynamics starting from *cis*-isomer and up to 64 % for the reverse reaction. Note that the calculations were gas-phase calculations and the molecule leaves the excited states vibrationally very hot without any cooling opportunity. Instead, the complete energy excess is redistributed internally. As a consequence brAB could cross the ground state barrier between the two isomers and oscillations between *cis*- and *trans*-isomer were observed quite often. The quantum yields listed above mark the fraction of trajectories that reached and stayed in product

formation, e.g. within user-defined boundaries of CNNC and  $\text{CCCC}_{\text{Br}}$  dihedrals, for at least 5 fs and should be interpreted as upper limits. Besides the increased quantum

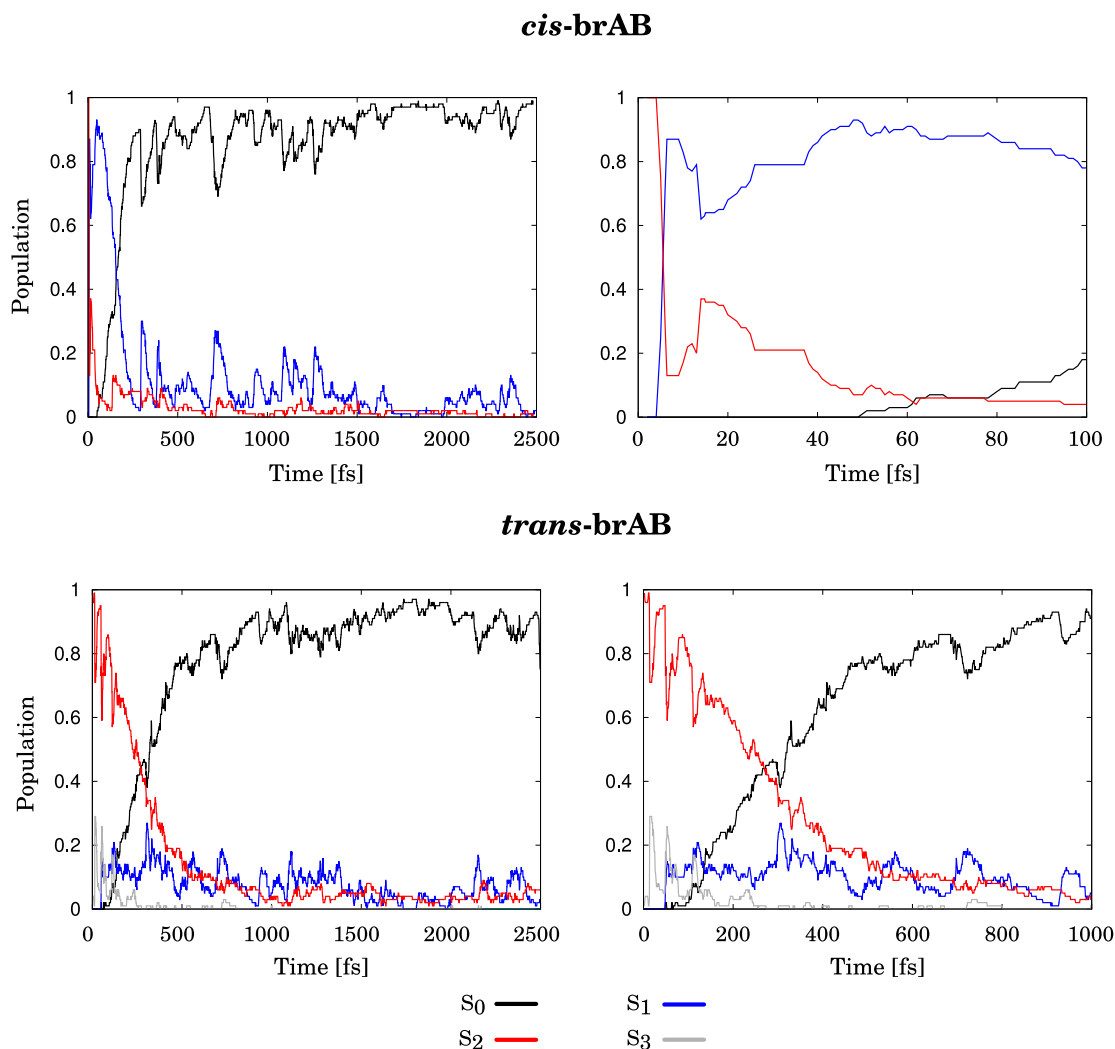


Figure 3.7: Averaged state populations for the *cis*- and the *trans*-isomer following  $S_0 \rightarrow S_2$  excitation. Note the different time scales in the right panels.

Taken from.<sup>69</sup>

yields, the two isomers showed strikingly different reaction mechanisms that manifest themselves already in the average populations of states depicted in Fig. 3.7.

During the *cis*→*trans* reaction the  $S_2$  state is almost instantly depopulated with a rapid decay to less than 20% within the first 15 fs, hinting at steep gradients of the  $S_2$  potential energy surface and/or a strongly coupled region in close vicinity to the FC point. It is not surprising that the internal coordinates are only slightly affected by the short excursion on the  $S_2$  surface, but as discussed in Chap. 7 already a rather subtle modification of starting conditions, a slight opening of the CNNC dihedral angle

and the initial momentum in this case, might be sufficient for a dramatic increase of quantum yields. The subsequent dynamics proceed as expected on the  $S_1$  surface with an average stay of 247 fs before the ground state surface is finally reached. Interestingly the decay to the ground state takes significantly longer than in the case of  $S_0 \rightarrow S_1$  excitation where the trajectories on average returned about four to five times as fast.<sup>(4)</sup> Apart from the rather short excursion to the  $S_2$  surface, the increased quantum yield and the prolonged stay in the first excited state the general mechanism remains unchanged. In particular the dynamics proceed in a straightforward and barrierless manner towards the *trans*-isomer almost exactly as in the case of a  $S_0 \rightarrow S_1$  excitation.

The *trans*→*cis* dynamics are proceeding significantly longer on the  $S_2$  surface as it takes 223 fs until half of the excited-state population has decayed.<sup>(5)</sup> Interestingly a significant amount of the trajectories were found to return directly to the  $S_0$  surface without any visit of the first excited state. This direct return manifests itself in a population transfer between  $S_2$  and  $S_0$  states in Fig. 3.7. The likely reason for this long stay in the excited-state surface seems to be a trapping in a local minimum on the  $S_2$  surface. Once a trajectory manages to reach the  $S_1$  surface, the molecule is promoted rapidly towards the known  $S_1/S_0$  CoIn and experiences the ground state state barrier on its way towards the *cis*-isomer as in the case of  $S_0 \rightarrow S_1$  excitation (see Chap. 4 for details).

In closing it must be noted that the calculations in this bachelor thesis on brAB photodynamics upon  $S_0 \rightarrow S_2$  excitation mark only the very first step towards the simulation of higher excitations. The results must be interpreted with care, as unpublished multireference calculations by J. B. Schönborn<sup>66</sup> which were carried out during the preparation of the bachelor thesis, gave indications that higher excited states of brAB might not be  $\pi \rightarrow \pi^*$  states as they are in the case of naked AB. In this latter eventuality, the semiempirical description of the  $S_2$  and even higher excited states needs to be checked in yet another extensive benchmark.

---

<sup>(4)</sup>Averaged return to ground state surface in gas-phase calculations: 59 fs for reactive and 46 fs for unreactive trajectories (see Chap. 4 for details).

<sup>(5)</sup>Please note that the trajectories that entered the  $S_3$  state ( $\approx 30\%$ , see Fig. 3.7) were excluded from the bachelor thesis due to lack of time and will also be excluded in this summary due to the presumably doubtful quality of the  $S_2$  and  $S_3$  surfaces (see final remarks, p. 53).

### 3.6 R. Höppner: Simulating the photochemistry of bridged azobenzene derivatives

The bachelor thesis of R. Höppner entitled "Simulation der Photochemie verbrückter Azobenzolderivate" aimed at constructing a brAB-like azobenzene derivative that shares the benefits of brAB but does overcome its limitations that manifest themselves in the slow and non-beneficial rearrangement of the ethylenic bridge on the ground-state surface.<sup>67</sup> In direct contrast to the automated design approach presented in Chap. 5, R. Höppners thesis can be considered the logical continuation of our work on brAB photoisomerization mechanisms, namely moving from trying-to-understand towards trying-to-improve.

In order to predict promising candidates Höppner constructed an initial set of eight brAB-like AB derivatives with a variety of different bridging patterns as depicted in Fig. 3.8. From Fig. 3.8 it becomes visible that different bridges were applied as well as different bridging positions with regard to the phenyl rings. The setup was chosen to contain a large diversity in bridge-flexibility with the loose constraint that all structures should in principle be synthesizable.<sup>(6)</sup> Among the structures a preselection of the most promising candidates was carried out by calculating the UV/Vis absorption spectra for both isomers of every molecule accordingly. The calculation of spectra served a double purpose: First, the absorption bands could be checked for undesired overlapping of the  $n \rightarrow \pi^*$  bands and secondly the ground state trajectories needed for the calculations gave first impressions on thermal stability of the isomers. Upon calculation of the spectra most of the initial structures ruled themselves out due to a variety of easily accessible isomeric forms and/or strongly overlapping absorption maxima. Among the promising candidates left, molecule **I** (see Fig. 3.8), was chosen for further treatment with surface-hopping dynamics.

The surface-hopping dynamics of molecule **I** quickly revealed two essential points. The first point is that the increase in bridge-flexibility results in a non-existent ground-state barrier as expected. The other is that once the central ring system is extended, more and more isomeric forms of both *cis*- and *trans*-isomers exist. The latter point is a problem, because the more isomeric forms are involved the more complicated the photochemistry gets. The well-defined *cis*- and *trans*-isomers of brAB and their (more or less) understood reaction paths are then substituted by a manifold of possible reaction paths that tend to branch and the complexity of the problem increases dra-

---

<sup>(6)</sup>...of course seen from the theoreticians point of view.

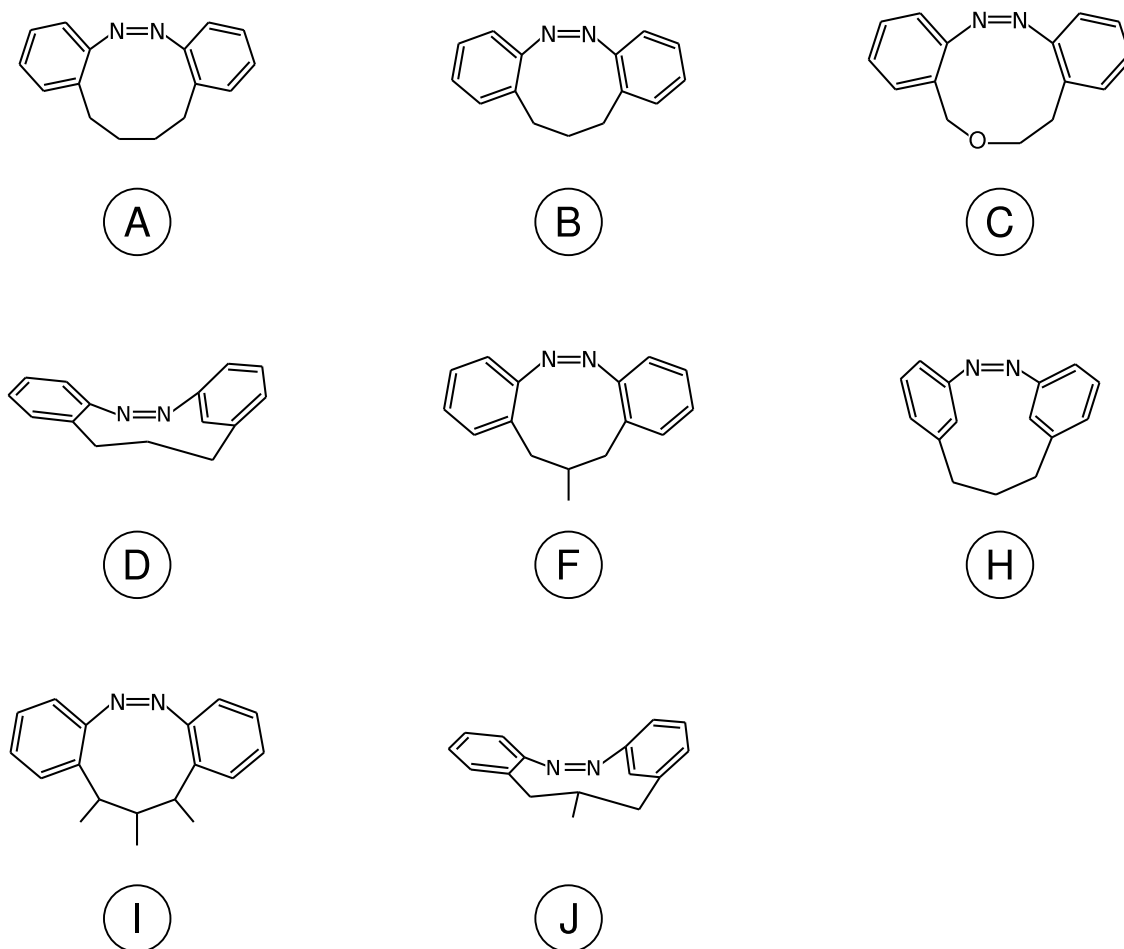


Figure 3.8: Initial set of brAB-like AB derivatives as used in Höppners bachelor thesis (see text for details).

matically. It should be noted that the existence of more isomeric forms of *cis*- and/or *trans*-isomers does not necessarily result in complicated photodynamics as in the case of molecule I. This can be seen when looking at the parent compound brAB that also possesses two isomeric forms of the *trans*-isomer, but only one form is accessible via ( $S_0 \rightarrow S_1$ ) photo-excitation of the *cis*-isomer. Therefore, and because the *cis*-isomer is the thermodynamic stable one, the other form becomes completely insignificant. Fig. 3.9 visualizes the above as it shows the five isomeric forms of molecule I that, according to Höppners simulation, are accessible at room temperature on ground-state surface.

When simulating the photodynamics of I every structure shown in Fig. 3.9 has to serve as a starting point of enough(!) surface-hopping trajectories to capture the essential features of the dynamics following the excitation. In diligent work, Höppner analyzed all reaction paths running 100, 2 ps long, surface hopping trajectories and

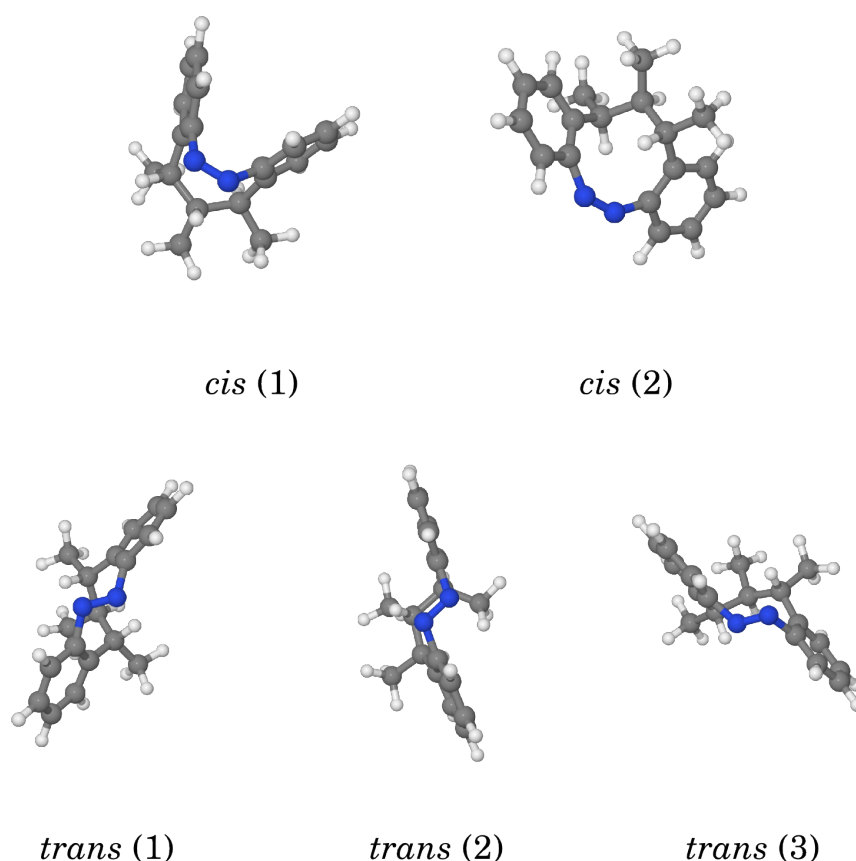


Figure 3.9: Isomeric forms of molecule **I** (see Fig. 3.8, p. 55, bottom left) as optimized by Höppner (see text for details).

Taken from.<sup>67</sup>

a 10 ps ground state trajectory for every isomer shown in Fig. 3.9. The resulting mechanisms are very complex and can be found in Höppners thesis. They will not be summarized here. However, an excerpt is shown in Fig. 3.10 where the reaction pathways starting from only one isomer are depicted. Since the complex and branched dynamics of molecule **I** disqualified it as potential molecular switch, Höppner proposed one more AB derivative termed molecule **K** as depicted in Fig. 3.11. As molecule **I** did show too much flexibility with regard to the bridge, a central oxygen was introduced with the aim of reducing the bridge-flexibility. First geometry optimizations of molecule **K** yielded only one *cis*-isomer and two *trans*-isomers, as in the case of brAB, apart from the finding that both isomeric *trans* forms could interconvert during ground state dynamics at 300 K. The ability to interconvert between the two isomeric *trans*-forms suggests more flexibility than in the case of the parent compound brAB. Nonetheless the two *trans*-forms could be non-beneficial depending on their according absorption maxima, but luckily the simulated UV/Vis absorption spectra in Fig. 3.11 show clearly separated maxima for *cis*- and *trans*-isomers, since the two



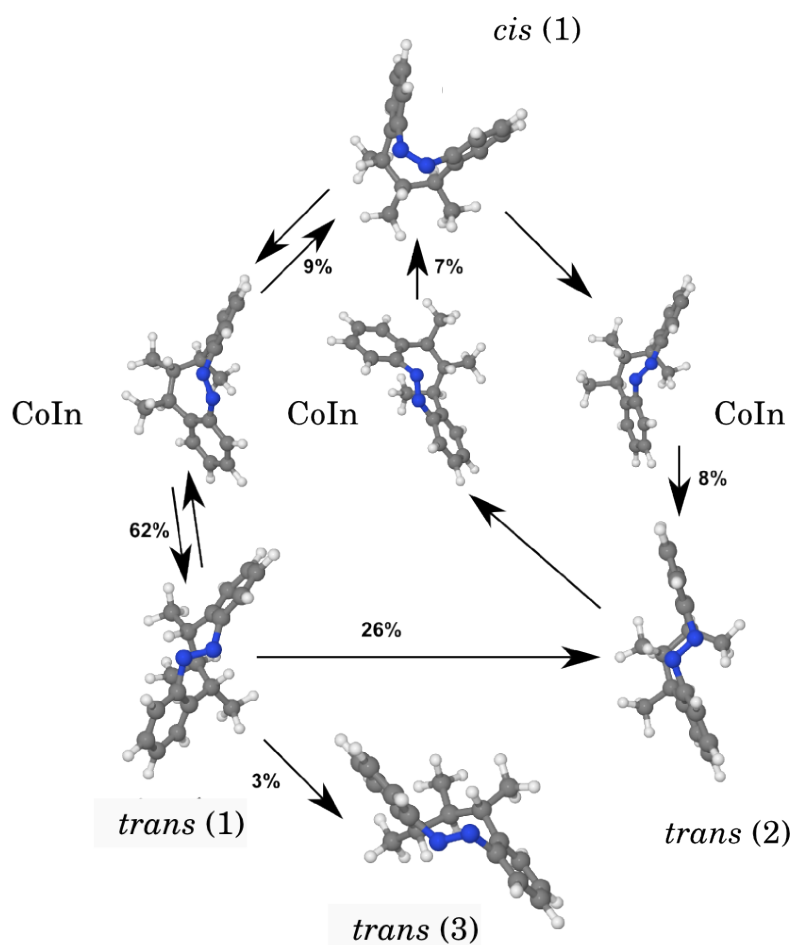


Figure 3.10: Reaction pathways starting with  $S_0 \rightarrow S_1$  excitation of the *cis* (1) isomer of molecule I (see Fig. 3.9, p. 56, top left) according to Höppner.

Taken from.<sup>67</sup>

*trans*-isomers almost completely overlap. Whilst the two interconvertible *trans*-forms

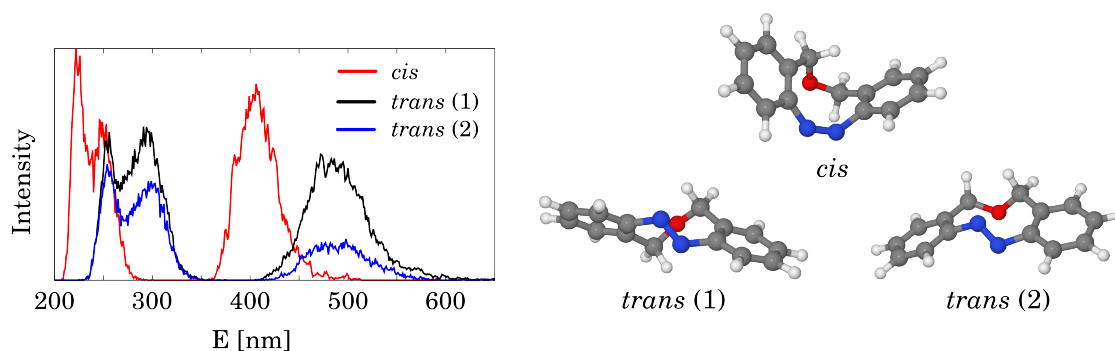


Figure 3.11: Simulated UV/Vis absorption spectra of molecule K as proposed by Höppner. The FOCI-AM1 optimized ground state structures are shown alongside on the right.

Taken from.<sup>67</sup>

are clearly not beneficial in applications where the molecular switch needs to have a

defined conformation, molecule **K** might still be of use in optical devices. It is of rather simple structure and presumably exhibits ultrafast switching combined with large quantum yields, probably larger than those of the parent compound brAB. In addition, the synthesis of molecule **K** is likely to be simpler than that of the parent compound brAB. In fact the synthesis is currently attempted in the Herges and Staubitz groups.

# GAS PHASE PHOTODYNAMICS OF A BRIDGED AZOBENZENE DERIVATIVE

## 4.1 Scope of the project

The scope of the following project, which started as the diploma thesis of the author, was the proposal of a reaction mechanism for a novel bridged azobenzene derivative (brAB).

Following the discovery of enhanced photoswitching capabilities of brAB by Siewertsen and coworkers during the course of the collaborative research project SFB 677, this presents the first comprehensive theoretical dynamics study of brAB. Comprehensive refers to a preceding communication by Marx *et al*, namely the first purely theoretical study on brAB published that employed only 30 surface-hopping trajectories<sup>(1)</sup> at the restricted open-shell Kohn-Sham level, all of them starting from the *cis*-isomer and completely neglecting the dynamics starting from the *trans*-isomer.

The initial motivation for a direct trajectory surface-hopping treatment of brAB was given by experimental data showing ultrafast photodynamics and distinct transient absorption spectra for the *trans-cis*- and *cis-trans*-isomerization as well as

---

<sup>(1)</sup>Brief historical note: The Diploma thesis of the author actually pre-dated the publication by Marx and coworkers significantly. In fact Marx and coworkers became aware of brAB via our work at the symposium of theoretical chemistry in Neuss (8.-12.9.2009). It was only due to the limited set of trajectories and the exclusion of the *trans*-dynamics that their publication could pre-date our publication presented below.

preceding static *ab-initio* multireference calculations by J. B. Schönborn. Summing up the above, brAB offered unrevealed mechanistic details in an ultrafast photochemical process, which made it an ideal candidate for a treatment with direct surface-hopping dynamics.

## 4.2 Own Contribution

All FOCI-AM1 calculations, including the complete dynamics, were carried out by the first author. He also wrote the software used for analysis of the trajectories (including all spectra, hopping maps, quantum yields...) and proposed the reaction mechanisms. These calculations were already subject of the authors diploma thesis, but almost everything of what was presented there was recalculated as the set of trajectories was extended to the total amount of 500 trajectories (250 trajectories for each isomer).

## 4.3 Publication

**Authors** *Niss Ole Carstensen, Jan Boyke Schönborn,  
Jan Sielk and Bernd Hartke*

**Title** Unusual photochemical dynamics  
of a bridged azobenzene derivative

**Submitted** 23 March 2010

**Accepted** 26 July 2010

**Publication Data** J. Chem. Phys., **133**, 2010, 124305.  
DOI: 10.1063/1.3479397

### Abstract

In a large-scale simulation study of ultrafast photochemical dynamics for an azobenzene compound with an additional ethylenic bridge we have found unexpected features: while the dynamics starting from the Z isomer follow a barrierless path with steep gradients, the dynamics starting from the E isomer proceed through a different conical intersection surrounded by a rather flat potential energy landscape and then encounter a sizeable barrier in the electronic ground state that markedly influences the reaction behavior. Direct comparisons with experimental static UV spectra, quantum yields, and transient absorption spectra show good agreement and reveal signatures of this unusual behavior.

## 4.4 Additional Information

The above publication on FOCI-AM1 gas-phase dynamics of brAB definitely marks the foundation of the following works on brAB and its derivatives in this thesis. This section is organized as follows: First the results from the benchmarking procedure against multireference *ab-initio* data provided by J. B. Schönborn are summarized, before the reception of the publication in follow-up publications is discussed. The focus of the latter part lies on the reaction mechanism of the *trans*-isomer and the ground-state minimum structure involved in it. The section concludes with a discussion of the question whether or not the brAB photoisomerization involves two conical intersections.

At the center of any theoretical description of photodynamics lies the quality of the potential energy surfaces. Due to the very nature of photochemistry, several surfaces are involved and both the shape of the single surfaces and their proportions relative to one another are of importance for a correct description of experimental findings. Additional complications arise if the method of choice is a semiempirical method. Speaking honestly, many theoreticians still consider semiempirical methods as being hardly more reliable than simple force fields. As a consequence every study not including the label "*ab-initio*" in the title is in the need of a thorough and critical benchmarking.

Unfortunately, benchmarking the quality of excited-state surfaces still is very challenging, although great research effort has been spent on this field and a large variety of methods could in principle be used.<sup>70</sup> In the case of brAB, where ultrafast dynamics were reported by the experiment, the reasonable (and computationally most expensive) choice lies in the use of multiconfigurational and multireference *ab-initio* calculations, as the Hartree-Fock reference wave function is simply not capable of describing conical intersections or strongly distorted molecular geometries (as pointed out in Chap. 2).

Fig. 4.1, taken from the electronic supplementary information of the above publication, is intended to visualize the term "qualitatively correct" used throughout this thesis for the quality of the potential energy surfaces. The scan along the CNNC coordinate, presented in the upper left of Fig. 4.1, clearly shows discrepancies between the reference data and the FOCI-AM1 data. Apart from the obvious differences, a very important feature, the relative shape of the surfaces, emerges on second glance. The relative shape seems to be roughly reproduced, which would explain the good perfor-

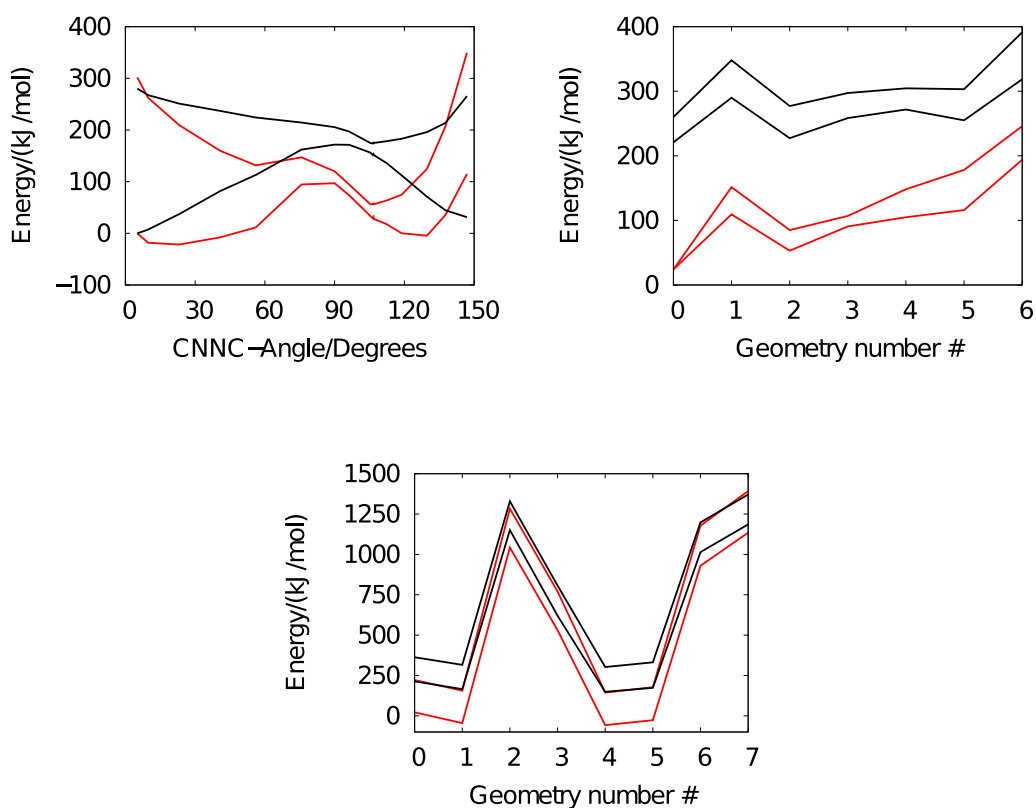


Figure 4.1: Energies for various brAB geometries calculated at the FOCI-AM1 (black lines) and CASPT2/app-TZ (red lines) levels of theory.

formance of the FOCI-AM1 dynamics in direct comparison with experimental data (see also Chap. 7, p. 87). Due to the benchmark procedure, single-point calculations on a set of benchmark structures, additional complications may arise. Consider a situation where the surfaces are exactly alike but the structures corresponding to points on the surface differ by a few degrees. The resulting comparison of single-point calculations with the same structures would indicate a bad correlation, even though the surfaces are in fact only slightly shifted against each other. This is an inherent problem in every benchmark procedure employing single-point calculations. Nonetheless, this should be kept in mind when looking at the graphs in Fig. 4.1.

Another point worth stressing is already discussed in the electronic supplementary information. The *ab-initio* calculations carried out by J. B. Schönborn did employ CASPT2(14,12)/ap-TZ calculations as the highest level reference not because they mark the final answer, but because this is the limit of what could be afforded in terms of computational costs. Putting it bluntly, these reference data themselves are definitely not fully correct. Since there will probably never be a final answer to the question of what the excited state surfaces of brAB actually do look like, we also

took into account the most direct information available, that is the experimental absorption time profiles, and found that the essential trends were well reproduced, especially in the QM/MM dynamics presented in Chap.7. Further support for the application of FOCI-AM1 semiempirics comes from the reproduction of the reaction mechanism following  $S_0 \rightarrow S_1$  excitation of the *trans*-isomer by other theoretical studies, employing other theoretical models (see below for the discussion).

In conclusion, it was not until the exhaustive benchmark and the direct comparison to various experimental data revealed that the reparametrized FOCI-AM1 semiempirics are in fact capable of capturing the essential features of brAB photodynamics that follow up projects like automatized design of photoswitchable molecules as described in Chap. 2, the FOCI-AM1/OPLSAA QM/MM dynamics in Chap.7 and 6 and most of the bachelor topics reported in Chap. 3 were at all possible. In a nutshell, all of the above established the reparametrized FOCI-AM1 semiempirics as the method of choice for (single chromophore) azobenzene (derivatives) in the Hartke group, serving as a quick and solid approach for excited-state calculations on azobenzene (derivatives). It was even used as a reference itself for reparametrization of a reactive force field.<sup>71</sup>

The second central point refers to the first formulation of the brAB mechanism following  $S_0 \rightarrow S_1$  ( $n \rightarrow \pi^*$ ) excitation. Of course this is directly coupled to the first point as the results distilled from the trajectories would be meaningless without the *ab-initio* benchmarks. It should be pointed out that the above publication contains the first formulation of the *trans-cis*-photoisomerization mechanism that by now has been supported by several other theoretical studies on brAB.<sup>72-76</sup> The first theoretical communication on brAB, published by Marx *et al.*,<sup>72</sup> did completely exclude this central part of brAB photochemistry, since it only deals with the opposite isomerization reaction.

It is worth noticing that although presenting trajectory data that support our proposed reaction mechanism, most of the follow-up publications by other authors did not recognize the intermediate minimum structure as the one described in our publication. Fig. 4.2 shows the characteristic ground-state minimum structure with its characteristic coordinates. As the configuration of the central ring system is described accurately with the coordinates shown in Fig. 4.2 it seems to be very unlikely that if the coordinates take on these values the molecular geometry differs significantly from the one depicted.



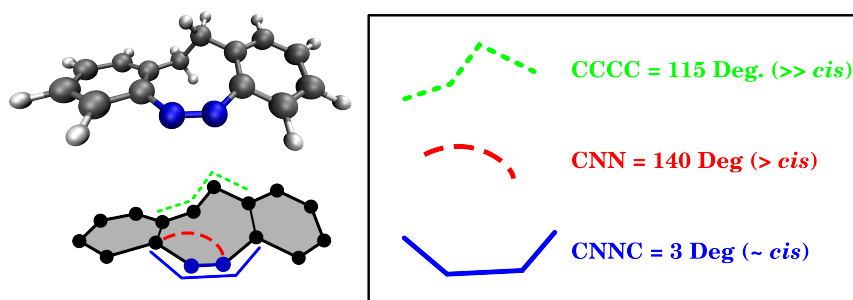


Figure 4.2: Ground-state minimum structure reached during *trans-cis*-photoisomerization with the characteristic degrees of freedom. The shown structure results from a FOCI-AM1 geometry optimization (confirmed by frequency calculation). Given in parentheses is whether these coordinate values are about equal ( $\approx$ ), slightly bigger ( $>$ ) or substantially bigger ( $>>$ ) than the corresponding ones of the *cis*-isomer.

So far all dynamics simulations we are aware of show these signatures in the trajectory data. For example the trajectory data published in references 73-76 clearly confirms this finding. When compared with Fig. 4.2 these works do reveal that the minimum structure is reached, though somehow not recognized by any of the authors. The work of Liu and coworkers<sup>77</sup> requires special interest since the minimum structure is said to be "not supported by the present electronic structure calculations". Their attempted geometry optimizations using B3LYP/6-31G\*, MP2/6-31G\* and CASPT2(14,12)/6-31G\* converged to the *cis*-isomer.

In fact, our own geometry optimizations using B3LYP/SVP and B3LYP/cc-pVTZ<sup>78-83</sup> using the program suite TURBOMOLE<sup>84</sup> support Liu's findings. A B3LYP/cc-pVTZ optimization yielded a transition state with an imaginary frequency of 39.59 cm<sup>-1</sup>. Note that, at first sight, the results from the dynamics and the stationary quantum chemical calculations seem to contradict: On the one hand, the minimum structure is supported only by our reparametrized semiempirical calculations, leading to the conclusion that the ground-state minimum structure is unlikely to exist. On the other hand, the footprints in the trajectory data clearly show the importance of the intermediate. In the author's opinion, the question of whether or not the intermediate structure is a "true" minimum is less important than its distinct role in the dynamics. Even when accepting the assumption that there exists a barrierless reaction pathway between the conical intersection and the *cis*-isomer, it is obviously not taken. Such behaviour is often found in multi-dimensional dynamics, and it is resolved by statistics, because the required distribution of kinetic energy over the right degrees of freedom is simply a matter of probability and time.

The final point that needs additional discussion is the question of whether or not brAB photodynamics proceed via different local minima along the  $S_1/S_0$  intersection seam when starting from the *cis*- or *trans*-isomer. Finding a definitive answer to this question remains hard, despite the growing amount of theoretical work published on brAB. When presenting an overview of what is published on this particular question, we shall start off by summing up the essential findings by our group: The two minimum structures do not show much structural difference, except in the dihedral angle of the ethylenic bridge and most significantly in the NNCC-dihedral angles (that is, in the orientation of the phenyl rings).

The publication by Böckmann *et al*<sup>73</sup> states that optimized  $S_1$  local minima, as published by Siewertsen *et al*,<sup>85</sup> were found to be higher in energy than their optimized structures obtained by ROKS and CASSCF(10,8) calculations. Additionally, a different ordering of canonical MOs was found for structures within a range from 90-110° of the CNNC dihedral (e.g. the intersection region), which when taken into account seem to converge to a single minimum. The authors reference the work published by Liu *et al*, which also reports only one conical intersection. Apart from these remarks, Böckmann *et al* exclude the possibility of two local minima within the intersection seam from their further discussions. Fig. 4.3 shows the structures Böckmann

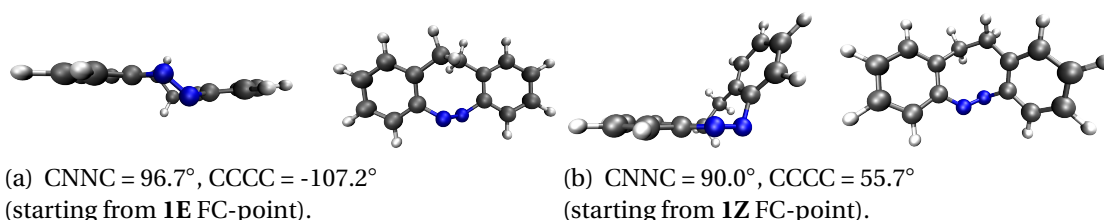


Figure 4.3: Excited state structures from Siewertsen and coworkers. Starting from the FC-points of the two isomers a relaxed scan along the CNNC-dihedral angle was carried out using CASSCF(14,12) with a mixed aug-cc-pVTZ, cc-pVDZ, STO-3G basis set.<sup>85</sup>

and coworkers refer to. The structures are optimized local minima taken from the electronic supplementary information of Siewertsen and coworkers.<sup>85</sup> Interestingly, the authors stress the fact that the published data does not include a valid conical intersection structure, but a series of separately (!) optimized structures for several fixed CNNC dihedral angle values. Although the data clearly suggests an intersection region, no conical intersection optimization was presented in this publication. Instead the authors stress the fact that their one-dimensional scan is supposed to give a first impression on the characteristics of the first excited state and is not to be confused with a fully optimized minimum energy path. Also, the structures around CNNC $\approx$ 96°

(the ones shown in Fig. 4.3 that show near degenerate  $S_0/S_1$  energies) are significantly differing regarding the ethylenic bridge and the orientation of the phenyl rings, which could support the existence of two minima along the intersection seam. On the other hand, the ethylenic bridge is said to be rather flexible thus not ruling out the possibility of only one minimum.

Within the study of Liu and coworkers,<sup>77</sup> only one distinct conical intersection structure was found and optimized by a state-averaged CAS(10,8)/6-31G\* calculation. The study includes dynamics for both isomerization processes and a scan of the potential energy surfaces, but also a feature inherent to many theoretical dynamics studies on brAB: One of the essential coordinates, i.e. the dihedral angle of the ethylenic bridge, is not shown for the trajectories or potential energy surfaces. As already discussed above, this particular internal coordinate most clearly distinguishes the two intersection seam structures in our work. Therefore, a comparison of the dynamics with regard to the conical intersections becomes difficult. However, the authors report the two-step isomerization mechanism starting from the *trans*-isomer. At least in our study and the studies including the CCCC-angle, this mechanism features a delayed adjustment of the ethylenic bridge. In the author's opinion, a thorough discussion of this mechanistic question, based on the change in the ethylenic bridge, has not yet been presented.



# DESIGN OF OPTIMALLY SWITCHABLE MOLECULES BY GENETIC ALGORITHMS

## 5.1 Scope of the project

The project presented in this chapter comes from the popular discipline of molecular design. Its novelty arises from the fact that two rather unrelated subcategories of theoretical chemistry, namely global optimization and photochemistry, are combined in an unique automated design approach. Both global optimization techniques<sup>86,87</sup> and theoretical photochemistry<sup>88,89</sup> have individually been used for molecular design, but since both fields are computationally very expensive a combined approach seemed beyond the bounds of the feasible. However, the deployment of semiempirical floating-occupation configuration interaction methods (as used throughout this thesis) does allow for a quick and reasonable accurate estimation of vertical excitation energies and facilitates the combination with a global optimization technique in this pioneering, proof-of-principle project.

The property subject to the global optimization procedure is the tuning of vertical excitation energies of brAB up to a user-defined target value. In order to suggest practical relevance the wavelengths of cheap commercial laser pointers were chosen as target values for the optimization procedure. Tuning of vertical excitation energies was realized by different substituent patterns that were automatically constructed, optimized and evaluated by the high-performance global optimization program suite

OGOLEM developed by J.M.Dieterich in the Hartke group.<sup>90</sup>

## 5.2 Own Contribution

Apart from coming up with the original idea, all FOCI semiempirical calculations including the surface-hopping dynamics for the post-processing, the calculation of UV/Vis absorption spectra and the fitting procedure used for a quick estimate of the band shapes were carried out by the first author. Both the implementation of the program part `ogolem.switches` and the actual global optimization were carried out by the second author, J. M. Dieterich as part of his PhD thesis work.

## 5.3 Publication

<b>Authors</b>	<i>Niss Ole Carstensen, Johannes M. Dieterich and Bernd Hartke</i>
<b>Title</b>	Design of optimally switchable molecules by genetic algorithms
<b>Submitted</b>	02 July 2010
<b>Accepted</b>	10 November 2010
<b>Publication data</b>	Phys. Chem. Chem. Phys., 2011, <b>13</b> , 2903. DOI: 10.1039/C0CP01065K

### Abstract

We demonstrate the possibility to design molecules for specific tasks, using a fully automatic global optimization setup employing genetic algorithms. As an example, we tune the two excitation wavelengths of a molecular switch backbone to arbitrarily pre-set values, by an automatic optimization of the substituent pattern.

## 5.4 Additional information

The section is organized as follows: First some additional information on the proposed molecular switch, 4-hydroxy-2,8,9,10-tetranitro-11,12-dihydrodibenzo[*c,g*][1,2]diazocine-1,3,7-tricarbaldehyde (tn-brAB, upper left in Fig. 5.1) is presented before a perspective on push-pull substitution patterns in combination with brAB and the overall design approach is given.

Beforehand, one important thing to keep in mind is the excessive substitution of all optimized molecules. As already pointed out in the publication this substitution patterns cause a serious infringement on the electronic structure of brAB. Although the FOCI-PM3 method does not rely on the AB specific parameterset, like FOCI-AM1, it still utilizes the same active space consisting of 94 selected determinants that are considered important in AB photochemistry. Therefore all of the results presented are in desperate need of a thorough *ab-initio* benchmark. As already mentioned in the publication itself, an *ab-initio* benchmark was discarded due to the study's proof-of-principle character.

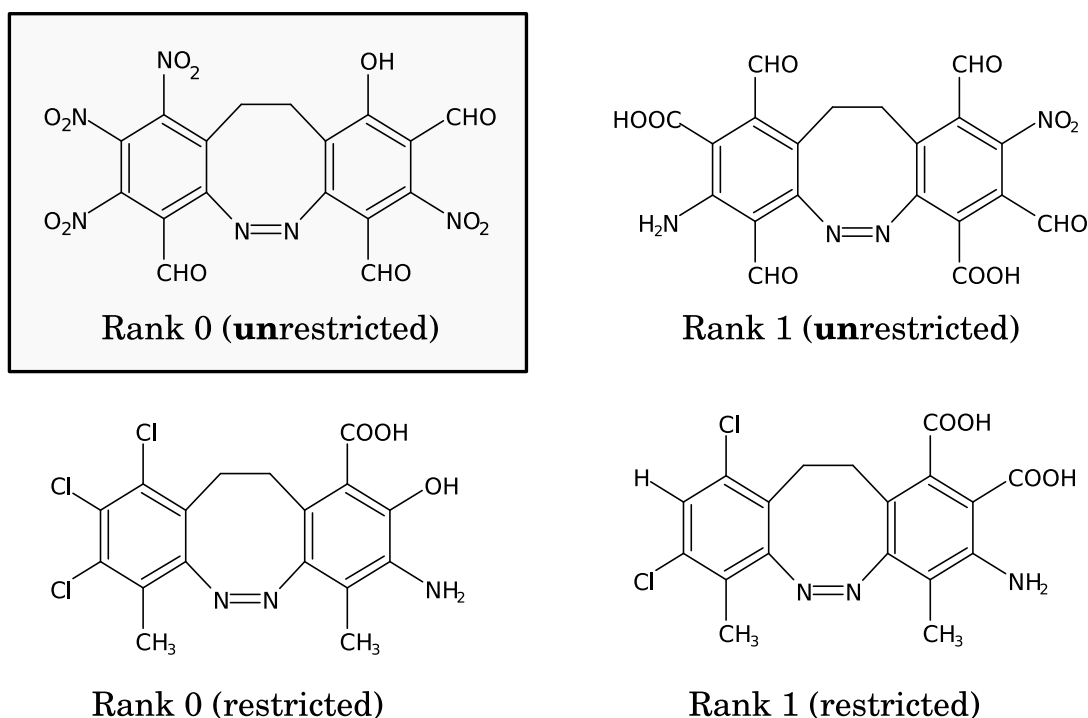


Figure 5.1: Overview of the optimized structures proposed in the above publication and shown in Fig. 4 and Fig. 5 therein. The molecule tn-brAB is highlighted and shown in the upper left panel (see text for details).

One of the central approximations presented in the above work was the approximation



of the UV/Vis spectra by a sum of Gaussian functions. The linear combination of Gaussians can adjust via the vertical excitation energies and squared transition dipole moments taken from a calculation of vertical excitation energies. It should be noted that this approach was chosen as it employs all information about the absorption bands that can be extracted from a single-point calculation. A more advanced calculation of the band shape increases the computational effort dramatically, because - depending on the method of choice - either a long ground-state trajectory or knowledge of the ground- and excited-state vibrational wave functions are required (see Chap. 2.3, p. 34).

However, the validity of this approximation was not elaborated further in the publication. For this purpose, Fig. 5.2 shows a direct comparison of the UV/Vis absorption spectrum of tn-brAB computed from a long ground-state trajectory and the spectrum constructed from a linear combination of Gaussian functions. There is surprisingly good agreement between the spectra, which shows that at least in the case of tn-brAB the approximation is in fact a reasonable one. All peak centers are at the correct positions and of adequate width, although the peaks that result from higher excitations than  $S_0 \rightarrow S_1$  are overestimated in width. Nonetheless the  $n \rightarrow \pi^*$  bands, our primary objective, show a good agreement in both shape and position. A possible explanation for this finding is the rather limited flexibility of the molecular framework of brAB, which efficiently prevents large conformational changes during ground-state dynamics. In any event, the approach seems to be a sufficiently reliable for a quick estimate of the band shapes in an automatized design approach.

The surface-hopping dynamics of tn-brAB showed the same characteristics as for the parent compound brAB. In particular, the distinctive dynamics following  $S_0 \rightarrow S_1$  excitation of the *trans*-isomer (see Chap. 4, p. 59) are also found in the tn-brAB dynamics, despite the drastic modification of the electronic character. Nonetheless, an interesting observation was made when the energetics of the two isomers were compared with the ground-state energy barrier<sup>(1)</sup> as depicted in Fig. 5.3. The energy difference between *cis*- and *trans*-isomer remains almost unchanged with respect to the parent compound brAB, while the opposite is true for the height of the barrier, which has fallen below one quarter of the original height. At first sight this might seem unexpected, but in fact similar effects were found in theoretical works on push-pull substituted ABs.<sup>91,92</sup> In particular, Roitberg and coworkers performed B3LYP/6-31G\* and TD-B3LYP/6-31G\* calculations on naked AB and a set of four push-pull substi-

---

<sup>(1)</sup>The energies result from FOCI-PM3 optimized transition states.

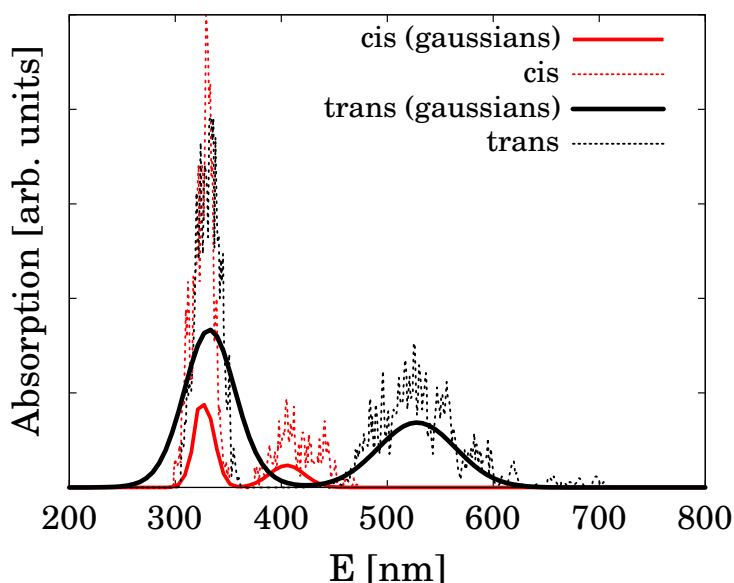


Figure 5.2: Comparison of UV/Vis absorption spectra of tn-brAB calculated from a long ground-state trajectory (dotted lines) and approximated by a linear combination of Gaussian functions (see text for details).

tuted ABs and claimed a pronounced substituent effect on the rotational ground-state barrier.<sup>91</sup> The calculations showed that electron-withdrawing substituents lowered the barrier, while electron-donating substituents raised the barrier compared to naked AB. However, the energy difference of *trans*- and *cis*-isomers were not, or only very little, affected by the substituents, as in the case of tn-brAB. Even though the tn-brAB barrier is lowered by 121 kJ/mol, compared to 64 kJ/mol in the case of NO<sub>2</sub>-NH<sub>2</sub>-AB, this difference can be explained by the incorporation of the four extremely electron withdrawing NO<sub>2</sub> substituents in tn-brAB that probably increase the effect. When discussing energetics, it should be pointed out that TD-B3LYP energies should not be trusted quantitatively in close vicinity to conical intersections formed by a twisting of double bonds.<sup>93</sup> Estimated from the intersection regions of bare AB, the rotational barriers reported by Roitberg *et al.* are located very close to the S<sub>0</sub>/S<sub>1</sub> conical intersection seam. Therefore the energetics should be interpreted in a more qualitative manner in the absence of supporting *ab-initio* multireference data. Apart from the exact numbers in energetics, it appears to the author that the high quantum yields reported in the above publication can, at least in part, nicely be explained by the effect of a lowered ground-state barrier. In fact this was not the objective of this project but the objective of R. Höppner's bachelor thesis presented in Chap. 3.6 on p. 54.

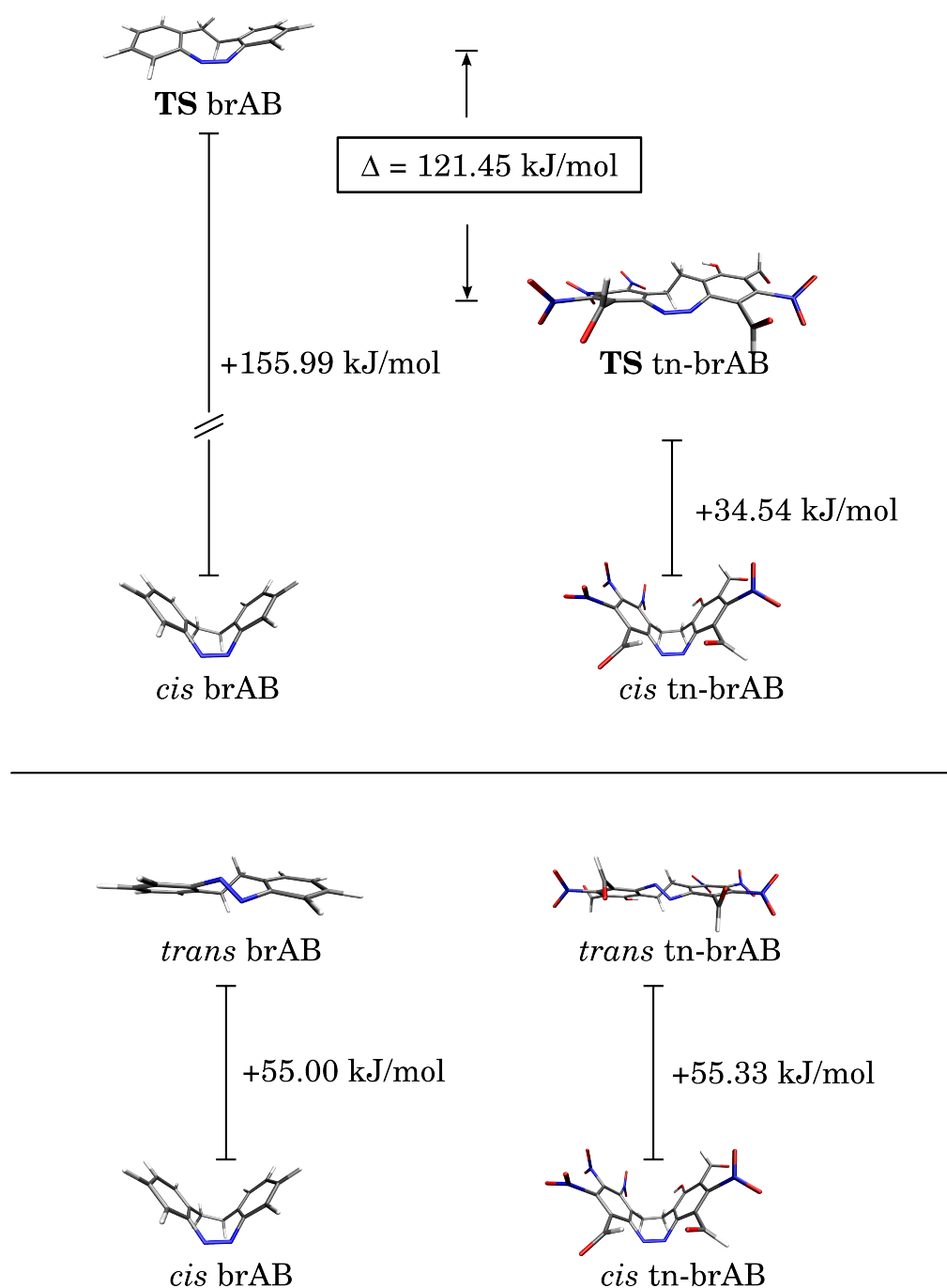


Figure 5.3: FOCI-PM3 optimized ground-state structures of both isomeric forms, *cis* and *trans*, of brAB and tn-brAB (*bottom*) and optimized transition states (*top*). All energies are given relative to the according *cis*-isomers (see text for details).

As an estimate of the changes in the electronic character of tn-brAB with regard to the parent compound, the computed dipole moments of brAB and tn-brAB are shown in Fig. 5.4. For comparison the length of the dipole moment vector of *cis*-NO<sub>2</sub>-NH<sub>2</sub>-AB, i.e. the archetypal push-pull substitution pattern, was computed with B3LYP/6-31G\* and found to be 7.53 Debye by Roitberg *et al.*,<sup>91</sup> which is almost alike

to the dipole vectors computed for tn-brAB. Of course the push-pull character of an AB derivative does not manifest solely in the electric dipole vector, but a quantum chemical investigation on mesomeric forms would exceed the scope of this section. Additionally, tn-brAB can be expected to be an extremely fragile compound that should better remain a theoretical model for the sake of everybody's safety.

Still, the published data for push-pull ABs shows notable parallels with tn-brAB, suggesting that a more thorough study on less dangerous push-pull brABs (e.g. NO<sub>2</sub>-NH<sub>2</sub>-brAB) would be very interesting. Presumably, the ground-state barrier can be lowered and the quantum yields for both switching directions can be increased. Moreover, pronounced solvent effects can be expected, as in the case of push-pull AB,<sup>94</sup> where rotational barriers are effectively lowered by usage of polar solvents due to a stabilization of strongly polar transition state geometries. This effect is likely to exist in push-pull brABs as well, given that tn-brAB possesses a similar overall dipole moment (see Fig. 5.4). Last but not least, the main reason for push-pull ABs not being more popular molecular switches, the serious lack of product lifetime, caused by lowered inversion(!) barriers on ground-state surface, is very likely eliminated with push-pull brABs, because of the ethylenic bridge. In a nutshell: In the opinion of the author, push-pull brABs offer the experimentalist a vast amount of adjusting screws for creating tailor-made molecular switches.

The presented automated design approach succeeded in finding an optimal molecular structure, of course within the limits of the FOCI-PM3 methods and of the authors knowledge about synthesis-related constraints. While the resulting molecular switch might not be a candidate for a real-life application, it still points towards push-pull substitution patterns that are of potential interest. In general, unexpected structural motifs are an inherent feature of non-deterministic global optimization techniques. As demonstrated above, automated design approaches do not replace the human molecular designer but can nicely be used as a source for additional inspiration. The actual criteria that can be incorporated into the design approach are numerous. To name but a few possible candidates: Synthesis related constraints, size/shape constraints, the wettability, orientation and amount of the electric dipole or a transport of kinetic energy from a chromophore to another (functional) part of a molecule could be included and optimized fairly easy. If the reader is willing to think in bigger dimensions, he could also consider computer-aided design (CAD) software for molecular machines, not in the sense of running quantum chemical program suites "by hand", but in the sense CAD software is used by an engineer. Such a program could offer a

variety of molecular hinges, motors, pumps or in general functional building units that are presented in an abstract manner and automatically combined and optimized once the desired overall function is formulated by the "chemical engineer". A continuation of the above publication can already be found in the Hartke group, namely in the work of S. Frick, who is currently developing a multi-purpose global optimization molecular design framework.

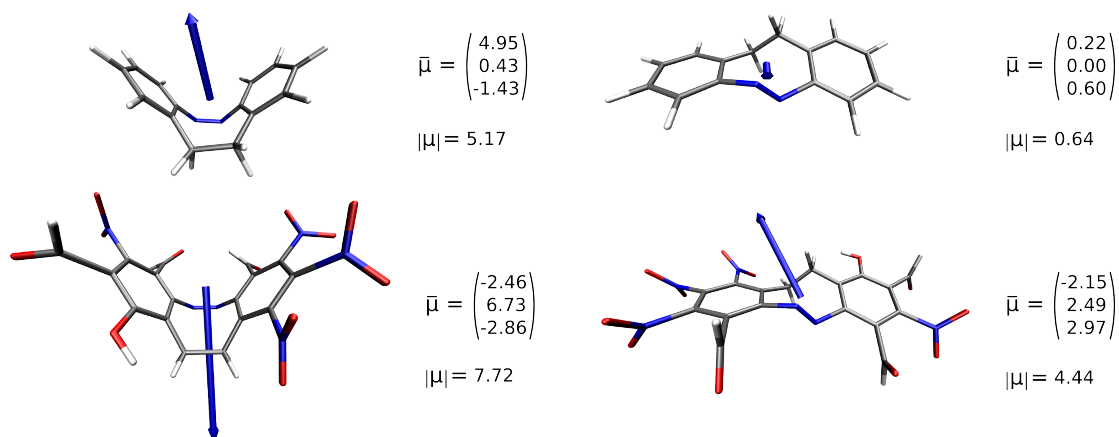


Figure 5.4: FOCI-PM3 optimized isomeric forms of brAB and tn-brAB. The arrows visualize the electric dipole vectors listed alongside and are centered at the center of mass. All units are in Debye.



# SIMULATING A COMPLETE MOLECULAR MACHINE IN ACTION

## 6.1 Scope of the project

The following project is the first attempt to directly simulate explicit photodynamics of a complete molecular machine driven by an AB motor. It marks not only a continuation of a bachelor project started in the Hartke Group,<sup>95</sup> but employs also a platform approach developed and experimentally applied in sub-project B09 of the SFB 677.<sup>58</sup>

From the technical side, initial motivation for the current molecular setup arose from published experimental data by the Herges Group, namely static UV/Vis absorption spectra of an AB mounted on the platform that could be used for a comparison with the simulated spectra, since an *ab-initio* benchmark of excited states would hardly be affordable for a molecule of the size of the cilium. The study also marks our first use of the connection atom approach implemented in the MOPAC development version by the Persico group.<sup>45,96</sup> In this approach, the QM and MM parts are actually bonded to each other.

From the scientific side it was intended to investigate whether the long-term plan of a functioning artificial cilium can be supported by a dynamics simulation based on realistic and above all explicit AB photodynamics.

## 6.2 Own Contribution

The calculations presented in the publication reproduced in the next subsection were carried out by Tim Raeker during the course of his bachelor thesis. The author supervised all calculations and supplied analysis scripts. Additionally, the interpretation of the results was guided by the author.

## 6.3 Publication

<b>Authors</b>	<i>Tim Raeker, Niss Ole Carstensen and Bernd Hartke</i>
<b>Title</b>	Simulating a molecular machine in action
<b>Submitted</b>	30 May 2012
<b>Accepted</b>	22 August 2012
<b>Publication Data</b>	J. Phys. Chem. A, 2012, <b>116</b> , 11241. DOI: 10.1021/jp305258b

### Abstract

Using QM/MM methods, we have simulated the action of a simple molecular machine, a cilium. It consists of a platform for surface mounting, a photochemical motor unit, and a tail-like effector that amplifies the small-scale conformational change of the motor unit into a larger-scale beating motion usable for molecular transport. In this proof-of-principle application, we show that the techniques used here make it possible to perform such simulations within reasonable real time, if the device action is sufficiently fast. Additionally, we show that this molecular device actually works as intended for one isomerization direction. For the other direction, results are inconclusive, possibly because the total propagation times we can afford are too short to capture the complete event.



## 6.4 Additional information

This section is organized as follows: First the problems in *trans*→*cis*-isomerization are discussed from a different perspective. The latter is a more classical-mechanical view focusing on an aspect of mechanical work, namely the displacement of the phenyl rings during the photoisomerization. This part links to the force-related bachelor projects presented in Chap. 3. The section concludes with an assessment of a brAB-based setup of a "complete" artificial cilium with the FOCI-AM1/MM approach.

As already noted in the publication, the molecular motor that drives our artificial molecular device is essentially a bare AB. Therefore, it is not surprising that the typical AB photodynamics were found in the trajectories. In particular, this does include not only a rotational based reaction mechanism upon  $n \rightarrow \pi^*$  excitation, but also a significantly lower quantum yield for the *trans*→*cis*- photoisomerization. According to Persico *et al*<sup>54</sup> this is one of two well established trends<sup>(1)</sup>, which are found throughout the experimental literature on AB, regardless of the solvent. This is why an initially planned simulation including explicit solvent will not be discussed in this section: Solvent dynamics can be expected to produce essentially the same results. The effect is commonly traced back to different slopes of the excited-state surfaces reflecting the relative stability of the two isomers. For our artificial cilia this means that the reaction from *trans*- towards *cis*-isomer is poorer positioned right from the start.

The direct consequence of the smaller gradients of the potential energy surfaces is that smaller forces act on the molecular framework and less kinetic energy can be assembled and used for the desired beating movement during the course of the dynamics. The trajectory-averaged kinetic energy as a function of the simulation time for the cilium is presented in the left panel of Fig. 6.1. The QM-part of the dynamics, starting from the *cis*-isomer, obviously exhibits more kinetic energy throughout the whole simulation time, although both curves seem to approach each other towards the end of simulation time. The fact that the kinetic energies seem to approach each other points towards an equilibrium state that is presumably reached at some future point not too far away in the dynamics. This assumption can be made keeping in mind that the energy put into the system is defined by the initial  $S_0 \rightarrow S_1$  photo-excitation, which is almost alike in both cases with  $\approx 430$ - $440$  nm. If the latter assumption holds, a successful isomerization beyond our simulation times for the *trans*→*cis*-isomerization unfortunately becomes even more unlikely as trajectories starting from the *cis*-isomer

---

<sup>(1)</sup>The other is that higher excitations lead to lowered quantum yields.

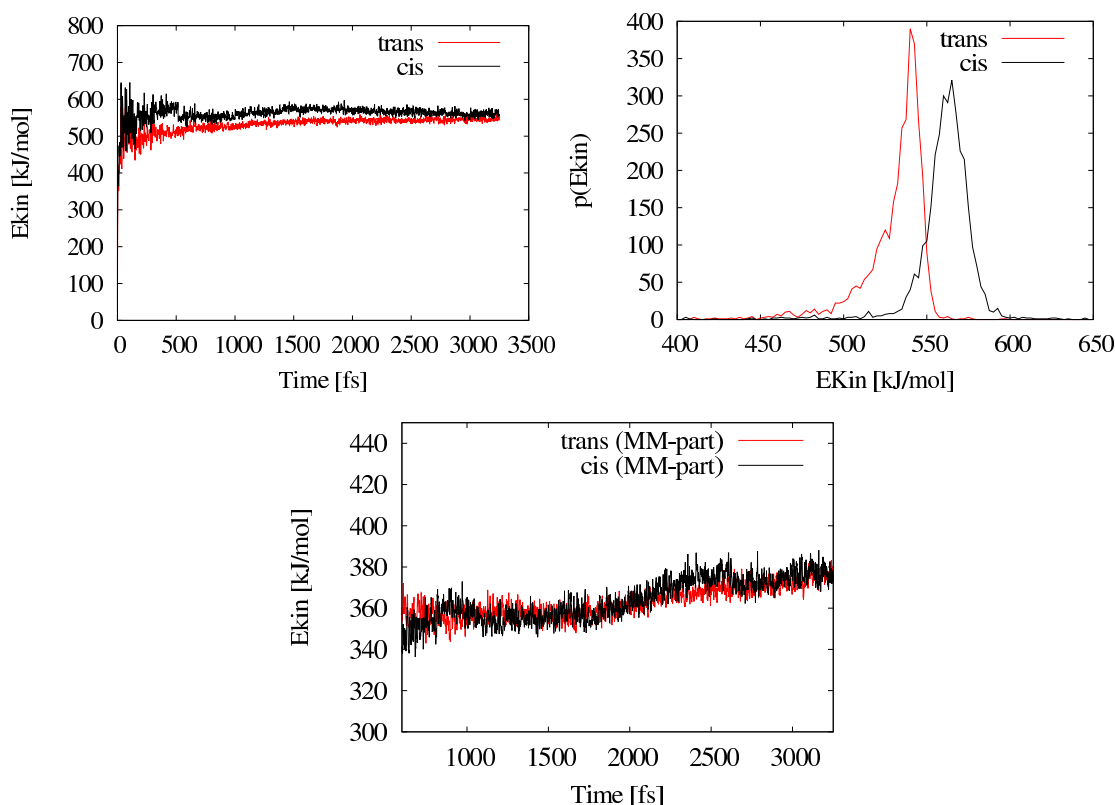


Figure 6.1: Kinetic energies of the *cis*→*trans* and *trans*→*cis* reactions averaged over all trajectories (left panel) and the according distributions of the kinetic energy (right panel). The lower panel shows the kinetic energies of the MM-parts for both isomerization directions (note the different time scales with regard to the above panels).

that reached the *trans*-isomer were not found to experience a back-isomerization, regardless of the initial kinetic energy in the system. This is further supported by the assumption that the kinetic energy, initially located in the azo-moiety, can be considered lost for cilium movement once it also distributes over the internal degrees of freedom of the platform. The latter is depicted in the lower panel of Fig. 6.1, where a slow but steady increase of the kinetic energy in both MM-parts can be seen.

The right panel of Fig. 6.1 shows the according kinetic energy distributions. The most probable velocity can be extracted as the maxima of the distribution functions, i.e. 540 kJ/mol during the *trans*→*cis*- and 565 kJ/mol for the opposite direction, once again highlighting the low efficiency of the *trans*→*cis*- photoisomerization of AB as the reaction starting from the *cis*-isomer releases more kinetic energy (right panel of Fig. 6.1) in a significantly shorter period of time (left panel of Fig. 6.1).

The estimates of the work that can be delivered by AB and brAB in Chap. 3 on

p. 43 were all based on the assumption that in order to calculate the work the path taken by the system is simply described by the length difference of *cis*- and *trans*-isomers. Clearly this is a rather drastic approximation, because it is based on a more inversion-like mechanism rather than a rotational mechanism. If ABs are supposed to drive a molecular machine, as intended in the above publication, the real path should be reconsidered as one additional consequence arising from the problematic *trans*→*cis*-isomerization. In order to estimate a more realistic path, FOCI-AM1

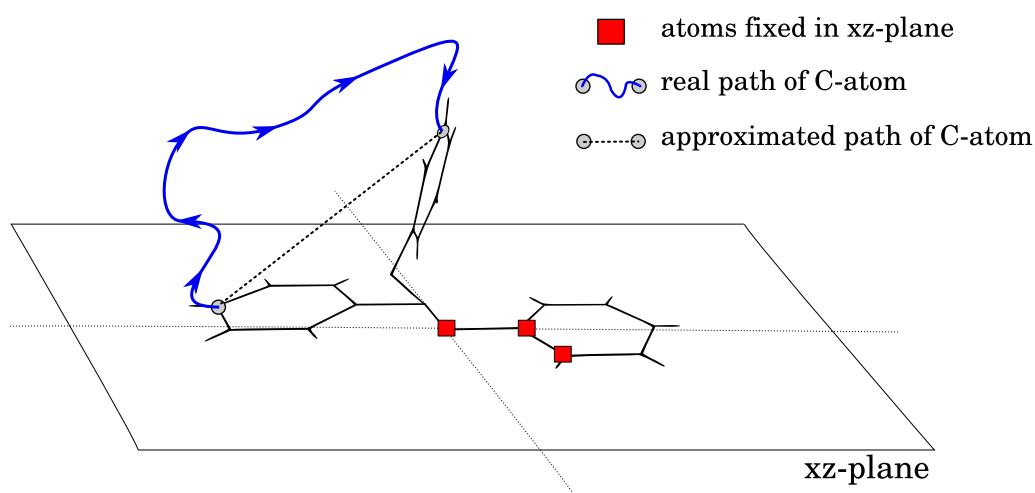


Figure 6.2: Cartoon-like picture of the standard orientation used to calculate the path described by the outer C-atom during AB photoswitching. The estimated path used in the force-related bachelor theses (see Chap. 3, p. 43) is depicted by a dashed line (see text for details).

surface-hopping dynamics were calculated for a bare AB in gas phase. The structures within the movie file of a representative trajectory were all brought into a standard orientation such that one N atom is located at the origin, the according NC-bond located in the x-axis and the phenyl ring rotated into the xz-plane (see Fig. 6.2 for a cartoon-like picture of the standard orientation). After fixing the molecular structures with regard to the external coordinate system, the 3D cartesian coordinates for the outer C-atom of the other phenyl ring can be extracted from the movie files resulting in a more complete estimate of the path described by the outer C-atom. The total distance that has to be taken can afterwards be easily calculated from the 3D path.

The path depicted in Fig. 6.3 still contains approximations, because the path presumably changes once the AB is forced to deliver work, nonetheless, in the opinion of this author, the key features, i.e. smaller gradients and a prolonged reaction path,

are likely to be found in AB-driven molecular machines.<sup>(2)</sup> In particular, it can be expected that the artificial cilium suffers from this effect. Evidence for this assumption arises from the *cis*→*trans*- mechanism reported in the publication that despite being noticeably delayed by the cilium setup, still shows typical AB dynamics.

In Fig. 6.3 the path that is taken during the *trans*→*cis*-photodynamics is three(!) times as long compared to the path of the opposite reaction (41.08 Å vs. 13.68 Å). Given the fact that the CoIn reached upon  $S_0 \rightarrow S_1$  excitation is located at a CNNC dihedral angle of  $\approx 90^\circ$ , i.e. almost exactly "between" the two isomers, this finding may seem counterintuitive, but reflects the discrepancy between the simple 1D textbook and "real" multidimensional (photo)dynamics. The dynamics are not just slowed down by low gradients but the distance that needs to be crossed is actually larger starting from the *trans*-isomer. Since work is force times distance, it can be argued that, if the overall force remains the same, the longer distance means that the reaction is simply less powerful.

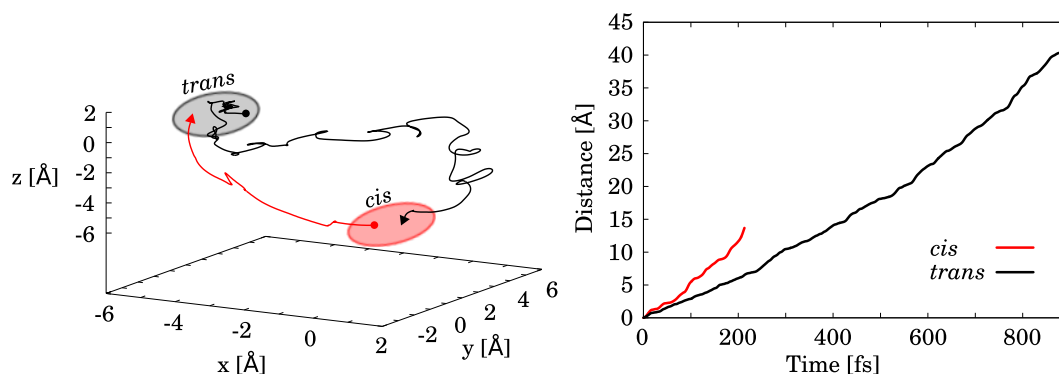


Figure 6.3: Left panel: path taken by the outer C-atom of a phenyl ring during AB photoisomerization. Right panel: the resulting absolute distances as a function of time.

In summary, two effects, inherent to AB photodynamics, seem to be (mainly) responsible for the problems during the *trans*→*cis*-dynamics of our artificial cilium: low efficiency when converting the initial photo-excitation into kinetic energy and a long-winded movement towards the *cis*-isomer.

Based on the paths discussed in the above paragraphs it appears sensible to consider a cilium setup that is driven by a brAB unit instead of an AB unit. The corresponding paths for the brAB photoisomerizations are compared to the AB paths within Fig. 6.4. When comparing the trajectories starting from the *cis*-isomer in the

<sup>(2)</sup>Please note that this will not hold for sterically hindered AB derivatives, for example brAB, that exhibit a different, less space-consuming, hula-twist mechanism.

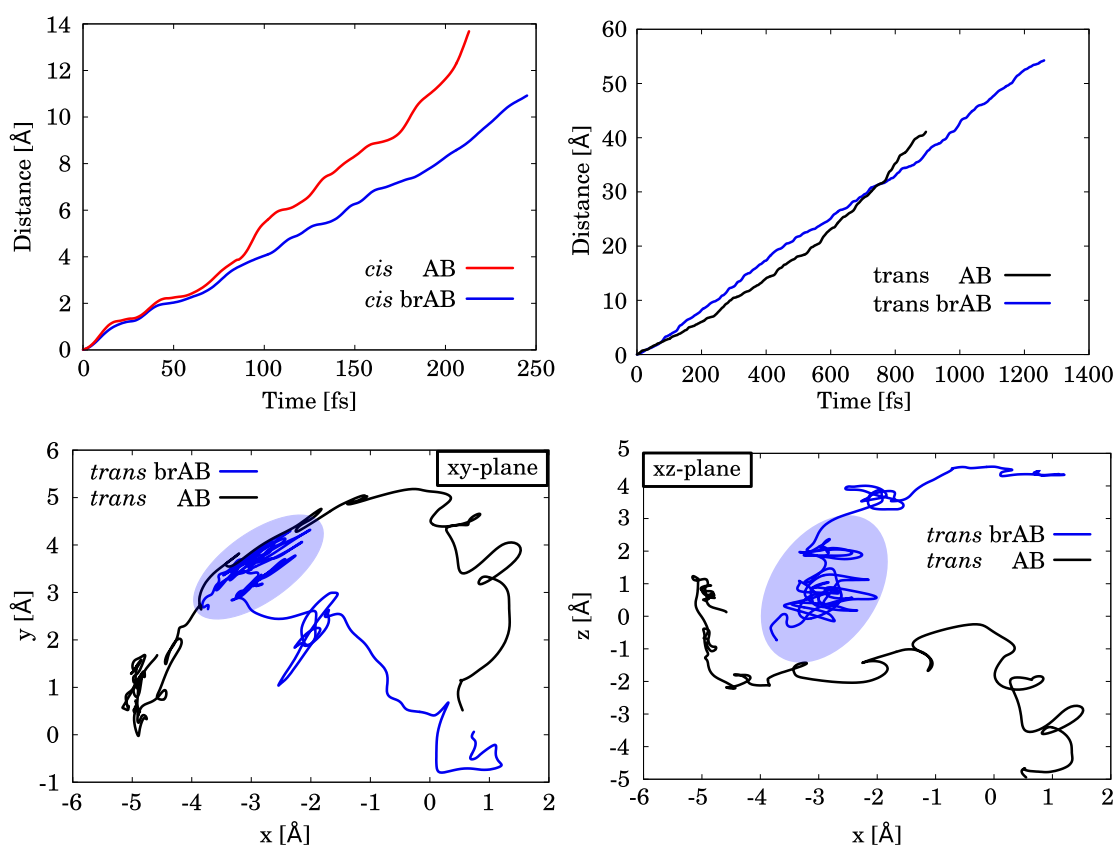


Figure 6.4: Top panels: Comparison of absolute distances taken by the outer C-Atoms of a phenyl ring during brAB and AB photoisomerization. Lower panels: projections onto the xy-plane(left) and xz-plane(right) of the according absolute paths for *trans*-brAB and *trans*-AB. The coordinates of the intermediate ground-state structure of brAB are indicated by a light blue region.

upper left of Fig. 6.4 it becomes obvious that the actual path is clearly reduced in the case of brAB although not as pronounced as one might expect. The movement was found to be more directed, which can easily be explained by the ethylenic bridge that prevents the phenyl rings from taking excursions around the direct path. In terms of a molecular machine this (more) direct transformation of initial potential energy into a straightforward movement is clearly beneficial. Since the *cis*→*trans*-isomerization was already successful with the plain AB as reported above, the *cis*→*trans*-isomerization employing brAB should be at least equally efficient.

The opposite isomerization reaction will most likely behave in a different manner. Due to the relatively slow reorientation of the molecular framework on the ground-state surface the total distance that has to be covered is significantly larger than in the case of AB, which is clearly non-beneficial for usage as a molecular motor. Nonetheless, once the projections of the actual paths on the xy- and xz-plane, depicted

in the bottom panels of Fig. 6.4, are taken into account it can be seen that the persistence in the intermediate ground-state structure, highlighted as a light blue region, is responsible for this effect and that once the molecular framework adapts to the shape of the *cis*-isomer, i.e. the phenyl rings close, the path is again straightforward, while the corresponding AB path appears to be significantly more widespread. Whether or not this affects the efficiency as a molecular motor is hard to put into a realistic estimate, but to the author it seems plausible that the longer path taken by brAB might not be as dramatic as expected upon first sight. Moreover, the reader should be reminded that in the case of brAB the *cis*-isomer is the thermodynamically stable one. The back reaction from the *trans*-isomer is promoted anyways in an experimental setup, even if the reaction should exceed the simulation times that can be afforded running FOCI-AM1 surface-hopping dynamics.

# QM/MM PHOTODYNAMICS OF A BRIDGED AZOBENZENE DERIVATIVE

## 7.1 Scope of the project

The project targeted an urgent question raised in the (theoretical) literature on brAB photodynamics: What is the influence of the solvent? Since the pioneering work published by Siewertsen *et al.*<sup>97</sup> and the first theoretical follow-up publications by Böckmann *et al.*<sup>72</sup> and our group,<sup>73</sup> the role of the solvent environment became more and more important. Initially Böckmann and coworkers assumed a "qualitative insensitivity to solvent effects" <sup>(1)</sup>. However, the follow-up publication of the same authors<sup>73</sup> claimed that the *cis*→*trans* photoisomerization is affected by a "pronounced solvent effect". Another typical example comes from the density-functional-based tight-binding study of the *cis*→*trans*- isomerization by Jiang and coworkers that suspected "quantitative differences" in their quantum yields might be due to the gas-phase dynamics.<sup>74</sup> Again, already the next publication by the same authors using the same method on the opposite isomerization direction seemed unaffected by the gas-phase nature of the dynamics.<sup>75</sup> In a nutshell, the obscure effect of the solvent on the quantum yields just needs clarification.

Apart from the theoretical considerations it is also worth noting that *n*-hexane solvent is usually expected to show very little influence on a chemical reaction, which

---

<sup>(1)</sup>In direct contrast to the publication from our group presented in Chap. 4

contradicts the theoretical predictions mentioned above. By employing QM/MM surface-hopping dynamics the following work was intended to shed light on the role of the solvent and marks the first study on brAB including explicit *n*-hexane solvent.



## 7.2 Own Contribution

All calculations were carried out by the author, including *ab-initio* and DFT-D benchmark calculations. The same applies to the results obtained from the trajectories, in particular mechanisms, quantum yields and spectra. Although own solvent boxes were prepared (see Sec. 7.4), the below publication employed a solvent box kindly provided by the group of Prof. M. Persico simply because it was already present at the start of the project.

## 7.3 Publication

<b>Author</b>	<i>Niss Ole Carstensen</i>
<b>Title</b>	QM/MM Surface-hopping dynamics of a bridged azobenzene derivative
<b>Submitted</b>	08 February 2013
<b>Accepted</b>	05 July 2013
<b>Publication Data</b>	Phys. Chem. Chem. Phys., 2013, <b>15</b> , 15017. DOI: 10.1039/C3CP50606A, 2013

### Abstract

Ethylene-bridged azobenzene (diazocine) has been shown to have superior photochemical properties. So far, however, experimental and theoretical quantum yields did not match, not even qualitatively. Here, a large-scale QM/MM surface-hopping study of this molecule is presented. For both photo-isomerization directions, surprisingly prominent solvent effects are found and analyzed by detailed comparisons against gas phase dynamics and experimental data. By taking explicit n-hexane solvent into account, the quantum yields change markedly and approach the experimental values, where the same solvent was used.

## 7.4 Additional Information

This section is organized as follows: First unpublished results from dynamics employing cyclohexane and methanol solvent boxes are presented, before the solvent-chromophore interaction in *n*-hexane is discussed in more detail also with regard to the benchmark procedure chosen. Please note that the first few paragraphs dealing with different solvent boxes are intended to give the reader an idea on how error-prone QM/MM dynamics actually are and how errors luckily often manifest themselves at an early stage of the calculations.

In addition to the *n*-hexane solvent box, a methanol and cyclohexane solvent box were prepared for ground-state Brownian dynamics (see Chap. 2.4, p. 39 for details on the solvent box setup). The reason for preparing a cyclohexane solvent box was the higher dynamic viscosity of 0.9748 mPas compared to *n*-hexane with a corresponding dynamic viscosity of 0.3131 mPas, while preserving the argument of primarily steric hindrance as supported by the small dielectric constants of 1.989 F/m and 1.897 F/m for cyclohexane and *n*-hexane respectively.<sup>98–100</sup> Experimenting with solvents of different viscosity was initially motivated by the prominent role of solvent viscosity in the photochemistry of the parent compound AB, where quantum yields and transient signals are significantly affected by the choice of solvent.<sup>101</sup> Strong electrostatic interactions, as expected with the methanol solvent, are presumably not correctly described by the QM/MM approach used, unless great effort is spent in reparametrizing the solvent chromophore interaction. The methanol solvent box used was supplied by the group of Prof. Persico and (trial) dynamics were run in order to check for the limits of our semiempirical QM/MM method, already expecting failure. In summary, the first paragraph below is intended to shed some light on the limitations of the QM/MM ansatz as is, i.e. without any further reparametrizations.

Fig.7.1 shows snapshots taken from a 30 ps long brownian trajectory at a temperature of 300 K of *cis*-brAB in a solvent sphere consisting of 181 cyclohexane molecules. In direct contrast to the *n*-hexane dynamics the simulation predicts that brAB is not soluble in cyclohexane as the chromophore is almost completely expelled from the solvent sphere during the 30 ps ground-state dynamics. The dynamics starting from the *trans*-isomer are not shown in Fig. 7.1, but show a similar behavior. The chromophore is also leaving the solvent sphere although slightly slower. As to whether or not brAB is soluble in cyclohexane is a question easily answered by any classical

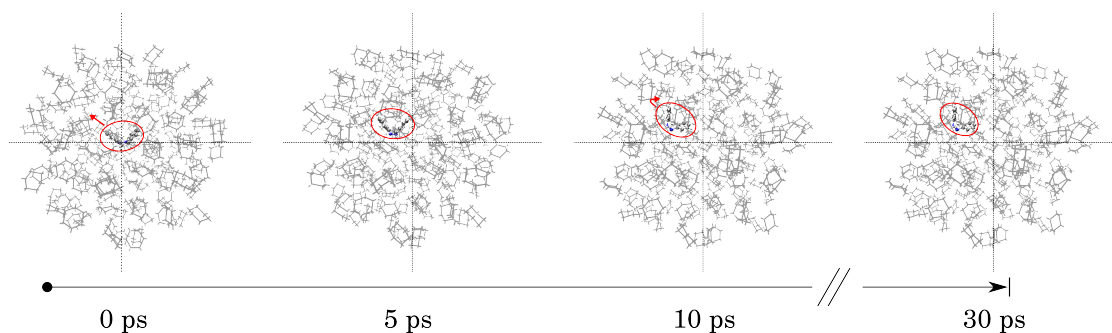


Figure 7.1: Snapshots from a FOCI-AM1/OPLSAA-L ground-state trajectory @300K of *cis*-brAB inside a *n*-hexane solvent sphere. The center of the solvent sphere is indicated by dotted lines and the chromophore is framed red for clarifying the movement of the chromophore inside the sphere.

chemist<sup>(2)</sup>. Completely independent from this question is the fact that the simulations led to a dead end: Either brAB is not soluble or the chosen ansatz cannot be used for the problem at hand without a tedious reparametrization. Given that cyclohexane and *n*-hexane differ only slightly in their physical properties, this unexpected outcome clearly shows a typical problem encountered when running large-scale QM/MM calculations. Simple assumptions like "the *n*-hexane-brAB interaction is described at least qualitatively correct, therefore simulating a cyclohexane solvent box will likely be an easy task" can't be naively made.

Fig. 7.2 shows snapshots from ground-state brownian trajectory at 300 K of *cis*-brAB in a methanol solvent sphere. As already pointed out in the introduction, the electrostatic interaction between methanol and brAB was expected to be more troublesome in terms of our QM/MM approach. In Fig. 7.2 the fatal consequences of an inadequate description of the electrostatic interactions are clearly visible. Very soon after the trajectory is started nearby methanol molecules are rapidly drawn towards the chromophore until the chromophore and the solvent molecules finally collide. Immediately after the collision, the molecules virtually explode, as unphysical giant gradients caused by the collision presumably lead to a breakdown of the Verlet algorithm and an exploding trajectory. The behaviour reported above could also be caused by a starting structure that contains almost-collisions between the chromophore and the solvent molecules. This is why different starting structures with solvent pockets of different sizes were prepared and tested, but all trajectories showed explosive behaviour, pointing towards a dramatically wrong description of the methanol-brAB electrostatics. It should be noted that early attempts of preparing

<sup>(2)</sup>The experimental literature on brAB does not mention cyclohexane as a solvent at the present moment.

brAB-*n*-hexane solvent spheres suffered from a similar difficulty until van der Waals radii of the chromophore and solvent molecules were taken into account for the setup of the starting structures (see also Chap.2.4, p. 39 and Fig. 7.2 below).

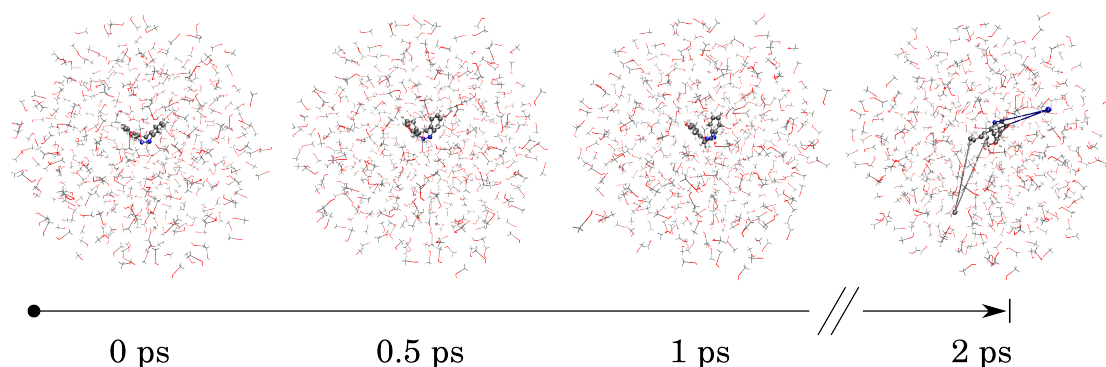


Figure 7.2: Snapshots from a FOCI-AM1/OPLSAA-L ground-state trajectory @300K of *cis*-brAB inside a methanol solvent sphere.

Luckily, the dynamics using the *n*-hexane solvent did not show any of the above shortcomings.

Fig. 7.3 shows a 3D rendered view of the solvent pocket, in order to help the reader's spatial perception. A more rational estimate of the solvent sphere is presented in the lower panel of the same figure where the pair radial distribution functions ( $g(r)$ , see also Chap. 2.3, p. 37) are shown. The functions were calculated from the 30 ps long ground-state trajectories of the two isomers. Please note that the functions shown reflect first order, i.e. pairwise, interactions and do not contain information on orientation of the solvent molecules or the chromophore, but the positions of the according center of masses. Also, the simulation times of 30 ps are significantly shorter than in usual MD simulations seriously limiting the statistical reliability of the distribution functions. Nonetheless, first qualitative information on the solvent shell can nicely be extracted from the distribution functions.

First of all, the proposed altering of starting structures in the case of the *cis*-isomer reflects nicely in the first peak located at 2Å. Obviously it is very likely to find solvent molecules in close vicinity to the center of mass of *cis*-brAB, which is located above the central ring system between the two phenyl rings. In the case of *trans*-brAB a slightly increased probability at around 4Å is found, less pronounced and more broadened compared to the other isomer. This can readily be explained by weaker but still more or less equilibrated solvent-chromophore interactions, resulting in a loose short range

order of the solvent molecules neighboring *trans*-brAB. The absence of the typical additional peaks is due to the short simulation time scales and the usage of a solvent sphere without periodic boundaries.

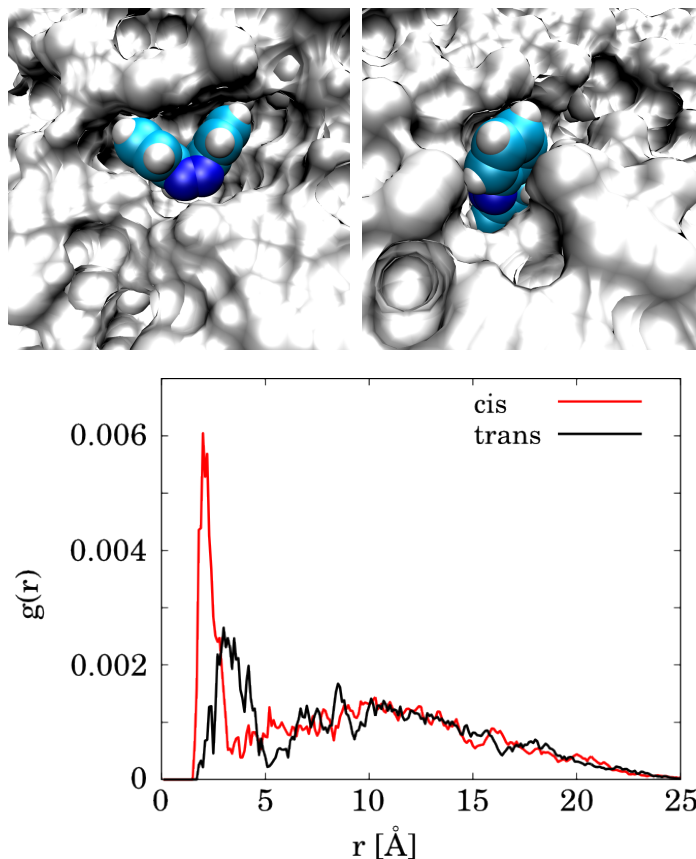


Figure 7.3: Two snapshots taken from the end of two 30ps, FOCI-AM1/OPLSAA-L ground-state trajectories @300K. The top left picture shows *cis*- and the top right picture *trans*-brAB inside their *n*-hexane solvent pockets. For illustrating proportions all atoms were rendered with their according van-der-Waals radii and solvent molecules blocking the view were removed. Lower panel: pair radial distribution functions calculated from the same two ground-state trajectories of the two brAB isomers.

During the preparation of the above publication, attempts were made to quantify the interactions between the *cis*-isomer and the *n*-hexane solvent molecule located between the two phenyl rings by running DFT-D/TVZ calculations. A geometry optimization was carried out, starting from a dimer structure of the two molecules taken from the last frame of the Brownian ground-state trajectory. Compared with a geometry optimization of the molecules spaced 35Å apart, i.e. outside the solvent sphere, the dimer complex was found to be more stable by 0.59 kJ/mol. This finding

would correspond to a very weak van-der-Waals bonding, but unfortunately the interaction is not outside the error range of a DFT-D treatment, which is given to be 1.34 kJ/mol in the case of the benzene-CH<sub>4</sub> dimer.<sup>38</sup>

Quantifying the subtle interaction between *n*-hexane and the chromophore turned out to be a challenging task, because the RI-MP2/aug-cc-pVTZ calculations presented in the publications cannot serve as an absolute benchmark either since they are affected by basis set superposition errors (BSSE). The BSSE, computed following the approach of Boys and Bernardi,<sup>102</sup> was found to be rather big with 9.8 kJ/mol on average.<sup>(3)</sup> Given the fact that a single-point calculation of the dimer structure, consisting of 48 atoms, takes 20 h on average, a geometry optimization on this level of theory would hardly be affordable and becomes completely impracticable once the basis is increased and/or BSSE corrections are added in order to minimize the error. Also, consideration of the relative orientation of the molecules would increase the complexity of the problem even further, which is why the attempts of quantifying the *n*-hexane-chromophore interaction were finally stopped. What can be said is that, according to DFT-D, they are of the order of very weak van-der-Waals interactions.

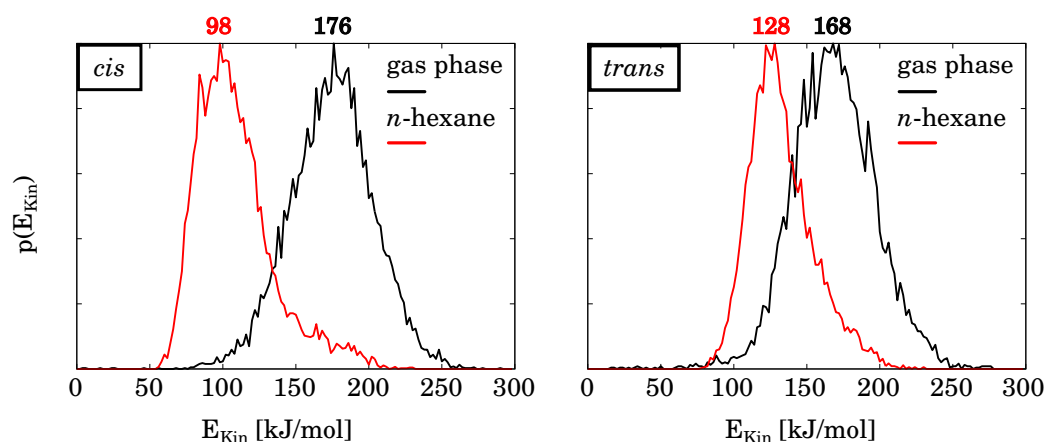


Figure 7.4: Distribution of the kinetic energy of brAB during the last picosecond, both in *n*-hexane solvent and gas phase, for the two isomers of brAB. The most probable kinetic energies for all graphs are given on top of the graphs and are averaged over a set of 14 selected trajectories.

The solvent cooling, beneficial for the *cis*→*trans*- and hindering for the opposite photoisomerization, is shown in Fig. 7.4. In order to illustrate the solvent cooling, the distribution of the kinetic energy of brAB during the last picosecond of a representative set of 14 surface-hopping trajectories was calculated for both gas phase and

<sup>(3)</sup>Calculated for 4 randomly chosen structures from the benchmark set.

QM/MM trajectories. During the last picosecond the trajectories have returned to the ground-state and the kinetic energy begins to distribute over the internal degrees of freedom of the chromophore, or of the chromophore and the solvent in the case of the QM/MM trajectories. It should be noted that the trajectories very likely do not reach full equilibrium during the 2.5 ps simulation time. A reasonable estimate of the solvent cooling was published by Siewertsen *et al.*<sup>97</sup> According to Siewertsen and coworkers the vibrational cooling takes place on a time scale of 5ps, i.e. twice as long as the simulation time. Apart from that, the very efficient solvent cooling of the *cis*-isomer discussed in the publication manifests itself nicely in the difference of 78 kJ/mol between the most probable kinetic energies. Note that the according difference between gas phase and QM/MM dynamics is only half as much with 40 kJ/mol in the case of the *trans*-isomer, although the corresponding gas phase simulations differ by only 8 kJ/mol. The latter point clearly distinguishes the solvent cooling from effects arising from the different reaction pathways of the two isomers.

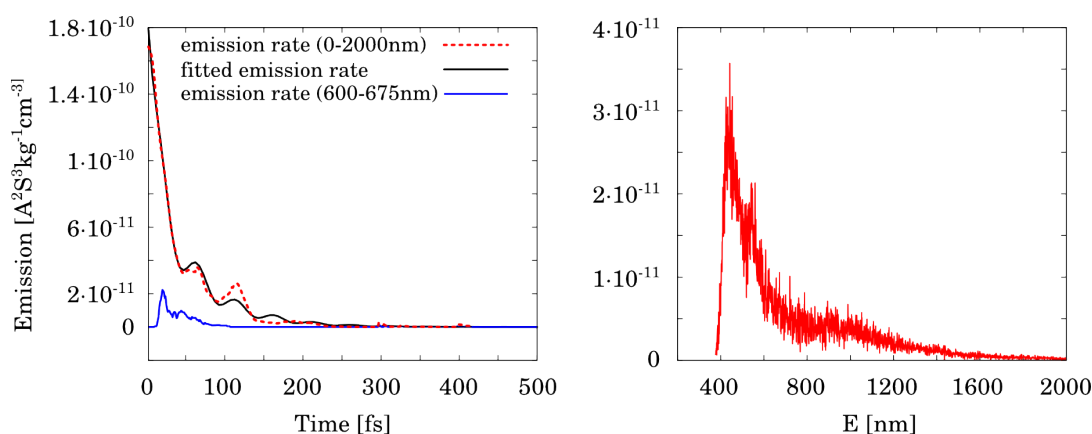


Figure 7.5: Left panel: Simulated time-resolved emission rates for the *cis*→*trans* photoisomerization of brAB. The red dotted line is the simulated emission rate taken into account emission wavelengths from 0 up to 2000nm, whilst the blue curve is limited to the experimental observation window of 600-675nm. The black curve is a fit to a bi-exponential function with a decaying oscillatory component with a frequency of  $632 \pm 6 \text{ cm}^{-1}$ . Right panel: Simulated total fluorescence spectrum.

As concluding additional information, Fig. 7.5 shows the computed fluorescence spectra (see Chap. 2.3, p. 34 for computational details). In the above publication fluorescence spectra were not part of the results, due to the experimental findings by Siewertsen *et al.* who reported ultrafast fluorescence decays and very low fluorescence intensities. The authors predicted an ultrafast spectral red-shift of the fluorescence signal out of the experimental observation window between 600-675nm. The latter assumption is clearly supported by the simulated total fluorescence spectrum, where

notable intensity is found in a broad range up to  $\approx 1200$  nm. Unfortunately the peak of the spectrum is also located outside of the experimental observation window albeit at the blue side of the spectrum at  $\approx 440$  nm, therefore the computed total fluorescence quantum yields are one order of magnitude smaller if computed inside the range of 600-675nm, i. e.  $\Phi_{\text{Tot.}}=6.73 \cdot 10^{-9}$  for the total spectrum and  $\Phi_{600-675\text{nm}}=5.51 \cdot 10^{-10}$  for the cutout. Despite notable fluorescence intensities outside the experimental observation window, the fitted time constants of  $\tau_1=66.95 \pm 0.35$  fs and  $\tau_2=19.13 \pm 0.11$  fs indicate that the fluorescence decay is ultrafast and supports the experimental findings of fluorescence decays faster than 150 fs.



## SUMMARY

A reaction mechanism for the photoisomerization following  $n \rightarrow \pi^*$  excitation of a bridged azobenzene derivative (brAB) was proposed with the help of surface-hopping dynamics. For both isomerization directions, *cis*→*trans* and *trans*→*cis*, the mechanism is based on a rotational movement around the N=N bond. As with other sterically hindered azobenzene derivatives, the excited-state dynamics are primarily focused on the azo-moiety and are virtually space-conserving with regard to the molecular framework (hula-twist) for both isomers. Starting from the thermodynamically stable *cis*-isomer the reaction path is barrierless and proceeds via a straightforward rearrangement of the molecular framework, initiated by the rotation around the N=N bond. The opposite photoreaction shows a remarkably different signature, since the rotation around the N=N bond does not initiate an instant rearrangement of the overall molecular framework. Instead, once the azo-moiety has reached the product conformation, an intermediate structure is formed, sharing the overall shape of the educt but the azo-group configuration of the product. The formation of the product structure from this intermediate takes place on a disadvantageous timescale of about one picosecond.

In the first QM/MM surface-hopping simulation of brAB photodynamics, including explicit *n*-hexane solvent, the role of the solvent was quantified. Due to the space conserving mechanism, the solvent hardly interferes with the excited-state dynamics. Instead, the ground-state equilibrium structure of the *cis*-isomer is altered, because solvent molecules preferably locate between the two phenyl rings of the more closed *cis*-structure. After leaving the excited state, the hot *trans*-product is rapidly stabilized by efficient solvent cooling, causing an overall increase in the quantum yield. The

reversed isomerization is affected by the solvent only during the formation of the *cis* product structure on the ground-state surface, which causes a decrease in the quantum yield. In summary, these simulated quantum yields are the first ones clearly reproducing the correct experimental trend.

In the bachelor thesis of A. Kostevic first attempts towards simulating part of the  $\pi \rightarrow \pi^*$  photodynamics of brAB were performed, by running surface-hopping dynamics for the  $S_0 \rightarrow S_2$  excitation. Unfortunately, the results are presumably questionable, since simultaneous multireference *ab-initio* calculations of J. B. Schönborn suggested that the characters of the electronically excited states in azobenzene differ significantly from those in brAB. As a consequence, the active space and the new parameters of the current semiempirical ansatz are likely unusable for simulating the dynamics of higher excitations.

Based on the proposed reaction mechanism for brAB, a molecular design project was set up and realized in R. Höppner's bachelor thesis. With the aim of proposing a suitable modification of the ethylenic bridge of brAB, in order to ease the formation of the *cis*-isomer on the ground-state surface during the *trans* $\rightarrow$ *cis* isomerization. A promising bridging pattern was found, employing an ether bridge. Synthesis attempts of the proposed molecule **k** are currently carried out in the Herges and Staubitz groups.

Another molecular design approach combining global optimization techniques with the semiempirical description of vertical excitation energies was realized in a cooperation with J. M. Dieterich. By using genetic algorithms, a substitution pattern for brAB was optimized, shifting the vertical excitation energies of both isomers towards wavelengths available in cheap commercial laser pointers. The resulting molecules were simulated in a proof-of-principle surface-hopping dynamics simulation and were found to show successful isomerization with high quantum yields. Linking to the thesis of R.Höppner, it was found that push-pull substitution patterns are likely promoting the formation of the *trans*-isomer during *cis*-photodynamics by lowering the ground state barrier.

The setup of a complete artificial cilium bound to a platform for surface mounting was simulated in the bachelor thesis of T. Raeker. While the kinetic energy released by the photoisomerization starting from the *cis*-isomer was successfully transformed into the desired beating motion of the complete setup, the reverse reaction could not be observed. Possible explanations include the limited simulation timescales, the in-

ability to simulate continuous pumping into photostationary states, the long-winded torsional movement of the azobenzene moiety and missing quantum decoherence. As a whole, the general molecular setup still appears encouraging, especially if azobenzene is replaced with brAB.

The question how much work can be delivered by brAB upon photoisomerization was addressed in the bachelor thesis of J. Müller. By running surface-hopping dynamics with brAB subject to artificial external forces, the amount of work was estimated to be  $48 \pm 6.0$  kJ/mol, which is half of the work delivered by naked azobenzene in an analog setup.<sup>60</sup> Another force-related effect was studied in the bachelor thesis of R. Scholz, where the effect of external forces on the vertical excitation energies of AB was simulated. According to the simulation, the main effect is found in the UV/Vis absorption spectra of the *cis*-isomer. There the absorption bands all experience a red shift and a significant broadening.

Azobenzene derivatives that are subject to environmental constraints (pBAAAB) were studied in the bachelor thesis of J. Steffen. The incorporation into the polymer matrix significantly affects the ground-state equilibrium structures: While the *cis*-isomer is stretched inside the polymer pocket, the *trans*-isomer is compressed. The simulated fluorescence decay is in good agreement with the experimental spectra for the plain BAAAB chromophore, but slightly overestimated for the polymer pBAAAB. Nonetheless, the results for the polymer agree qualitatively with the experimental findings despite the very simple polymer model.

Based on the works summarized above, numerous follow-up projects come to mind. Some of these are already sketched in the additional information given at the end of the according chapters. From technical side, immediate new opportunities arise from a very recently obtained extended MOPAC development version, including the newest overlap-based decoherence correction (ODC),<sup>68</sup> spin-orbit coupling for simulating the dynamics of spin-forbidden processes<sup>103</sup> and the explicit interaction with an oscillating electric field. The reparametrization of the FOCI-AM1 semiempirics for usage with non-AB-photoswitches remains a future target, although the MNDO99 program suite offers the computationally more expensive but flexible OMx/GUGACI alternative.<sup>104</sup> On the chemical side the list of potential applications is steadily growing. Especially the area of photo-driven molecular machinery, targeted in the collaborative research project SFB 677 "Function by switching" of the University of Kiel, offers many perspectives. At first, work in sub-project A01 on azobenzene derivatives

experiencing intra- and inter-molecular sterical and mechanical stress are very well suited for surface-hopping dynamics as shown with brAB or pBAAAB. In particular, the ultrafast time resolved data obtained from the Temps group marks the most direct benchmark for the dynamics results available. Due to the QM/MM nature of the ansatz even very large systems of several thousand atoms can be studied. For example, the dynamics simulation of photoswitchable antifreeze proteins, photoswitchable FimH ligands or mechanophores as planned by Staubitz and Adelung groups are in principle possible and would definitely be a challenging but highly interesting new task.

## ACKNOWLEDGMENTS

I would like to thank Bernd Hartke, my tutor, for the continuous support and promotion I received throughout all the years. His progressive thinking and high scientific ideals truly set an example for me.

I would like to thank Prof. Dr. Friedrich Temps for accepting to be referee for this work.

All the past and present members of the Hartke group Frank, Jan, Mats, JD, Florian, Boyke, Sushi, Tim, Ronja, Insa, Julian, David I would like to thank for the great time we had. Working with you guys really was a grand experience for me.

I would like to thank Tim, Julian, Roland, Julien, Angelika and Ronja for the nice bachelor projects. Passing on my knowledge to you was a valuable experience for me.

Thanks to all my band mates from Ballynacally, The Chancers, Hans Dans, Kaluun and all the other projects for the great craic. Rock agus Roll, Lads!

Thank you, Jan, for the countless moments of pure happiness playing tunes or going fishing, not to mention all the other completely ludicrous situations we have been through. Thanks to you, I will never ever be short of stories to tell...

My family I would like to thank for the virtually unlimited support I received for all my life. Without them this work would not have been possible.

Thank you, Michelle, for every single moment we spent. I am so fortunate to have you in my life.



## BIBLIOGRAPHY

- [1] E. Mitscherlich, *Annalen der Pharmacie* 12(2-3), 311 (1834).
- [2] G. Hartley, *Nature* 140, 281 (1937).
- [3] C. Ciminelli, G. Granucci, M. Persico, *Chem. Eur. J.* 10, 2327 (2004).
- [4] M. Kasha, *Discuss. Faraday Soc.* 9, 14 (1950).
- [5] S. Monti, G. Orlandi, P. Palmieri, *Chem. Phys.* 71(1), 87 (1982).
- [6] H. Rau, E. Lueddecke, *J. Am. Chem. Soc.* 104(6), 1616 (1982).
- [7] B. K. Pathem, S. A. Claridge, Y. B. Zheng, P. S. Weiss, *Annu. Rev. Phys. Chem.* 64(1), 605 (2013).
- [8] P. Cattaneo, M. Persico, *Phys. Chem. Chem. Phys.* 1, 4739 (1999).
- [9] T. Ishikawa, T. Noro, T. Shoda, *J. Chem. Phys.* 115(16), 7503 (2001).
- [10] A. Cembran, F. Bernardi, M. Garavelli, L. Gagliardi, G. Orlandi, *J. Am. Chem. Soc.* 126(10), 3234 (2004).
- [11] E. Wei-Guang Diao, *J. Phys. Chem. A* 108(6), 950 (2004).
- [12] C. Ciminelli, G. Granucci, M. Persico, *J. Chem. Phys.* 123, 174317 (2005).
- [13] R. Liu, A. E. Asato, *Proc. Natl. Acad. Sci.* 82(2), 259 (1985).
- [14] W. Fuß, C. Kosmidis, W. E. Schmid, S. A. Trushin, *Angew. Chem. Int. Edit.* 43(32), 4178 (2004).
- [15] Y. Imamoto, et al., *Angew. Chem.* 115(31), 3758 (2003).
- [16] G. Krishnamoorthy, A. E. Asato, R. S. Liu, *Chem. Commun.* (17), 2170 (2003).
- [17] G. Krishnamoorthy, et al., *Res. Chem. Intermediat.* 30 (2004).

- [18] W. L. Jorgensen, J. D. Madura, C. J. Swenson, *J. Am. Chem. Soc.* 106, 6638 (1984).
- [19] W. L. Jorgensen, D. S. Maxwell, J. Tirado-Rives, *J. Am. Chem. Soc.* 117, 11225 (1996).
- [20] G. A. Kaminsky, R. A. Friesner, J. Tirado-Rives, W. L. Jorgensen, *J. Phys. Chem. B* 105, 6474 (2001).
- [21] R. B. Murphy, M. D. Beachy, R. A. Friesner, M. N. Ringnalda, *J. Chem. Phys.* 103, 1481 (1995).
- [22] E. Schrödinger, *Phys. Rev.* 28, 1049 (1926).
- [23] D. R. Hartree, *Proc. Camb. Phil. Soc.* 24, 89 (1928).
- [24] J. C. Slater, *Phys. Rev.* 34, 1293 (1929).
- [25] D. R. Hartree, W. Hartree, *Proc. R. Soc. Lond. A* 150, 9 (1935).
- [26] F. Jensen, *Introduction to Computational Chemistry*. John Wiley and Sons Ltd., 2nd edn. (2006).
- [27] M. J. S. Dewar, E. G. Zoebisch, E. F. Healy, J. J. P. Stewart, *J. Am. Chem. Soc.* 107(13), 3902 (1985).
- [28] T. Cusati, et al., *J. Phys. Chem. A* 116(1), 98 (2012).
- [29] N. Rösch, P. Sandl, A. Görling, P. Knappe, *Int. J. Quantum Chem.* 34(S22), 275 (1988).
- [30] G. Granucci, A. Toniolo, *Chem. Phys. Lett.* 325(1–3), 79 (2000).
- [31] G. Granucci, M. Persico, A. Toniolo, *J. Chem. Phys.* 114(24), 10608 (2001).
- [32] A. R. Leach, *Molecular Modelling, Principles And Applications*. Pearson Education Limited, 2nd edn. (2001).
- [33] M. Feyereisen, G. Fitzgerald, A. Komornicki, *Chem. Phys. Lett.* 208(5–6), 359 (1993).
- [34] D. E. Bernholdt, R. J. Harrison, *J. Chem. Phys.* 109(5), 1593 (1998).
- [35] D. E. Bernholdt, R. J. Harrison, *Chem. Phys. Lett.* 250(5–6), 477 (1996).
- [36] F. Weigend, M. Häser, H. Patzelt, R. Ahlrichs, *Chem. Phys. Lett.* 294(1–3), 143 (1998).



- [37] A. D. Becke, *J. Chem. Phys.* 107(20), 8554 (1997).
- [38] S. Grimme, *J. Comput. Chem.* 27(15), 1787 (2006).
- [39] A. Warshel, M. Levitt, *J. Mol. Biol.* 103(2), 227 (1976).
- [40] S. Dapprich, I. Komáromi, K. S. Byun, K. Morokuma, M. J. Frisch, *J. Mol. Struct. THEOCHEM* 462, 1 (1999).
- [41] I. Antes, W. Thiel, *J. Phys. Chem. A* 103(46), 9290 (1999).
- [42] A. Toniolo, C. Ciminelli, G. Granucci, T. Laino, M. Persico, *Theor. Chem. Acc.* 111(2-6), 270 (2004).
- [43] P. Carloni, U. Rothlisberger, M. Parrinello, *Accounts Chem. Res.* 35(6), 455 (2002).
- [44] T. Cusati, *Computational simulation of the excited states dynamics of azobenzene in solution.*, Ph.D. thesis, , Università degli studi di Pisa, (2009), group of M. Persico.
- [45] J. Stewart, *J. Comput. Aided Mol. Des.* 4, 1 (1990).
- [46] P. Cattaneo, G. Granucci, M. Persico, *J. Phys. Chem. A* 103(18), 3364 (1999).
- [47] W. Van Gunsteren, H. Berendsen, *Mol. Phys.* 45(3), 637 (1982).
- [48] N. Bohr, *Zeitschrift für Physik* 2(5), 423 (1920).
- [49] E. J. Heller, *J. Chem. Phys.* 62, 1544 (1975).
- [50] N. L. Doltsinis, 'Nonadiabatic dynamics: Mean-field and surface hopping', Lecture Notes, John von Neumann Institute for Computing, Jülich (2002).
- [51] J. C. Tully, *Chem. Phys.* 93, 1061 (1990).
- [52] C. Zhu, S. Nangia, A. W. Jasper, D. G. Truhlar, *J. Chem. Phys.* 121(16), 7658 (2004).
- [53] C. Zhu, A. W. Jasper, D. G. Truhlar, *J. Chem. Theory Comput.* 1(4), 527 (2005).
- [54] G. Granucci, M. Persico, *Theor. Chem. Acc.* 117, 1131 (2007).
- [55] W. Humphrey, A. Dalke, K. Schulten, *J. Molec. Graphics* 14.1, 33 (1996).
- [56] J. W. Ponder, *TINKER 4.2 - Software Tools for Molecular Design* (2004), Washington University School of Medicine, St. Louis, MO; <http://dasher.wustl.edu/ffe/>.

- [57] J. Müller, 'Simulationen ultraschneller photochemischer Reaktionen eines verbrückten Azobenzols unter Einfluss externer Kräfte', *B.Sc. thesis*, University of Kiel, (2010).
- [58] 'Christian-Albrechts-Universität Kiel; Collaborative Research Center (SFB) 677 Function by Switching; August 2013; [http://www.sfb677.uni-kiel.de/pages\\_en/projekte.html](http://www.sfb677.uni-kiel.de/pages_en/projekte.html)'.
- [59] R. Scholz, 'Auswirkungen einer simulierten mechanischen Kraft auf ein schaltbares Molekül und dessen UV-Spektrum', *B.Sc. thesis*, University of Kiel, (2012).
- [60] S. Frick, 'Mechanical switching of azobenzene by classical trajectory dynamics with surface hopping approach', *Advanced practical course in Hartke group*, University of Kiel, (2009).
- [61] T. Raeker, 'QM/MM Simulationen molekularen Schaltens unter sterischer Behinderung durch die Umgebung.', *B.Sc. thesis*, University of Kiel, (2011).
- [62] B. Baisch, et al., *J. Am. Chem. Soc.* 131, 442 (2009).
- [63] J. Kubitschke, C. Näther, R. Herges, *Eur. J. Org. Chem.*, 5041 (2010).
- [64] C. Bornholdt, 'Investigations into the development of light-driven cilia based on azobenzene', *Diploma thesis*, University of Kiel, (2005).
- [65] J. Steffen, 'QM/MM - Simulation der Photodynamik von Chromophoren in Polymeren', *B.Sc. thesis*, University of Kiel, (2013).
- [66] J. B. Schönborn, *personal communication*; unpublished.
- [67] R. Höppner, 'Simulation der Photochemie verbrückter Azobenzolderivate', *B.Sc. thesis*, University of Kiel, (2012).
- [68] G. Granucci, M. Persico, A. Zocante, *J. Chem. Phys.* 133(13), (2010).
- [69] A. Kostevic, 'Dynamik eines Azobenzolderivates auf dem zweiten elektronisch angeregten Zustand', *B.Sc. thesis*, University of Kiel, (2012).
- [70] F. Plasser, M. Barbatti, A. J. A. Aquino, H. Lischka, *Theor. Chem. Acc.* 131, 1073 (2012).
- [71] H. Larsson, B. Hartke, *Comput. Meth. Mater. Sci.* 13, 120 (2013).
- [72] M. Böckmann, N. L. Doltsinis, D. Marx, *Angew. Chem. Int. Ed.* 49(19), 3382 (2010).

- [73] M. Böckmann, N. L. Doltsinis, D. Marx, *J. Chem. Phys.* 137, 22A505 (2012).
- [74] C. W. Jiang, R. H. Xie, F. L. Li, R. E. Allen, *Chem. Phys. Lett.* 521, 107 (2012).
- [75] C. W. Jiang, R. H. Xie, F. L. Li, R. E. Allen, *J. Phys. Chem. A* 115, 244 (2011).
- [76] A. H. Gao, B. Li, P. Y. Zhang, K. L. Han, *J. Chem. Phys.* 137, 204305 (2012).
- [77] L. Liu, S. Yuan, W. H. Fang, *J. Phys. Chem. A* 115, 10027 (2011).
- [78] P. A. M. Dirac, *Proc. Royal Soc. (London) A* 123, 714 (1929).
- [79] J. Slater, *Phys. Rev.* 81, 385 (1951).
- [80] S. Vosko, L. Wilk, M. Nusair, *Can. J. Phys.* 58, 1200 (1980).
- [81] A. Becke, *Phys. Rev. A* 38, 3098 (1988).
- [82] C. Lee, W. Yang, R. Parr, *Phys. Rev. B* 37, 785 (1988).
- [83] A. Becke, *J. Chem. Phys.* 98, 5648 (1993).
- [84] 'TURBOMOLE V6.2 2010, a development of University of Karlsruhe and Forschungszentrum Karlsruhe GmbH, 1989-2007, TURBOMOLE GmbH, since 2007; available from <http://www.turbomole.com>.'
- [85] R. Siewertsen, J. B. Schönborn, B. Hartke, F. Renth, F. Temps, *Phys. Chem. Chem. Phys.* 13, 1054 (2011).
- [86] T. Nagata, *J. Organomet. Chem.* 692(1-3), 225 (2007).
- [87] M. Durrant, *Chem.-Eur. J.* 13(12), 3406 (2007).
- [88] A. L. Sobolewski, *Phys. Chem. Chem. Phys.* 10, 1243 (2008).
- [89] J. B. Schönborn, R. Herges, B. Hartke, *J. Chem. Phys.* 130(23), (2009).
- [90] J. M. Dieterich, B. Hartke, *Mol. Phys.* 108(3-4), 279 (2010).
- [91] C. R. Crecca, A. E. Roitberg, *J. Phys. Chem. A* 110(26), 8188 (2006).
- [92] L. Wang, X. Wang, *J. Mol. Struc. THEOCHEM* 847(1-3), 1 (2007).
- [93] B. G. Levine, C. Ko, J. Quenneville, T. J. Martinez, *Mol. Phys.* 104(5-7), 1039 (2006).
- [94] S. Kobayashi, H. Yokoyama, H. Kamei, *Chem. Phys. Lett.* 138(4), 333 (1987).
- [95] B. Mantey, 'Design of a molecular effector', *B.Sc. thesis*, University of Kiel, (2011).

- [96] A. Toniolo, C. Ciminelli, G. Granucci, T. Laiano, M. Persico, *Theor. Chem. Acc.* 111, 270 (2004).
- [97] R. Siewertsen, et al., *J. Am. Chem. Soc.* 131(43), 15594 (2009).
- [98] M. Aleskerov, *Izv. Vyssh. Uchebn. Zaved. Neft Gaz* pp. 64–100 (1975).
- [99] N. Sastry, *J. Chem. Eng. Data* 48, 977 (2003).
- [100] F. Mopsik, *J. Res. NBS Sect. A* 71, 287 (1967).
- [101] T. Cusati, G. Granucci, M. Persico, *J. Am. Chem. Soc.* 133, 5109 (2011).
- [102] S. Boys, F. Bernardi, *Mol. Phys.* 19, 553 (1970).
- [103] G. Granucci, M. Persico, G. Spighi, *J. Chem. Phys.* 137(22), 22A501 (2012).
- [104] E. Fabiano, T. Keal, W. Thiel, *Chem. Phys.* 349(1–3), 334 (2008).

## DECLARATION

I hereby declare that the work presented in this thesis was done by me, under the supervision of Prof. Dr. Bernd Hartke, with no other help than the referenced sources in the text. This is my first dissertation and the work has never been used in any other dissertation attempts. The dissertation complies to the good scientific practice rules as proposed by the German Research Foundation (DFG).

(Ole Carstensen)

Kiel, July 1, 2014



# CURRICULUM VITAE

## NISS OLE CARSTENSEN

Date of birth - 02.02.1984  
Birthplace - Wyk on the isle of Föhr  
Nationality - German  
Address - Westring 271, 24116 Kiel

## EDUCATION

2004-2009 - Diploma studies in Chemistry, University of Kiel  
2009 - Diploma thesis in Theoretical Chemistry  
under the supervision of Prof. Dr. B. Hartke  
2009-2014 - Ph.D. student at the University of Kiel  
under the supervision of Prof. Dr. B. Hartke